Abstract

This study applies chemical dating of monazite following the methods of Williams et al. (2017) in samples from a septum of metapelite that lies within the Belchertown intrusion in central Massachusetts. This septum is identified as Partridge Formation sillimanite schist that is characterized by large (10 cm long) sillimanite porphyroblasts interpreted to be pseudomorphs after andalusite in previous studies. Three samples (BE17-2, PF-2, and MAR20-1) were collected from an outcrop on the southern end of the septum. Whole rock composition data for these samples was obtained from XRF analysis. Individual monazite grains were identified by compositional mapping of thin sections with the electron microprobe at UMass. Individual monazite grains were mapped for Y, Th, and other elements and chemical domains were identified. Complete chemical analysis of selected domains was conducted and an age was calculated following the methods of Williams et al. (2017). Pseudosections detailing P-T stability fields for these samples were generated using Theriak Domino and the whole rock composition data. The estimated pressure of stability for all three samples is greater than 5 kbar. The temperature stability range for one staurolite-containing sample is estimated to be 500-700°C, and for the other staurolite-lacking samples, the temperature range is greater than 650°C. The majority of monazite grains in all three samples give an age of $\sim$370 Ma, which corresponds to the Neo-acadian orogeny and metamorphism in central Massachusetts (Robinson et al., 1998). A few grains from two samples give much younger dates of $\sim$280 Ma, which dates to the Alleghanian orogeny. Highly irregular, patchy textures in Y composition maps of these grains are interpreted to be the result of a fluid-mediated alteration event. Fluid alteration would reset the U-Th-Pb system, leading us to conclude that the fluid alteration event would have occurred during the older Neo-acadian event.

The Age and Petrogenesis of a Sillimanite Gneiss within the Belchertown Igneous Complex, Massachusetts

Margrit Rindlisbacher
Supervised by: Prof. Steve Dunn

May 21, 2021

Acknowledgements

Many thanks to Dr. Mike Jercinovic, Serena Dameron, Dr. J. Michael Rhodes, Pete Dawson, and staff at the University of Massachusetts: Amherst Geosciences Electron Microprobe and XRF Facility for their assistance. Mount Holyoke College Geology department members have provided invaluable support, including Claire Pless and Sophia Brooks-Randall. Thank you to the advising committee, Profs. Michelle Markely, Ombretta Frau, and most importantly, Steve Dunn, who provided impeccable guidance even through the Zoom screen. Finally, thank you to all my friends and family for their encouragement and love as I worked on this project. This work was supported in part by the National Science Foundation, EAR-0126661 to Prof. Steven Dunn.

Contents

List of Figures

List of Tables

1 Introduction

An interesting and relatively recent method of determining the age of rocks is the chemical dating of the mineral monazite. The most common method of age dating old rocks relies on the radioactive decay of U in the mineral zircon, which involves two parent isotopes of U and their two daughter products of Pb. Several analytical techniques can be used for that method and require measuring the isotope ratios of U and Pb. Such age determinations can be very precise or less precise, depending on the method and the nature of the sample zircon. Although monazite can also be dated by isotope methods, in this study, we use the chemical method which does not rely on the use of isotope ratios. Dating monazite by the chemical method relies on the electron microprobe (Fig. 1) to measure the amount of U and Th, the radioactive parent elements, and the amount of Pb, the daughter element. Monazite is a light rare-earth element (LREE) phosphate that easily incorporates U and Th in its structure as it forms, but does not permit Pb. Therefore, all of the Pb present in monazite is interpreted to be the product of U and Th decay. The total amount of U and Th and the total amount of Pb is all that is needed to calculate an age; isotopic ratios are not needed (Williams et al. 2007, Williams et al. 2017). U-Th-Pb dates from monazite represent mineral growth ages due to its high closure temperature for Pb and actinide series elements (Cherniak and Pyle, 2008; Markley et al. 2018). As with isotope dating methods, one must assume the mineral as a closed system with regard to the radioactive parent elements and the radiogenic daughter products.

The following equation is used to calculate the age, with Pb, U, and Th being the concentration (ppm), t being age (years), and λ^{232}, λ^{238}, and λ^{235} being the decay constants for Th^{232} (4.95E-11/year), U^{238} (1.55E-10/year), and U^{235} (9.85E-10/year), respectively (Williams et al. 2007).

$$Pb = [\frac{Th}{232}(e^{\lambda^{232t}} - 1)]208 + [\frac{U}{238}0.9928(e^{\lambda^{238t}} - 1)]206 + [\frac{U}{235}0.0.0072(e^{\lambda^{235t}} - 1)]207$$

The electron microprobe is a non-destructive analytical method that can measure the composition of minerals within a thin section (Fig. 1). The non-destructive nature preserves the monazite grains within the original fabric of the rock, which allows consideration of texture and other minerals in the interpretation of the events represented by the monazite age. For example, the age of monazite grains, when present as inclusions in other minerals or oriented within foliations, can be used to determine the age of foliation development or put limits on when host minerals formed in metamorphic rocks. This method has the potential to unravel the timing of events in rocks with a complex history (Williams et al. 2007, Williams et al. 2017).

In this study, we investigate monazite ages and metamorphic conditions for samples of pelitic rocks that experienced more than one metamorphic event. Robinson (2016) and Massey and Moecher (2008) describe a septum of pelitic rock within a large pluton in western Massachusetts (Fig. 3, 2, 4). These pelitic rocks (interpreted as Ordovician Partridge Formation, and henceforth referred to as the Partridge Formation schist septum) occur as a narrow belt entirely surrounded by quartz monzonite and related rocks of the Devonian

Belchertown Igneous Complex. The goals of this study are two-fold: 1) to test this new monazite dating method these rocks characterized by an unusual geologic history, and 2) to learn more about the metamorphic history of these rocks. Monazite age dates, monazite compositional zoning, the mineral assemblage, and other textural clues will be our primary sources of interpretation. We also recreate the observed mineral assemblage in pseudosections at feasible pressure-temperature conditions.

Figure 1: Cameca SXFive-TACTIS electron microprobe at the University of Massachusetts: Amherst. Analysis done with Cameca Peaksight PC software.
From https://blogs.umass.edu/probe/facility/.

1.1 Geologic setting: history and significant geologic units

New England has a rich and varied geologic history. Five major periods of metamorphism and orogenesis are recognised: the Taconian (455-422 Ma, Ordovician), the Acadian (423-385 Ma, Silurian-Devonian), the Neo-Acadian (366-350 Ma, Devonian), the Late Pennsylvanian (300-390 Ma, Carboniferous), and the Alleghanian (280-260 Ma) (Robinson et al. 1998). The Taconian was characterized by the subduction of the southern margin Laurentia below a magmatic island arc. The Acadian featured a collision between the Laurentia-Medial New England and the outer belts of Composite Avalon in Maine. The Acadian concluded with tonalitic-granitic magmatism and up to granulite-facies metamorphism, possibly due to upwelling from subduction. The Neo-Acadian was characterized by tonalitic-granitic magmatism and up to granulite-facies metamorphism, as well as major deformation in central Massachusetts. The late Pennsylvanian period was characterized by magmatism, metamorphism, and deformation in the south. The Alleghanian featured penetrative deformation, granitic intrusions, and up to sillimanite-grade metamorphism (Robinson et al. 1998). The

Taconian, Acadian, and Alleghanian orogenies are largely responsible for the creation of the Appalachian mountains (Moecher 1999).

Regarding the area of our study, two main geologic units are relevant: the Belchertown igneous intrusion, and the Partridge Formation schist septum. The Belchertown complex is a predominantly quartz monzonite to tonalite pluton, circular in shape with a surface area of 120 km^2 (Fig. 2, 3, Ashwal 1979). It is a syntectonic Devonian intrusion determined to be 380 $\pm$ 5 m.y from U-Th-Pb zircon age dating (Ashwal 1979). This places it within the Acadian and Neo-Acadian orogenies (Robinson et al. 1998). It intrudes into rocks of the Bronson Hill anticlinorium, which consists of a series of gneiss domes and anticlines stretching from New Hampshire to New York (Fig. 2, Ashwal 1979). The geology of the surrounding area consists of metamorphosed Middle Ordovician volcanic and sedimentary rocks that include the Partridge Formation, metamorphosed Silurian and Lower Devonian sedimentary and volcanic rocks that includes the Erving Formation, and Lower Jurassic and Upper Triassic clastic sedimentary rocks and basalts (Fig. 2, 3, Ashwal 1979). The Erving Formation directly overlies the Partridge Formation (Ashwal 1979). To the north, the Belchertown pluton discordantly intrudes into the Erving formation, and to the east, the Belchertown pluton is concordant to the east limb of a Partridge formation syncline (Ashwal 1979). The Partridge formation schist septum, area of our study, extends into the Belchertown pluton for a length of about 5 km and is located about 2-3 km west of the Partridge formation limb (Fig. 3, 4). Both Partridge Formation outcrops are narrow linear structures that run parallel to each other, oriented north to south (Fig. 3, 4).

Robinson (2016) mentions a $\sim$380 Ma for the age of the schist septum, calculated using monazite dating; however no actual data for this has been published (Robinson 2016). Contact metamorphism due to the intrusion of the Belchertown igneous complex is understood to be the primary metamorphic event (Massey and Moecher 2008, Robinson 2016). The schist septum consists of quartz-muscovite-biotite-garnet-staurolite-kyanite schist for the northernmost 1 km, quartz-muscovite-biotite-garnet-sillimanite schist with minor staurolite for the middle 2 km, and quartz-biotite-garnet-sillimanite schist for the southernmost and final 1 km, closest to the center of the pluton (Ashwal 1979). Evidence for increasing metamorphic grade on the N-S axis led Robinson (2016) to describe the structure as a "rectal thermometer" (Robinson 2016). Massey and Moecher (2008) classify the whole section as a quartz-plagioclase-biotite-garnet-sillimanite-alkali feldspar paragneiss that locally contains cordierite (Massey and Moecher 2008). The sillimanite in the northernmost 3 km of the septum is fibrolitic (i.e., extremely fine-grained), while in the southern 2 km, the sillimanite appears as crystals as large as 10 cm in length (Robinson 2016, Ashwal 1979). Robinson (2016) and Ashwal et al. (1979) interpret these sillimanite crystals to be pseudomorphs after andalusite.

2 Sample Localities

We collected several samples at an outcrop on the eastern side of Michael Sears Road in Belchertown, MA, near the southern end of the schist septum (Fig. 5). The coordinates of this location are: (42.239173, -72.356964) (Obtained from Google Maps). This location

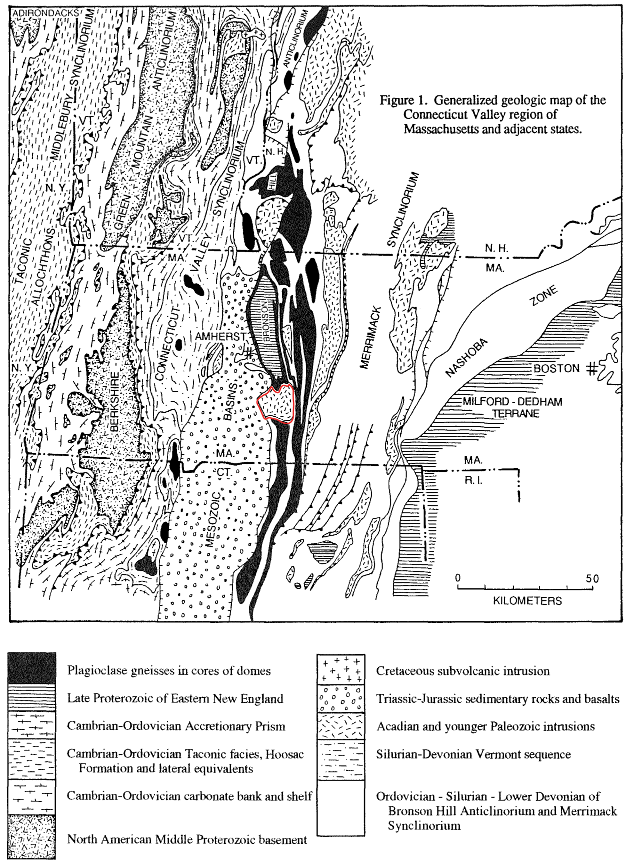

Figure 2: Generalized geologic map of the Connecticut Valley region of Massachusetts and adjacent states (taken from Robinson 1992). Belchertown igneous complex outlined in red.

is described in the field guide (Stop 9) by Robinson (2016). We collected additional samples of the Partridge Formation septum in a less-well exposed wooded area north of Cold Spring Road approximately 0.85 km along strike north of the Michael Sears Road location. Additional samples from the Michael Sears Road exposure, collected previously by Professor Steve Dunn and Professor Michelle Markley, are also included in my study.

The exposure at the Michael Sears Road locality consists of coarse sillimanite gneiss (Fig. 6). Many parts of this outcrop show a preferred mineral orientation expressed as both a lineation and a foliation, generally striking NNE parallel to the outcrop pattern as mapped by Massey and Moecher (2008) and shown in Fig. 4, 6. Samples PF1 and PF2-A were collected from the exposures within about 30 feet of the road, on its east side. This rock type also occurs in small, sporadic outcrops for about 50 to 75 feet into the woods. Additional samples, including BE17-2, from this same location were collected previously in 2017 by Professor Steve Dunn and Professor Michelle Markley. The sillimanite porphyroblasts in some parts of the exposure show random orientation, giving a jackstraw appearance on the rock surface. In other areas, the porphyroblasts are aligned in more of a curving, almost swirling pattern that may have resulted from folding within the unit. However, the sporadic nature of the exposure and variability of grain orientations did not reveal obvious fold axes,

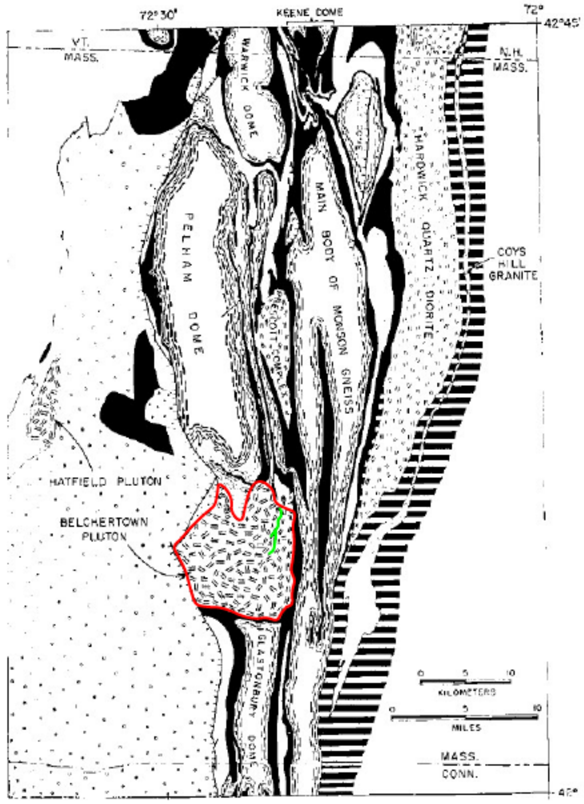

Figure 3: Belchertown pluton (red) with the Partridge Formation schist septum (green) and the surrounding geology (taken from Ashwal 1979).

but instead appeared somewhat chaotic. Still, the overall, prevailing orientation of both foliation and lineation when present strikes NNE.

About 50 to 75 feet east of the road into the woods is a weathered exposure of well-foliated schist striking NNE. Sample MAR20-1 was collected from this outcrop. About 25 more feet into the woods to the east, limited outcrops of the Belchertown Intrusive Complex, consisting of coarse granodiorite, can be found. The total width of the Partridge Formation schist septum is not certain due to lack of observable outcrop on the western side of the exposure.

3 Analytical Methods

We cut samples from BE17-2, PF-1, PF-2, and MAR20-1, and selected billets to be sent to Spectrum Petrographics in Vancouver, Canada, for thin sectioning. Some additional thin sections were made in house by Claire Pless, including MAR20-1B. After petrographic study, we selected four samples (BE17-2, PF-1, PF-2, and MAR20-1) for whole-rock X-ray Fluorescence (XRF) analysis and, ultimately, three samples (BE17-2, PF-2, and MAR20-1) for monazite geochronology.

Whole rock composition data was obtained for samples BE17-1, MAR20-1, PF-1 and

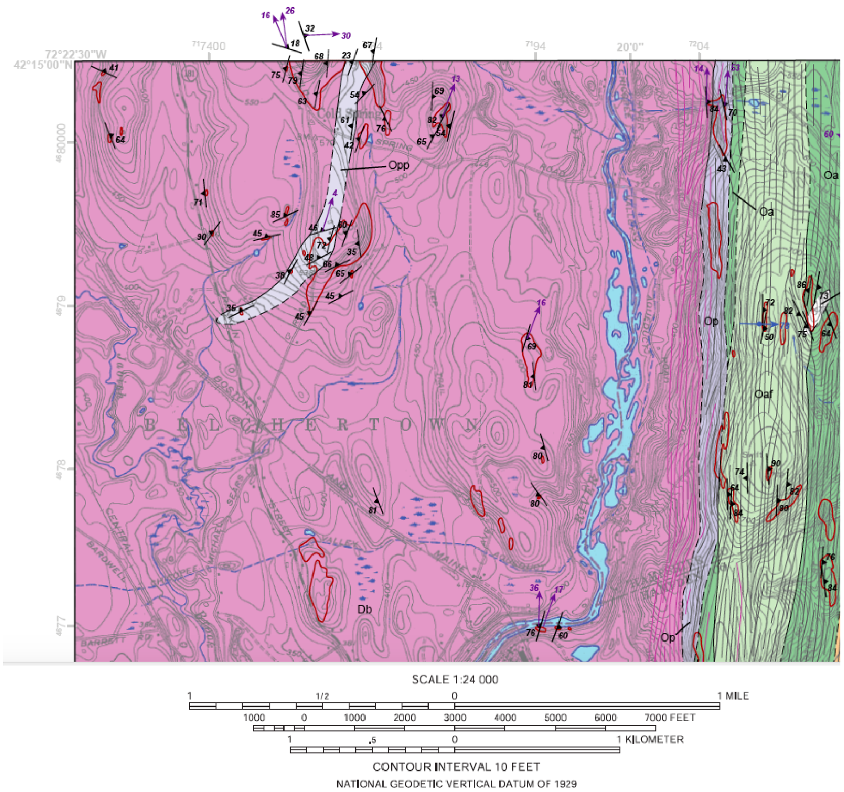

Figure 4: Close-up image of Belchertown igneous complex (Db, purple) and Partridge Formation schist septum (Opp, light blue) (taken from Massey and Moecher 2008). Outcrop exposures are indicated by red outlines. Sampling occurred along the eastern side of Michael Sears Road on the southern end of the septum.

PF-2 by crushing and grinding a fist sized sample into powder. The samples were then ignited overnight to drive off volatiles, mixed with a flux, and melted into a glass bead for x-ray fluorescence analysis. The analyses were completed in Mike Rhode's lab at the University of Massachusetts at Amherst with the assistance of Claire Pless and Pete Dawson. The whole rock data, given in wt% of oxides, was then converted into molar proportions for entry into Theriak Domino (Table 1).

Samples were checked for monazite first with a petrographic microscope, and then the whole section was scanned at the UMass microprobe lab for the elements Mg, Ca, Ce, and Zr. This was done by rastering the electron beam back and forth across the section with wavelength dispersive spectrometers set to count the characteristic X-rays for these elements. The element K was also scanned in sample MAR20-1. The Mg, Ca, and K maps show the location and distribution of the principal minerals, such as biotite, chlorite, garnet, quartz, and feldspars (Figs. 8, 9, 11) and the Ce and Zr show the locations of monazite and other accessory minerals (Williams et al. 2017). The second step in the monazite work is compositional mapping of individual monazite grains. The location of monazite is revealed by the presence of Ce and absence of Zr, as monazite concentrates light rare earth elements so bright spots in Ce, indicating high concentrations, also indicate the location

Figure 5: View of the Partridge formation outcrop on the eastern side of Michael Sears Road in Belchertown, facing south.

of monazite grains (Williams et al. 2017). Selected monazite grains were identified and mapped for Y, Th, U, Ca, and Nd by Serena Dameron under the direction of Dr. Michael Jercinovic at the UMass Microprobe Lab. The maps were processed simultaneously so that color intensity relating element concentration is comparable across all maps for a given sample (Fig. 7). Color intensity is not comparable across samples. Selected compositional domains of monazite grains are analysed for U, Th, and Pb (and many other elements) to calculate an age using decay constants for U and Th, the concentrations of U and Th, and the concentration of accumulated Pb (Williams et al. 2017, Markley et al. 2018). The equation for calculating dates was described previously (see: Introduction), and the complete procedure for calculating dates is outlined in Williams et al. 2017. A large number of elements were included in the microprobe analysis because the X-rays of interest for U, Th, and Pb are affected by absorption and fluorescence from nearby atoms of the other elements in the monazite. Adjusting for these matrix effects is an important part of this technique (Jercinovic et al., 2008; Williams et al., 2017).

Monazite date data was processed by Dr. Michael Williams. Individual ages and their standard deviations were graphed in histograms, sorted by similar chemical domains, to display the range of data. One date and its standard deviation was calculated for each domain. Interpretation of this data includes observing trends in compositional domains and their corresponding dates and observing grain location within the context of the thin section

Figure 6: Grapefruit-sized sample of Partridge formation schist septum collected from Michael Sears Rd, Belchertown. “Matchstick-sized” sillimanite crystals as described by Robinson 2016 are featured.

as a whole.

We also estimate the pressures and temperatures of metamorphism that these rocks have experienced using Theriak-Domino. Theriak Domino is a program designed by C. de Capitani and K. Petrakakis that computes equilibrium assemblage diagrams (also known as pseudosections) that show possible mineral assemblages over a range of pressure and temperature for a given whole-rock composition (de Capitani 2020). Theriak Domino can also calculate pseudo-binary or pseudo-ternary phase diagrams, and phase compositional isopleths (de Capitani 2020). Theriak Domino uses the principle of Gibbs free energy minimization to do its calculations (de Capitani 2020). Two databases of minerals are available, the Berman database (JUN92) or the Holland and Powell database (tcdb55c2d) (Allaz 2011).

For our purpose, we found the JUN92d.bs internally-consistent database that comes with the program files gave good results in less time and with fewer awkward, broken reaction curves than the alternative database, tcdb55c2d. In order to obtain geologically reasonable results, water had to be included in the bulk composition. The actual H_2O content of the samples is not measured by the XRF whole rock analysis. We used 4.25% H_2O which is consistent with "average pelite" of various metamorphic grades as reported by Shaw (1956). We attempted to adjust the oxygen content as a means of controlling the ferrous/ferric iron ratio, however this resulted in producing magnetite in all samples (magnetite is absent in these rocks) and also produced large stability fields for amphibole, which is not present in these rocks, nor in pelites generally. So, we applied an open quantity of oxygen in all these calculations, which is the most common approach used by petrologists when constructing pseudosections. Pseudosections were generated by Sophia Brooks-Randall and Prof. Steve Dunn.

Figure 7: Color intensity scale for monazite composition maps. Black is no concentration, white is highest concentration.

4 Results

4.1 Petrographic Analysis

Sample BE17-2 was collected by Profs. Steve Dunn and Michelle Markley in 2017 from the Partridge Formation outcrop on Michael Sears Road in Belchertown, Massachusetts (Fig. 5, 8). BE17-2 is a schist-gneiss and contains large sillimanite porphyroblasts. Foliation visible in thin section (Fig. 8) and in hand sample is parallel to N-S septum lineation. Thin section displays gneissic-schistose texture with inequigranular crystals. Porphyroblasts of sillimanite are idioblastic to subidioblastic. Other minerals include garnet, biotite, muscovite, quartz, chlorite, and apatite. Red-green thin section map showing Ca concentration in red and Mg concentration in green reveals garnet (in brown) coronas surrounding and partially surrounding sillimanite porphyroblasts (Fig. 8). Red (Ca-rich) inclusions within the sillimanite crystals are apatite.

Sample PF-2 was collected in 2020, also from the outcrop right at the side of Michael Sears Road (Fig. 5, 9). PF-2 in thin section appears to be less foliated than BE17-2, with a slightly more granulitic texture, though an overall similar fabric and mineral assemblage (Fig. 9). Sillimanite porphyroblasts are idioblastic to subidioblastic. Red-green thin section map showing Ca concentration in red and Mg concentration in green reveals that sillimanite crystals lack the garnet corona texture present in BE17-2 and PF-1 (Fig. 9). Garnet is present in association with chlorite (bright green) and displays compositional zoning with a higher Mg/lower Ca core and lower Mg/higher Ca rims (Fig. 9).

PF-1 photomicrographs compiled in Photoshop show a sillimanite porphyroblast with coronitic garnet (Fig. 10). The sillimanite porphyroblast appears to be retrograding to muscovite, with the muscovite forming pseudomorphic rims replacing the sillimanite around the edges and along fractures.

MAR20-1 was collected in 2020 from the eastern edge of the Partridge Formation exposure on Michael Sears Road, from an outcrop located about 50 ft east of the road (Fig. 11). It is more strongly foliated and more shistose than BE17-2 and PF-2. Its foliation is aligned with the NNE strike of the septum. Present minerals include garnet, chlorite, muscovite, biotite, quartz, sillimanite, and plagioclase (Fig. 11). Staurolite is observed in this sample (Fig. 13), while BE17-2 and PF-2 lack staurolite. K-Mg-Ca thin section images of MAR20-1 feature garnet porphyroblasts (Fig. 11). Observation of MAR20-1B on the SEM also revealed replacement of more calcic plagioclase feldspar by albite (i.e. albitization) (Fig. 13).

4.2 Monazite Compositional Maps

Monazite grains in BE17-2, PF-2, and MAR20-1 are scattered throughout the thin section. The grains range from 20 to 100 microns and are highly variable in shape (Fig. 14, 16, 18; see appendix for full catalogue of grains for each sample). Grains in PF-2 are more regular in shape with clear grain boundaries, while BE17-2 and MAR20-1 feature greater numbers of highly irregular shapes and textures and less defined grain boundaries. Common trends in compositional domains observed in all three samples include a high Y core and rim with a low Y mantle, a low Y core and mantle with a high Y rim, and a continuous high Y concentration for the whole grain. Also observed in all three samples is a mottled/patchy, irregular texture that is most visible in the Y composition maps (Fig. 14, 16, 18, 29; see appendix for full catalogue of Y maps for each sample).

Grains in BE17-2 with irregular, mottled, Y textures include M1, M2, M3, M4, M5, M6, M7, M10, M11, M14, M16, M19, M20, M22, M24, and M26. Th is present in low concentrations, though certain grains (M1, M2, M5, M6, M7, M10, M11, M13, M16, M22, M24, M25, and M26) display a similar mottled texture to that present in the Y concentration maps. Areas of high Y concentration correspond to zones of low Th and low Ca concentration. Grains generally contain lower concentration Dy and Ca, but have uniform high concentration of Nd. U textures are similar to the Y textures, though U is present in lower concentrations (See appendix).

Monazite grains in PF-2 that display the irregular, patchy Y textures include M1, M2, M4, M6, M11, M15, M16, M17, M18, and M19. Areas of Th depletion correspond to areas of Ca depletion. Overall concentrations of U and Ca are low while Nd concentrations are high. U, Ca, and Nd concentration maps display variations in texture, while Dy concentrations are uniformly low in all grains (See appendix).

Monazite grains in MAR20-1 generally lack the patchy, irregular Y texture seen in the other samples. M1, M2, M8, M12, and M14 have homogenous high Y composition throughout the entire grain. Irregular Th texture is present in M10, though the irregularity is not patchy in nature to the extent of that in some grains in BE17-2 and PF-2. U-concentration maps display more uniform textures. Ca composition is very similar to Th composition patterns, with areas of extremely high Ca concentration in grains M3, M8, and M10 (See appendix).

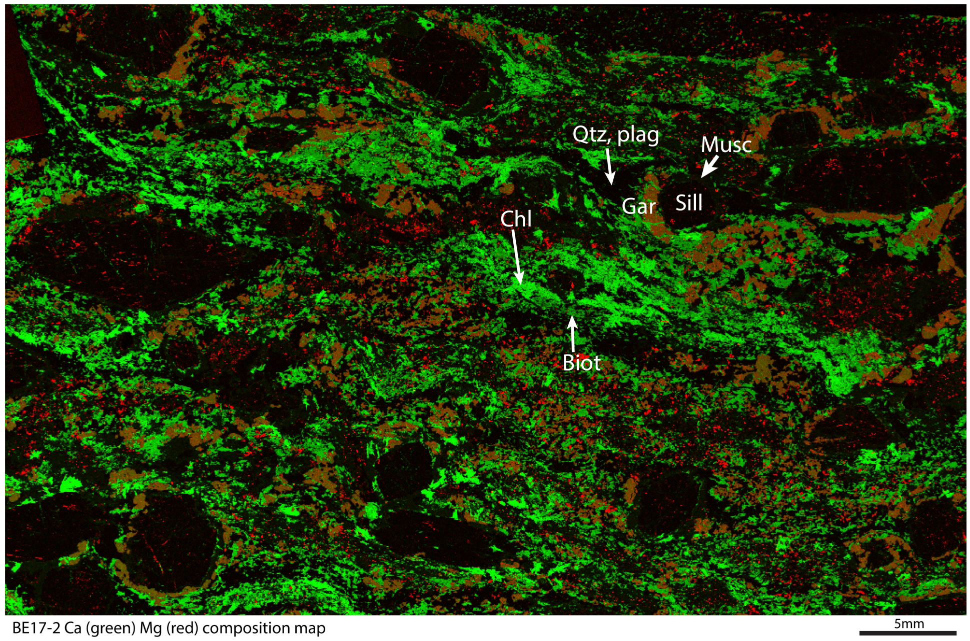

Figure 8: Composite whole thin-section element map of sample BE17-2 showing Ca in red and Mg in green. Red represents plagioclase and apatite, green is both biotite and chlorite, and brown areas, indicating overlapping Ca and Mg, correspond with garnet. Large black areas are sillimanite porphyroblasts and smaller disseminated black areas are mostly quartz. Long dimension is approximately 40 mm.

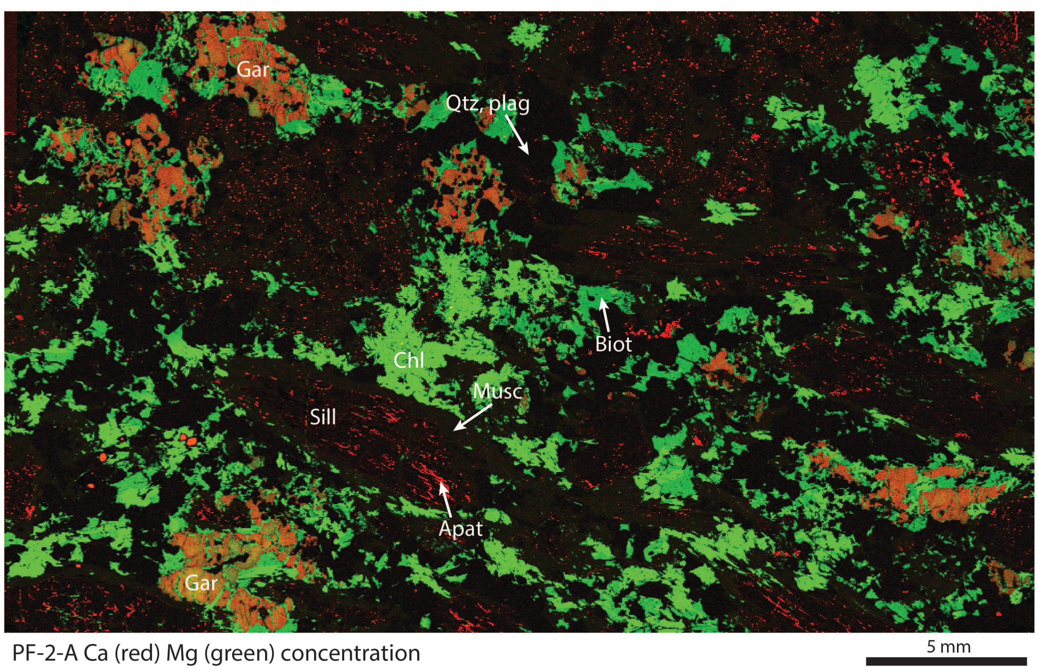

Figure 9: Composite whole thin-section element map of sample PF-2 showing Ca in red and Mg in green. Red represents plagioclase and apatite, green is both biotite and chlorite, and brown areas, indicating overlapping Ca and Mg, correspond with garnet. Large black areas are sillimanite porphyroblasts and smaller disseminated black areas are mostly quartz.

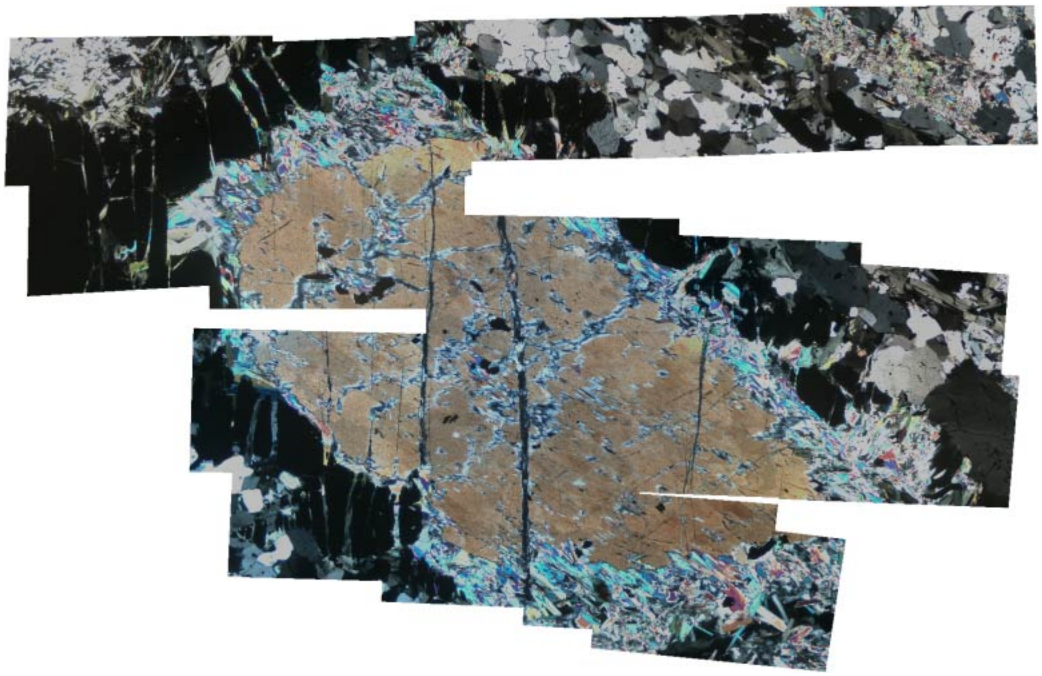

Figure 10: A composite photomicrograph mosaic of a sillimanite crystal with coronitic garnet in PF1-A in cross polarized light. The sillimanite crystal (beige) retrogrades to muscovite (white, light blue) along fractures and on the outside edge of the crustal. A coronitic garnet (black) surrounds three edges of the crystal. The sillimanite grain is approximately 4 mm long. Mosaic assembled in Photoshop.

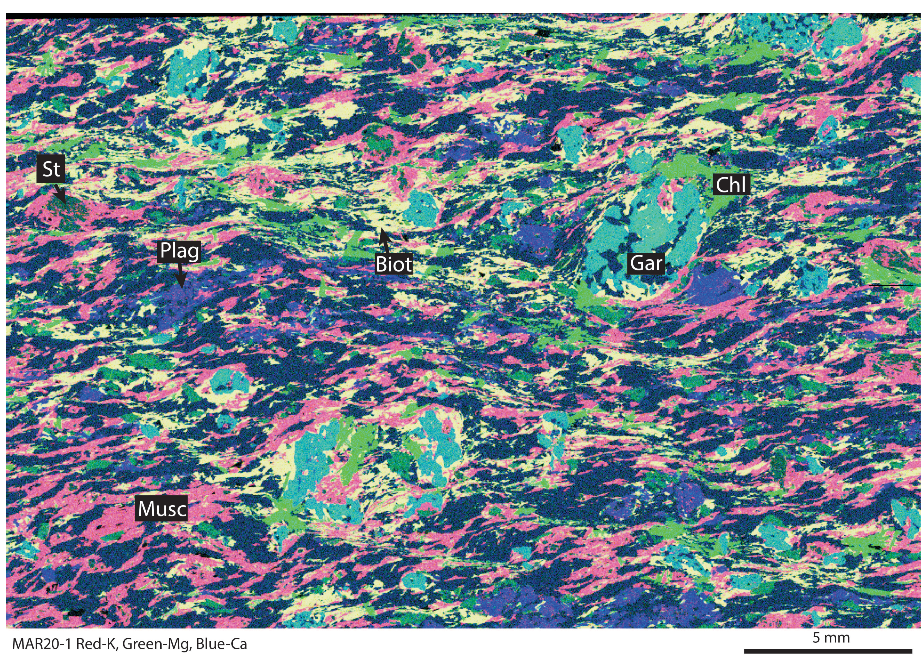

Figure 11: Full section map of MAR20-1. K is red, Mg is green, and Ca is blue. Garnet porphyroblasts are teal, chlorite is lime green, staurolite is dark green, biotite is yellow, muscovite is pink, and plagioclase is dark blue.

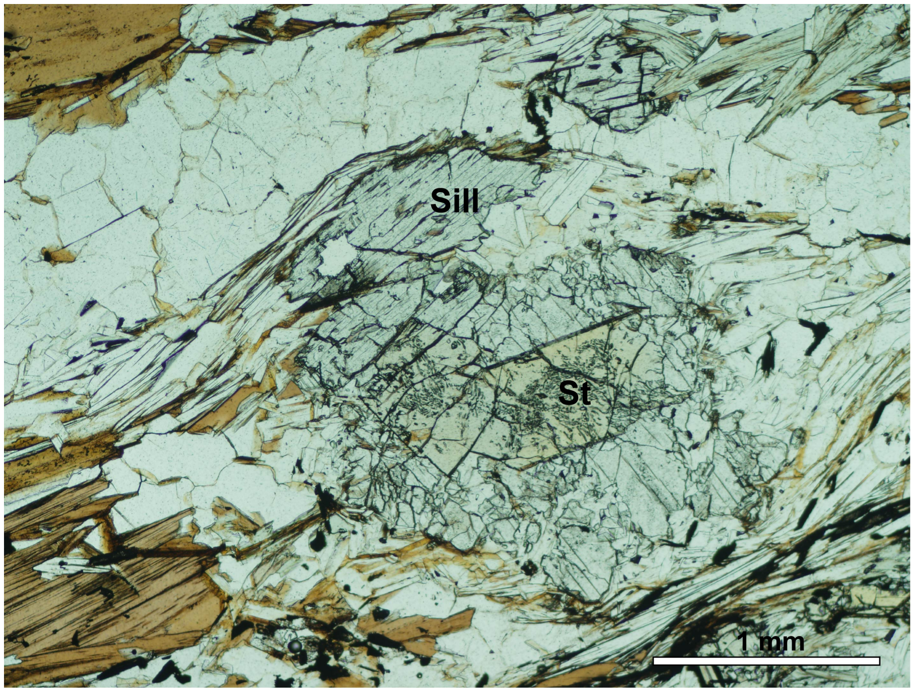

Figure 12: Sillimanite porphyroblast (light blue) featuring an euhedral stuarolite crystal (light yellow) within. From MAR20-1B; plane light.

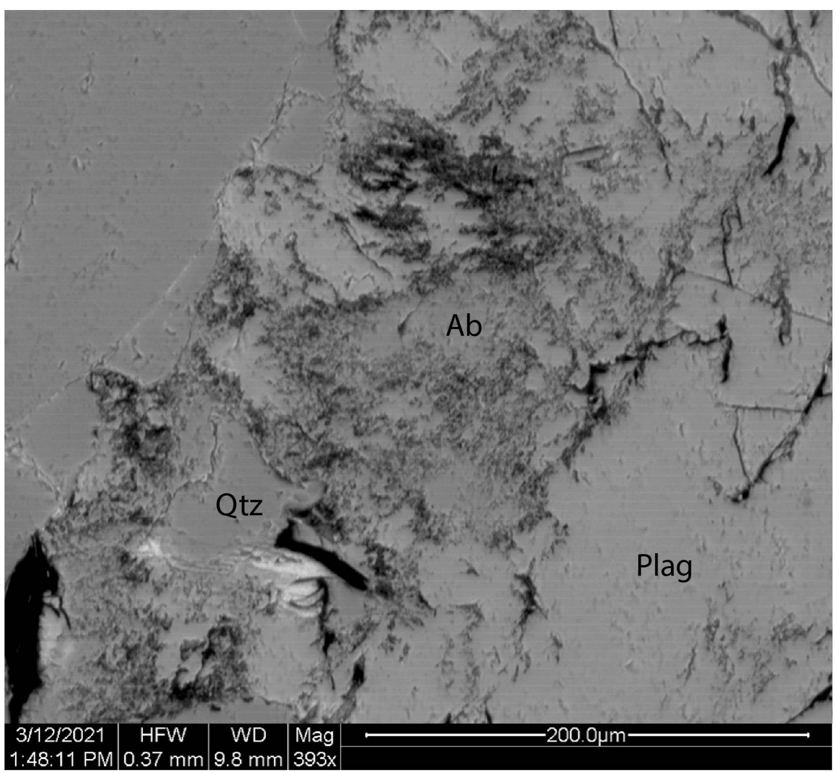

Figure 13: SEM image showing albitization of plagioclase feldspar from MAR20-1B.

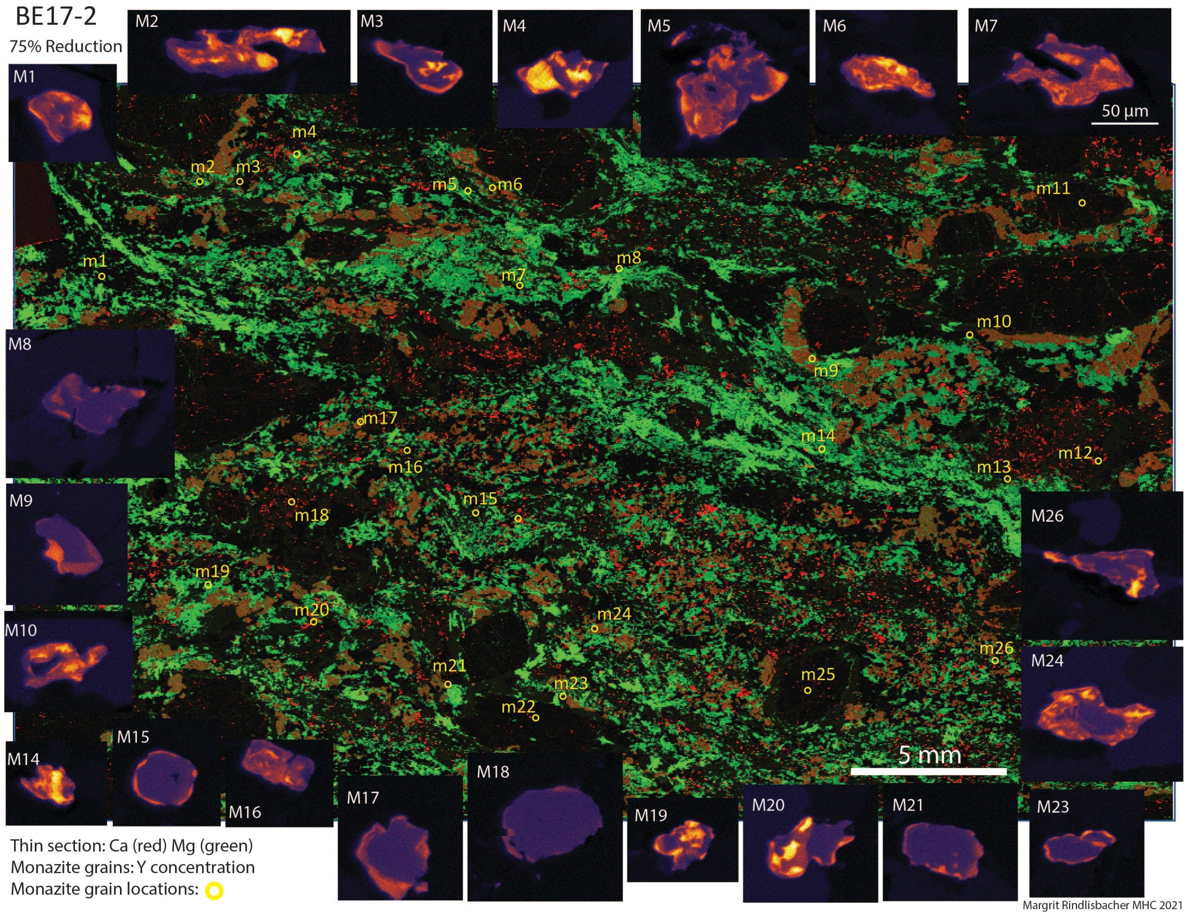

Figure 14: Composite figure of BE17-2 featuring Y composition maps of the smallest monazite grains. Refer to Fig. 15 for grains larger than ∼100 microns. The whole thin section of BE17-2 is a composite element map showing Ca in red and Mg in green. Monazite grain locations are circled in yellow.

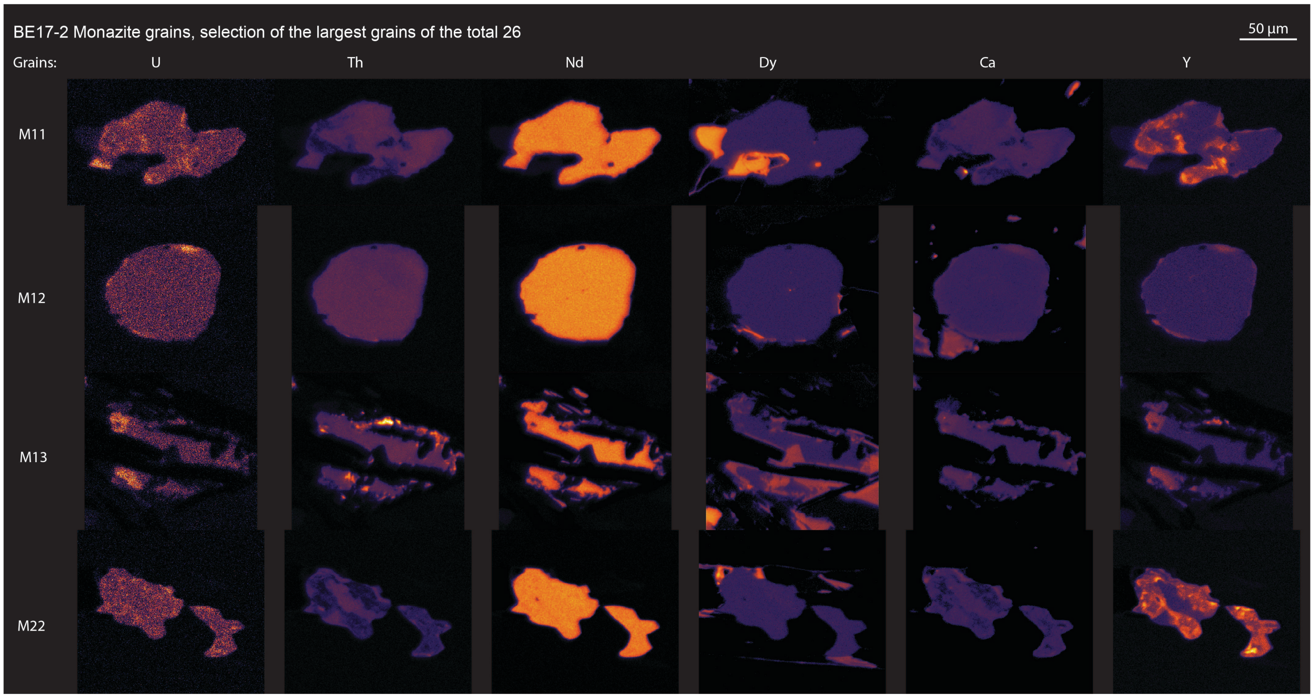

Figure 15: The largest monazite grains from BE17-2. U, Th, Nd, Dy, Ca, and Y maps are featured for M1, M12, M15 and M22.

4.3 Monazite Date Results

Analysis points are sorted by domains type in the monazite grains: the high Y cores (labeled as 2 in the data tables, see appendix), high-Y outer cores (3), the "main" low Y zone commonly found in the mantle and core of monazite grains (4), and high Y inner rims (meaning the inner edge of high Y rims, 5) and high Y outer rims (meaning the outer edge of high Y rims, 6). These domains are not exactly the same classification used to describe major trends in Y composition patterns, though they share domain descriptions. Two time periods are identified: ~370 Ma, given by the majority of the grains in all three samples, and ~280 Ma, given by a few grains in MAR20-1 and BE17-2. Dates and uncertainties given for each monazite compositional domain represent the weighted mean and 2 standard deviations for 5-7 analyses. These were provided by Professor Williams, UMass, as were the histograms in Figs. 20, 21, and 22.

For BE17-2, a total of 12 analysis points from "main" low Y domains resulted in an age of 370 ± 3 Ma. 6 total analysis points from outer core domains resulted in an age of 369 ± 12 Ma. One analysis point from the inner high Y rim of M15 resulted in a date of 374 Ma ± 7.2. High Y outer rim dates consist of two data points, one from M9 with an age of 281 Ma ± 2.3 and one from M17 with an age of 262 Ma ± 5.7. These outer rim dates are significantly younger than the other dates calculated for BE17-2. Main and inner rim dates are constrained, while outer core and outer rim dates are more widespread (Fig. 20).

For PF-2, 12 analysis points in "main" low Y domains resulted in a date of 372 ± 4 Ma. 7 analysis points from high-Y "inner rim" domains resulted in an age of 368 ± 7 Ma.

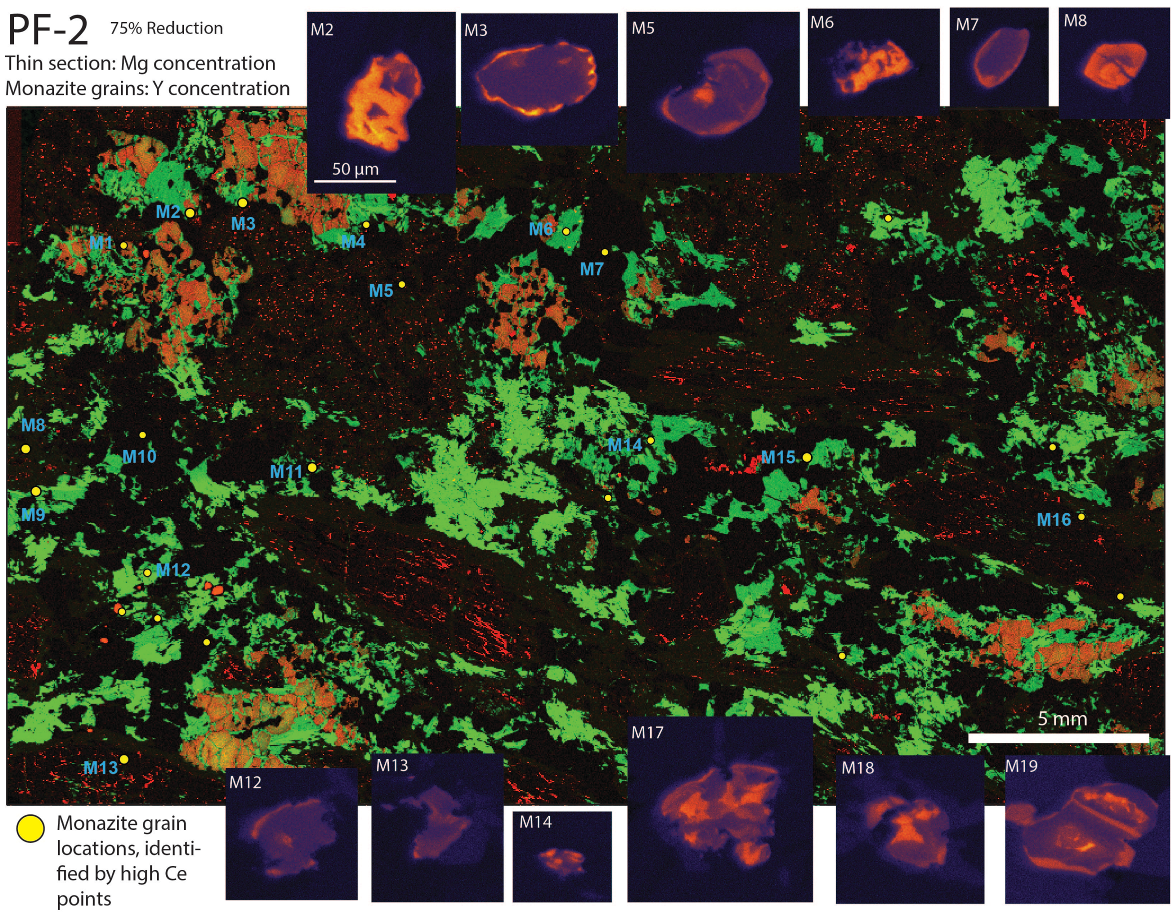

Figure 16: Composite figure of PF-2 featuring Y composition maps of the smallest monazite grains. Refer to Fig. 17 for grains larger than ∼100 microns. The whole thin section of PF-2 is a composite element map showing Ca in red and Mg in green. Monazite grain locations are indicated with yellow circles.

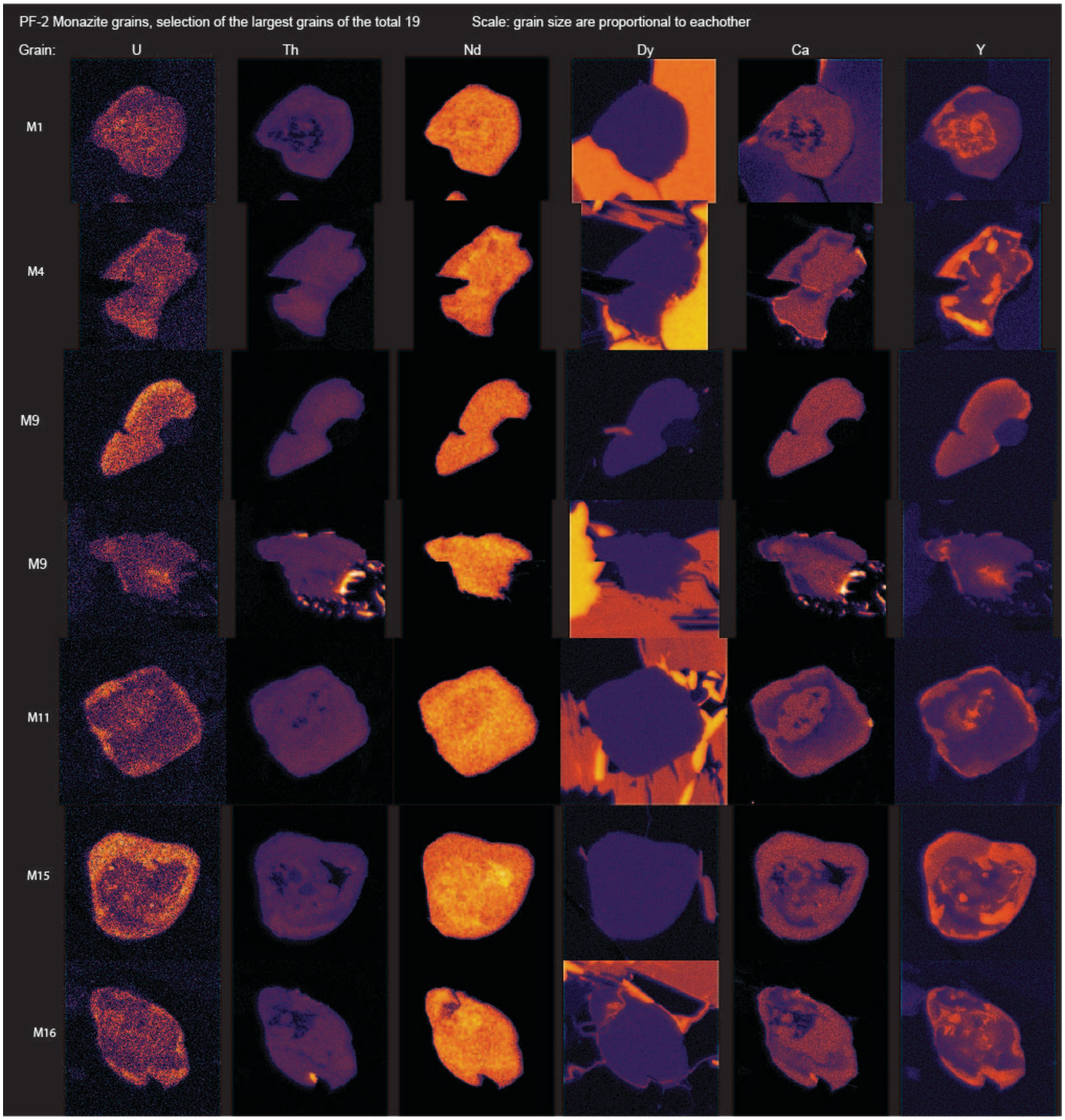

Figure 17: The largest monazite grains from PF-2. U, Th, Nd, Dy, Ca, and Y maps are featured for M1, M4, M9, M10, M11, M15, and M16.

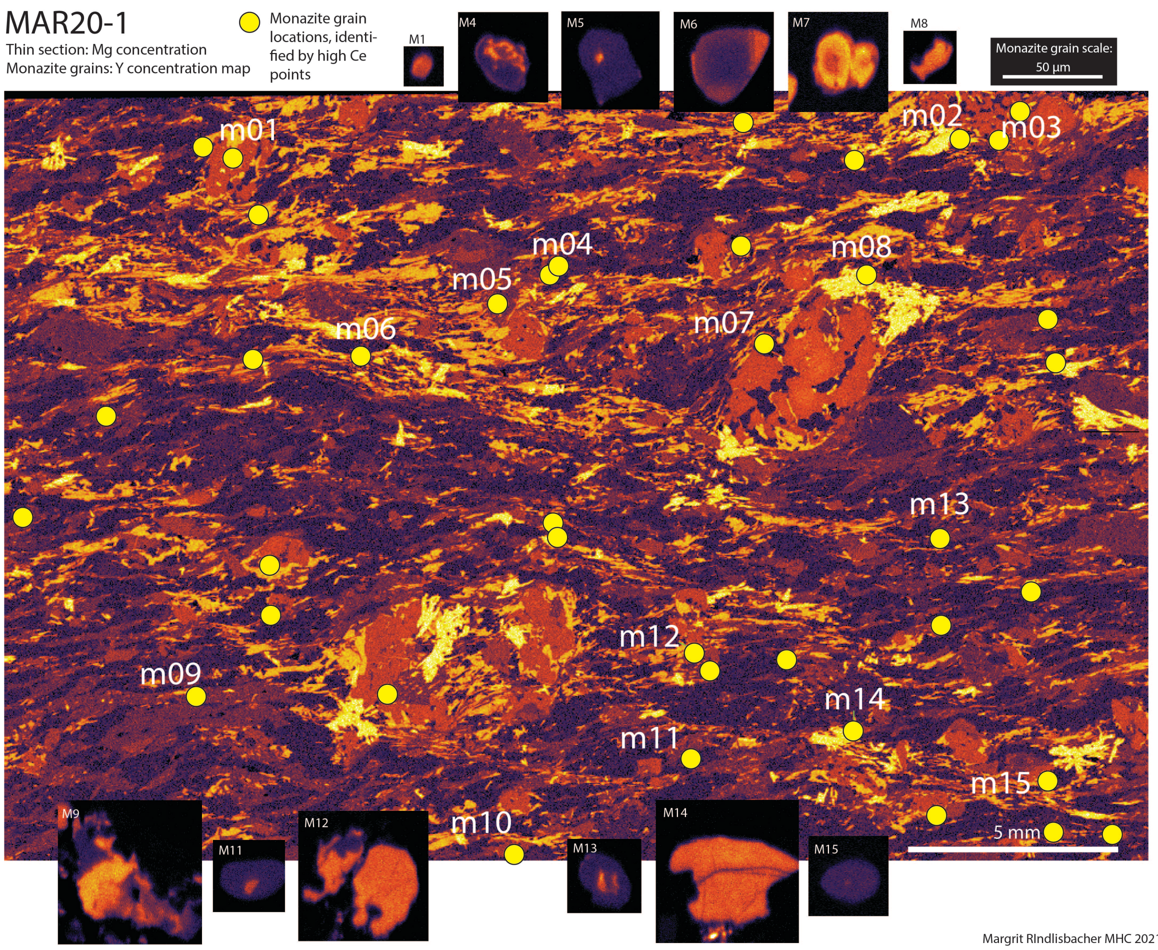

Figure 18: Composite figure of MAR20-1 featuring Y composition maps of the smallest monazite grains. Refer to Fig. 19 for grains larger than ∼100 microns. The whole thin section of MAR20-1 is a Mg element map. Monazite grain locations are indicated with yellow circles.

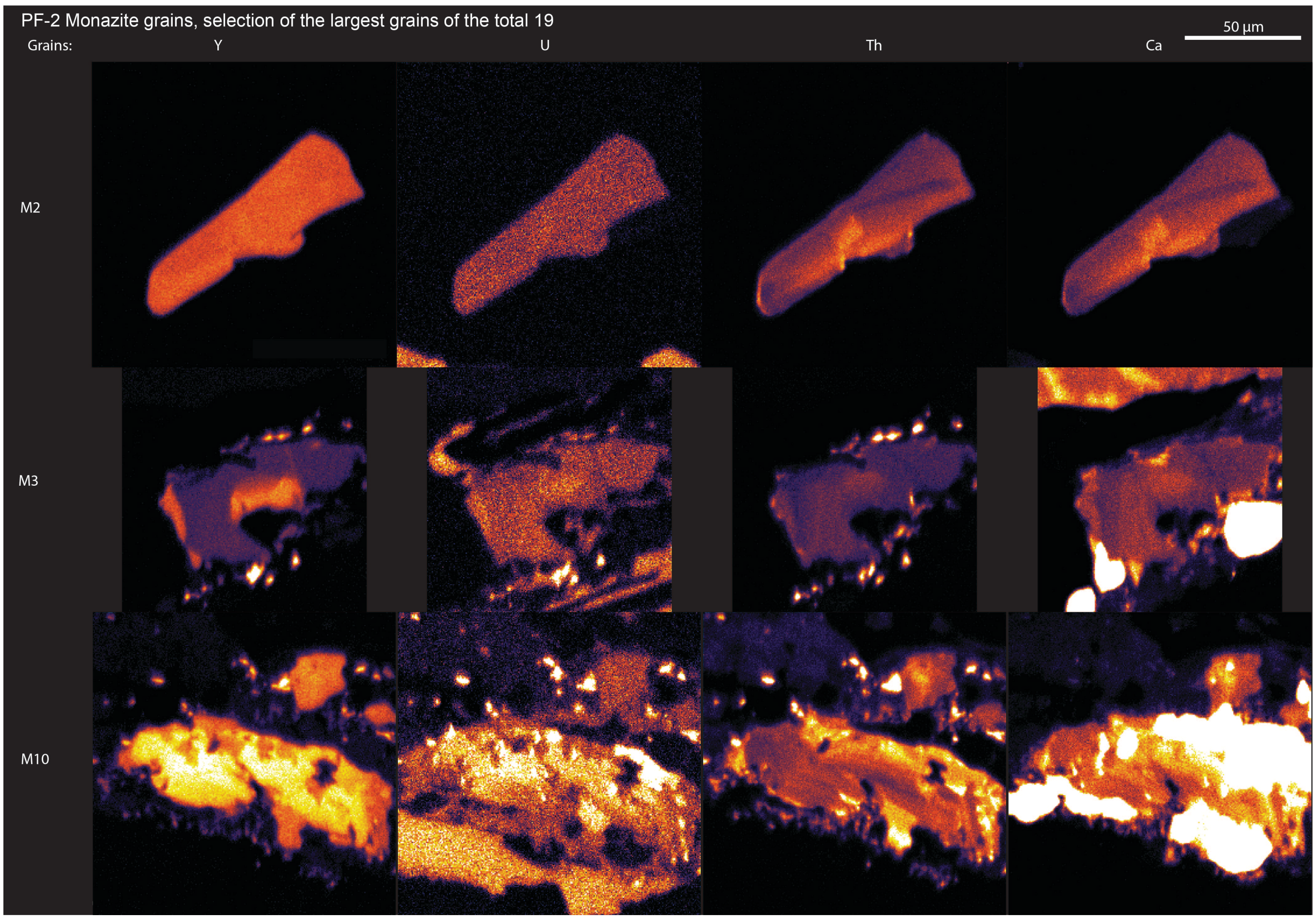

Figure 19: Figure 18: The largest monazite grains from MAR20-1. Y, U, Th, and Ca maps for M2, M3, and M10 are featured.

High inner core dates consist of two data points, one from M1 at 382 ± 2.3 Ma, and one from M10 at 384 ± 2.9 Ma. Graph includes all the norm-distribution plots with one young date excluded from the weighted mean calculation, which consistently resulted in a "main" low-Y age of 373 Ma. Inner core data is highly concentrated, while main and rim dates are more widespread (Fig. 21).

For MAR20-1, 9 analysis points from low Y "main" domains gave a date of 370 ± 5 Ma. 8 total analysis points from outer core domains were dated to be 372 ± 3 Ma. 5 total analysis points from high Y inner rims were dated to be 288 ± 4 Ma. The inner rims of monazite grains in MAR20-1 are some of the youngest dates calculated from these samples. The data from all these domains are similarly concentrated, though the outer core domain has 2 data points with standard deviations greater than 10 (Fig. 22).

4.4 Sources of Young Dates

Young monazite dates from MAR20-1 were taken from M2, M12, and M14. In M2, the analysis point is located in a high Y, low Th, low Ca domain. In M12, the analysis point is located in a high Y, low Th, low Ca domain. In M14, one analysis point is located in a high Y, low Th, low Ca domain and the other is located in a high Y, high Th, high Ca domain. M2, M12, and M14 lack the highly irregular Y-composition textures observed in other grains. All three grains are characterized by uniformly high Y content throughout the grain (See appendix, Fig. 43, 44).

Young monazite dates from BE17-2 were taken from M9 and M17. In M9, the analysis point is located in the high Y, low Th, low Ca rim on the left side of the grain. In M17, the analysis point is also located in the high Y, low Th, low Ca rim on the bottom of the grain. Both M9 and M17 have simple Y-composition domains consisting of a low Y core and a thin high Y rim (Fig. 31, 32). These grains also lack the highly irregular Y-composition textures observed in other grains.

4.5 Results of Theriak Domino Pseudosections

The P-T pseudosections from Theriak-Domino show the equilibrium assemblages for these samples corresponding to the whole rock composition of each sample (Table 1). For BE17-2 (Fig. 23) and for PF-2 (Fig. 24), the mineral assemblage, garnet + feldspar + biotite + sillimanite + quartz, is constrained by the absence of staurolite and orthopyroxene. The resulting stability field for sample BE17-2 requires temperatures greater than about 600°C and pressures greater than 3.5 kbar. PF-2 is constrained to a temperature greater than about 650°C and a pressure greater than about 5 kbar. The pseudosections for these samples show stability fields for "white mica" (muscovite allowing for solid solution with paragonite and phengite) at lower temperatures than the peak assemblage. This is consistent with the appearance of retrograde muscovite on the sillimanite porphyroblasts (Fig. 10), although the white mica field for sample PF-2 appears at a higher pressure than the retrograde path would be expected to take.

The pseudosection for MAR20-1 shows the stability field for the equilibrium assemblage

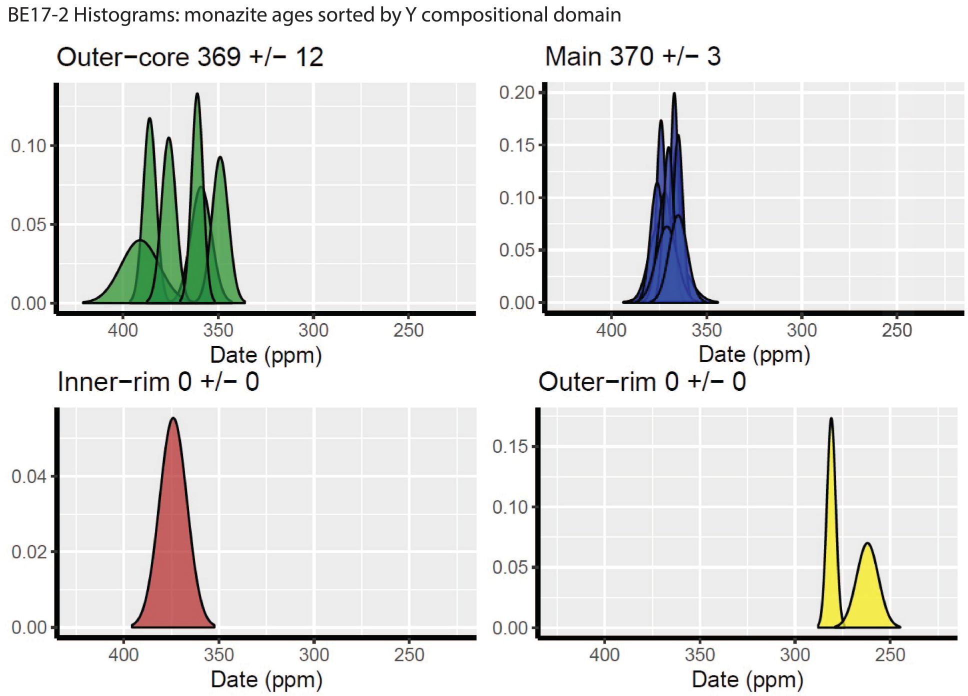

Figure 20: Histograms of monazite age data from BE17-2 (Table 2, see appendix), sorted by domain. Compiled by Dr. Mike Williams at the University of Massachusetts Amherst.

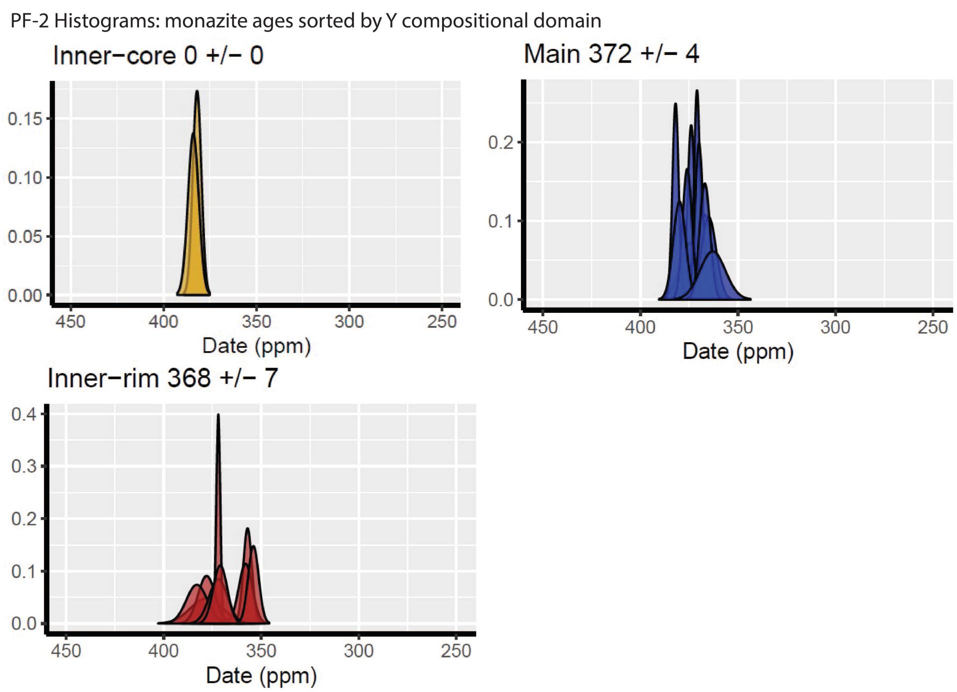

Figure 21: Histograms of monazite age data from PF-2A (Table 3, see appendix), sorted by domain. Compiled by Dr. Mike Williams at the University of Massachusetts Amherst.

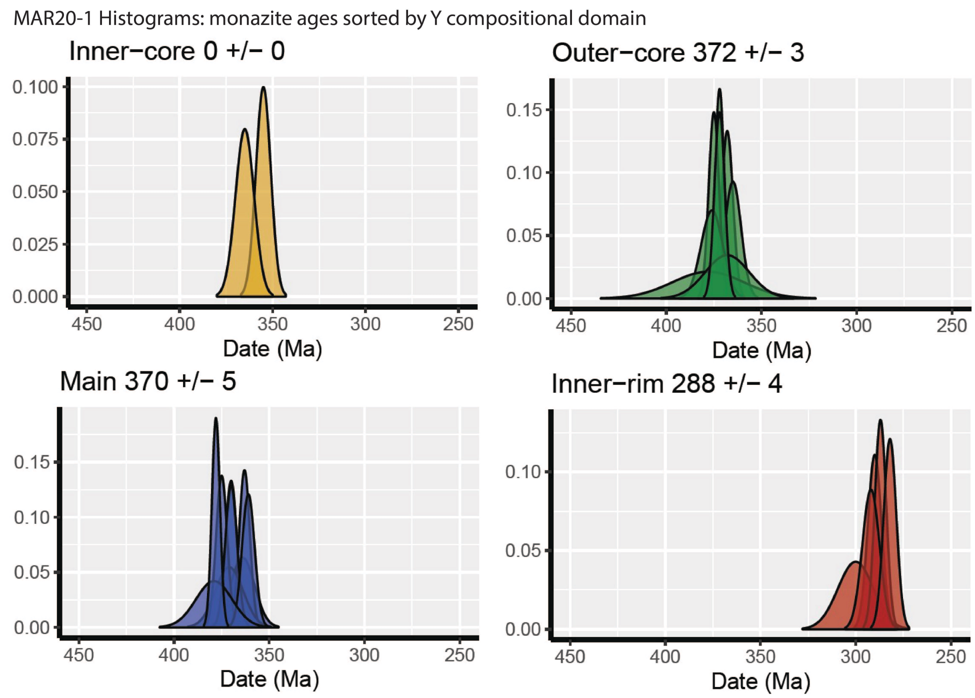

Figure 22: Histograms of monazite age data from MAR20-1 (Table 4, see appendix), sorted by domain. Compiled by Dr. Mike Williams at the University of Massachusetts Amherst.

garnet + feldspar + biotite + white mica + staurolite + sillimanite + quartz (Fig. 25). The presence of staurolite constrains the stability field to a smaller area relative to that of BE17-2 and PF-2. This assemblage is constrained by the sillimanite-to-kyanite reaction on the lower-temperature side, the sillimanite-to-andalusite reaction at low temperature, and the staurolite-out reaction on the higher-temperature side. The peak metamorphic assemblage appears stable over a temperature range of 500-700°C and a pressure range of 3.5-8 kbar. The white mica stability field is greatly expanded for the composition of MAR20-1 relative to BE17-2 and PF-2. White mica (muscovite) is sensitive to the H_2O content of a rock because muscovite + quartz break down at lower temperatures under dry conditions. However, because the H_2O content was held at 4.25% in all of these calculations, the difference is likely due to greater K_2O in MAR20-1 than in the other two.

5 Interpretation

5.1 Contextualization of the Date Data

The age of the Belchertown igneous intrusion was determined to be 380 ± 5 m.y from U-Th-Pb zircon age dating (Ashwal 1979). Robinson (2016) mentions a ∼380 Ma for the age of the schist septum, calculated using monazite dating (Robinson 2016). Our dates of ∼370 Ma for the schist septum are largely consistent with these previously calculated dates. We interpret this to indicate that monazite crystallization occurred simultaneously with the contact metamorphism from the Belchertown intrusion. Given that the Partridge Formation

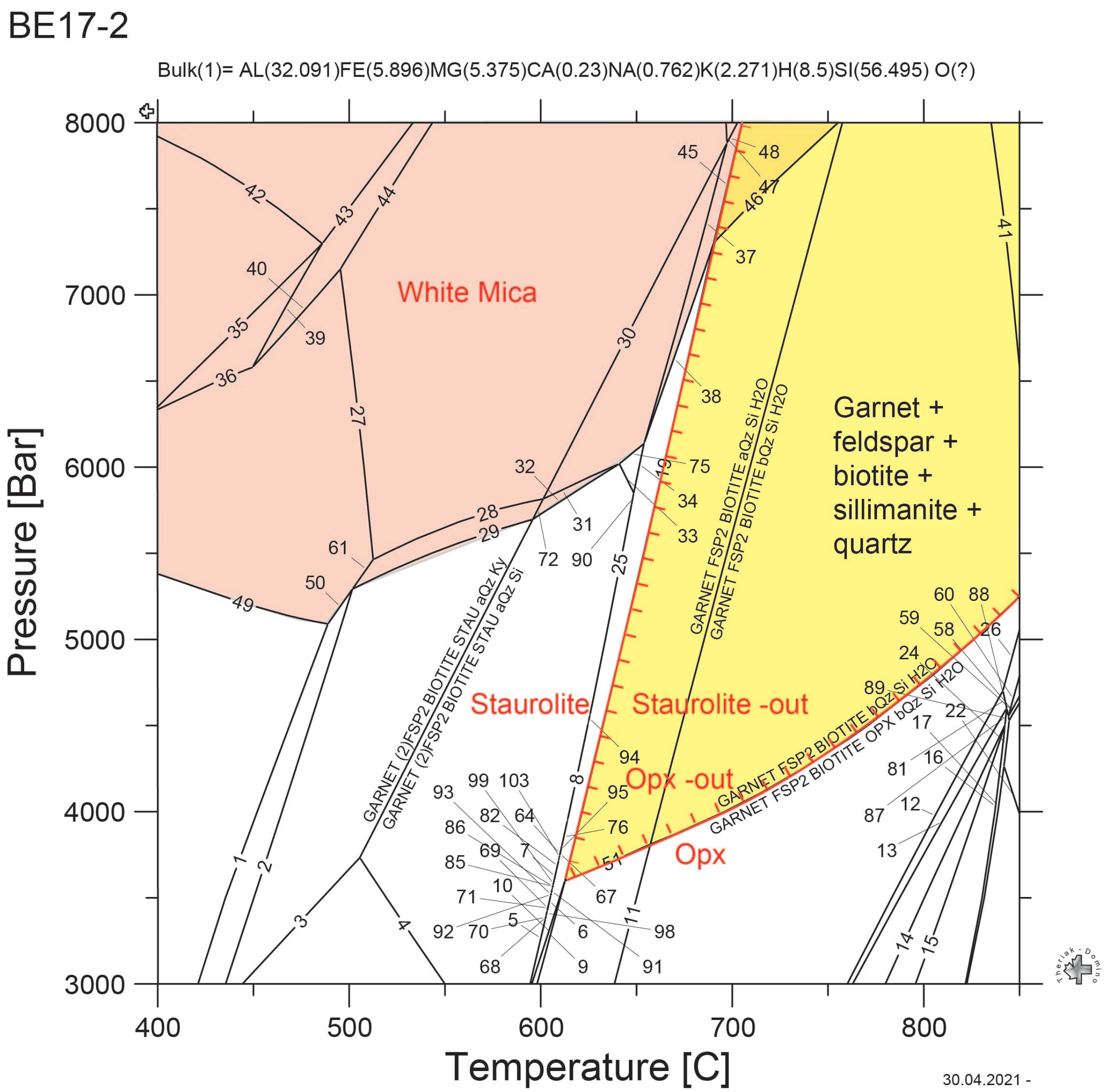

Figure 23: The pseudosection for BE17-2 shows the equilibrium assemblages given the whole rock composition of BE17-2. The assemblage garnet + feldspar + biotite + sillimanite (highlighted in yellow), being the minerals found in BE17-2, exists at temperatures greater than 600°C and pressures greater than 3.5 kbar. The limiting reactions are the staurolite out and orthopyroxene in reactions. The stability field for white mica (muscovite) is shown in pink. This calculation assumes 4.25% H_2O and unlimited oxygen.

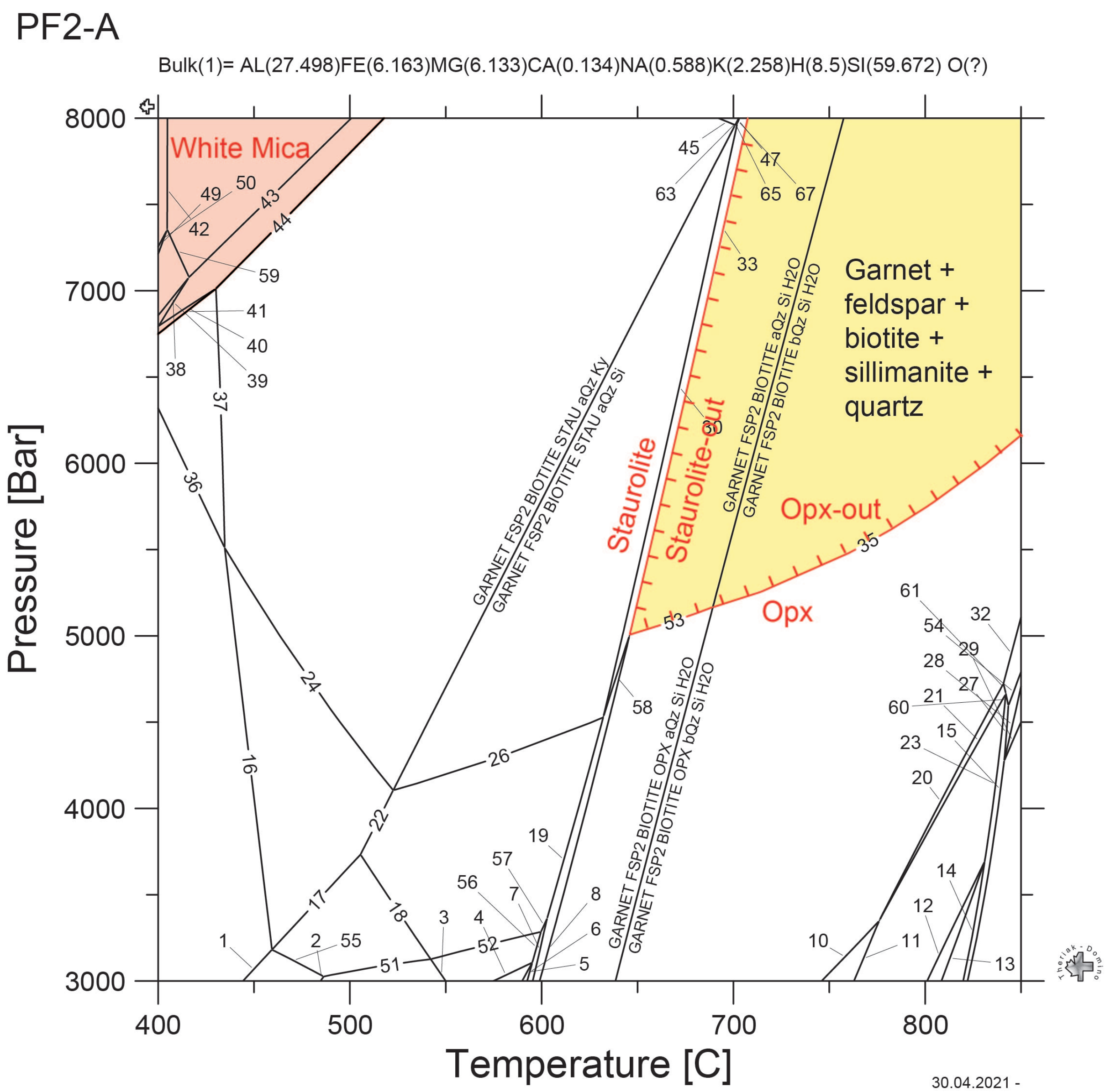

Figure 24: The pseudosection for PF-2 shows the equilibrium assemblages given the whole rock composition of PF-2. The assemblage garnet + feldspar + biotite + sillimanite (highlighted in yellow), being the minerals found in PF-2, exists at temperatures greater than 625°C and pressures greater than 5 kbar. The limiting reactions are the staurolite out and orthopyroxene in reactions. The stability field for white mica (muscovite) is shown in pink. This calculation assumes 4.25% H_2O and unlimited oxygen.

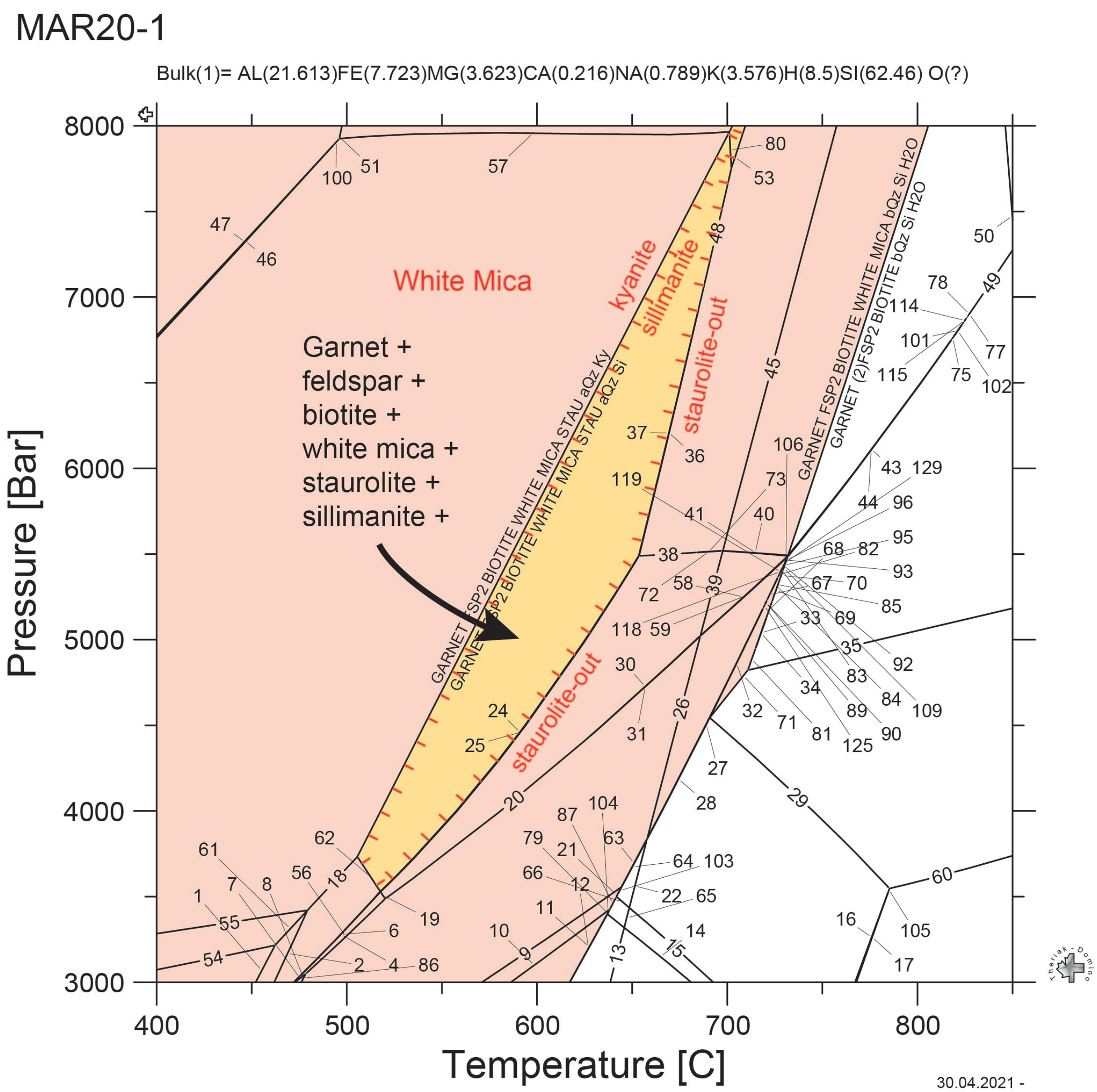

Figure 25: The pseudosection for MAR20-1 shows the equilibrium assemblages given the whole rock composition of MAR20-1. The assemblage garnet + feldspar + biotite + white mica + staurolite + sillimanite, being the minerals found in MAR20-1, exists over a temperature range of 500-700°C and a pressure range of 3.5-8 kbar. The limiting reactions are the sillimanite in and staurolite out reactions. The stability field for white mica (muscovite) is shown in pink. This calculation assumes 4.25% H_2O and unlimited oxygen.

Cation:	BE17-2	MAR20-1	PF-1	PF-2
Si	57.16	63.23	75.65	60.38
Ti	1.16	0.86	0.76	1.21
Al	27.54	21.87	14.76	23.60
Fe	7.93	6.87	4.92	8.29
Mn	0.08	0.09	0.05	0.08
Mg	3.65	4.18	2.26	4.16
Ca	0.22	0.32	0.12	0.13
Na	0.40	0.56	0.26	0.31
K	1.80	1.94	1.18	1.79
P	0.06	0.08	0.04	0.05
Total:	100.00	100.00	100.00	100.00

Table 1: Whole rock composition (wt%) for samples BE17-2, MAR20-1, PF-1, and PF-2. Data collected on October 6, 2020.

is composed of metamorphosed sediment accreted in the Middle Ordivician, we expected to observe some inherited monazite grains that record dates from this time period. However, this hypothesis was not supported by our data as no ages were older than the Devonian.

We interpret the younger, Permian ages calculated for some grains in MAR20-1 and BE17-2, ranging from 262 Ma to 292 Ma, to represent a second monazite growth event. We could find no consistent correlation between mineral associations with monazite grains, monazite grain texture and shape, and the much younger ages. Nevertheless, the occurrence of multiple grains all dating to the Permian over a range of 20 Ma in two separate samples indicates that this event is significant. The timing of this event places it within the Alleghanian orogeny. Robinson et al., 1992, recognize Alleghanian deformation and metamorphism in the Northfield syncline of north-central Massachusetts. Mike Williams (pers. comm. with Prof. Steve Dunn) reports similar ages in the Pelham Dome just to the north of Belchertown.

5.2 Chemical Domains in Monazite Grains

Compositional domains in monazite grains can be used to identify distinct periods of monazite growth. Williams et al. 2017 mapped monazite grains from a retrograde felsic granulite (sample S32D) from the Legs Lake shear zone, Athabasca area, Canada. Y composition maps of monazite grains reveal compositional domains that are cleaner and more regular than the monazite grains from our study. The same is true for the Y composition maps of monazite from Markley et al. (2018). Y compositional maps for a paragneiss (16TG-154 Swede Mountain) from Williams et al. 2019 are more similar to our data in terms of domain definition, but lack the highly irregular textures apparent in our samples.

Further insight is gained when compositional domains are contextualized with the location of the grains themselves in the thin section. Grains that are located within porphyroblasts either predate the crystallization of the porphyroblast or have grown simultaneously with growth of the porphyroblast. The majority of the monazite grains in BE17-2, PF-2, and MAR20-1 occur distributed throughout the matrix of the rock, and not located in any porphyroblasts. Exceptions to this include M11 in BE17-2, located in a sillimanite porphyroblast (Fig. 14), which was dated to be 372 3.8 ± Ma.

Chemical domains may also be used to associate growth periods of monazite with those of other minerals. For example, changes in Y content can correlate with different episodes of garnet growth in a metamorphic rock. During crystallization, garnet will preferentially accept Y and other HREE into its mineral structure (Pyle et al. 2001, Williams et al. 2007, Martins et al. 2009, Markley et al. 2018, Williams et al. 2019, Allaz et al. 2020). As a result, low-Y monazite can be indicative of monazite growth simultaneous with or after garnet growth (Williams et al. 2007, Markley et al. 2018, Williams et al. 2019). As garnet breaks down, it will release Y into the system (Williams et al. 2019). Thus, high-Y monazite zones can be interpreted as periods of growth that either predate garnet crystallization or occur simultaneously with garnet deterioration.

Major domain patterns in all three samples have been identified: low Y core and mantle with a high Y rim, high Y core with a low Y mantle and a high Y rim, and high Y in all domains (Fig. 26). Examples of the low Y core and mantle with a high Y rim zoning pattern include M9, M15, and M17 in BE17, and M3 and M7 in PF-2, and M6 in MAR20-1 (See appendix for catalogue of monazite chemical maps). We interpret these grains to have begun crystallization in the presence of garnet and the rims to have formed simultaneous with garnet deterioration. Examples of the high Y core with a low Y mantle and a high Y rim zoning pattern include M1, M11, and M16 in PF-2 (See appendix). We interpret these grains to have initially crystallized prior to garnet crystallization, grew further in the presence of garnet, and had a final growth event simultaneous with garnet deterioration. Examples of the high Y in all domains zoning patterns include M6 and M16 in BE17-2, M8 in PF-2, and M2, M12, and M14 in MAR20-1 (See appendix). We interpret this domain pattern to indicate complete monazite growth entirely predating garnet crystallization or postdating garnet deterioration. Regardless of this correlation of monazite growth events to garnet, calculated ages for growth events represented by chemical domains date them to the same time period within the Devonian.

Young Permian dates from BE17-2 and MAR20-1 were taken from domains with high Y concentration. In MAR20-1, the monazite grains, M2, M12, and M14, have homogenous high Y concentration. In BE17-1, both young dates were taken from high Y rim. We interpret these dates to record a monazite growth event that coincided with garnet being retrograded. While we do not know the pressure and temperature of the event, the high Y in the monazite grains suggests growth in coincidence with garnet consumption. The Alleghenian event may have included these conditions.

5.3 Monazite as a Solid Solution

Monazite belongs to the monazite group of minerals with three endmembers: monazite ($CePO_4$),brabantite [$CaTh(PO_4)_2$], and huttonite ($ThSiO_4$) (Forster and Harlov 1999, Forster 2005). Continuous solid solution between monazite and brabantite is suggested by natural minerals, which are referred to as cheralite (Forster and Harlov 1999, Forster 2005).

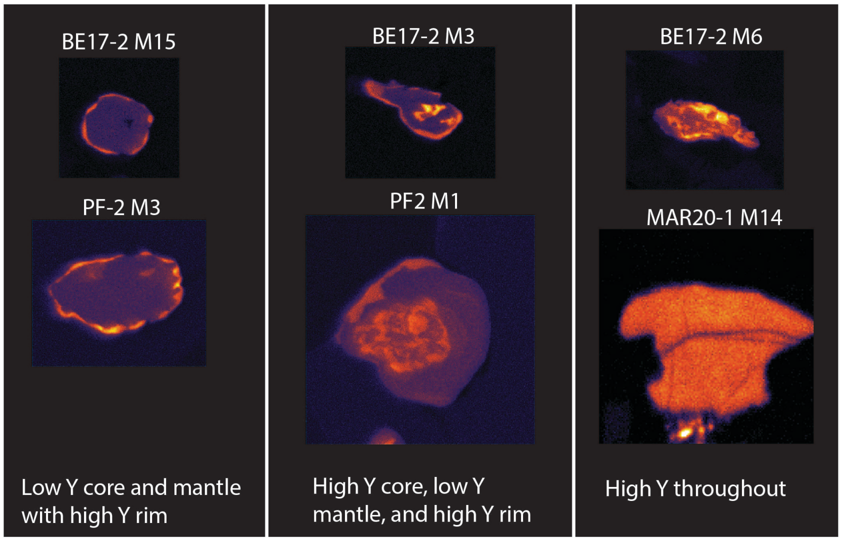

Figure 26: Examples of major compositional domain patterns seen in the monazite grains. Monazite maps show Y composition.

Intermediate monazite-huttonite minerals are referred to as huttonic monazite (Forster and Harlov 1999, Forster 2005).

Fig. 27 plots formula proportions of $(Th + U + Si)$ vs. $(REE + Y + P)$ for all analysis points in BE17-2, PF-2, and MAR20-1, normalized to 16 O atoms. Monazite composition for all samples is very close to endmember monazite ($CePO_4$), which lies at the lower right corner of Fig. 27. Pyle et al. (2001) plot formula proportions for monazite and xenotime and find that the brabantite substitution vector is dominant for monazite. Plots from Forster (1998) also observe that most monazite analyses plot closely along the brabantite substitution vector, with only a few analyses plotting close to the huttonite substitution vector. Analysis points for PF-2 plot closest to the brabantite substitution vector, while points from MAR20-1 plot closest to the huttonite substitution vector. For BE17-2, points closest to endmember monazite plot closer to brabantite, while points further from endmember plot closer to huttonite.

BE17-2 and MAR20-1 feature clusters of points that plot closer to endmember monazite than the rest of the data (Fig. 27). We observe no trends between grain location, element concentration, or calculated age of each analysis point and the composition of the monazite.

5.4 Evidence for Fluid Alteration Event

Patchy Y and Th textures on many of the monazite grains lead us to believe that the Partridge Formation schist septum suffered at least one fluid alteration event. Williams et al. (2019) report patchy monazite compositions in a sample that experienced fluid alteration in the Adirondacks. This patchy texture characteristic to fluid crystallization is shown in Layer 3 of Fig. 28.

Patchy textures of compositional domains in monazite can be interpreted as the result

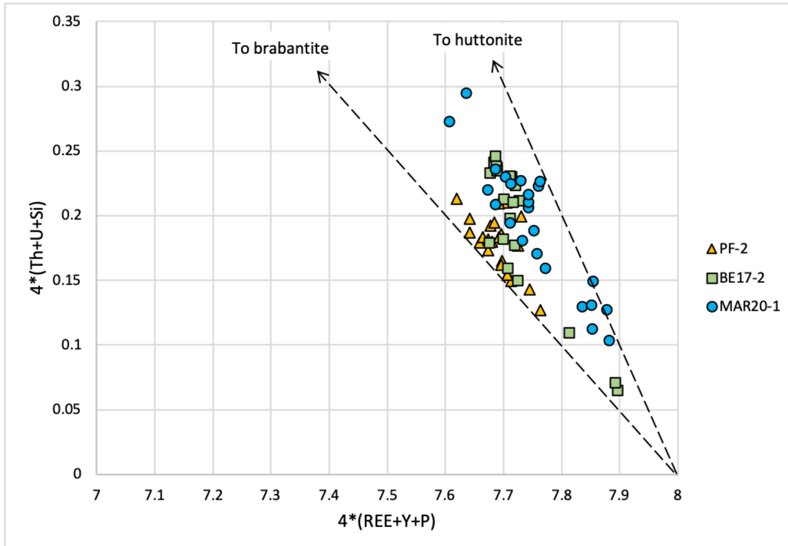

Figure 27: A plot of formula proportions $(Th + U + Si)$ vs. $(REE + Y + P)$ for BE17-2, PF-2, and MAR20-1, normalized to 16 O atoms. Brabantite $[CaTh(PO_4)_2]$, and huttonite $(THSiO_4)$ exchange vectors are featured. Brabantite has a 2 : 1 exchange with monazite, while huttonite has a 1 : 1 exchange, as indicated by mineral formulas. Endmember monazite $(CePO_4)$ plots at x=8.0.

of fluid alteration (Cherniak and Pyle 2008, Williams et al. 2011, Williams et al. 2017). Fluids can reset the U-Th-Pb system in monazite through dissolution-precipitation reactions, resulting in ages that may be inconsistent with the mineral assemblage and other geochronometer indicators (Cherniak and Pyle 2008, Williams et al. 2017). Harlov and Hetherington (2010) showed experimentally that Th and Pb could be removed during alteration by alkaline fluids. Reset compositional domains typically are composed of end-member monazite and characteristically contain less Th than unaltered monazite (Williams et al. 2011, Williams et al. 2017).

Altered monazite grains display a variety of textures. BSE images mapping for Th reveal several trends of the altered domains locations: lobate zones primarily at grain boundaries, around inclusions and fractures, and patchy zones with little to no structural or crystallographic control (Williams et al. 2011). Ca and Y are reduced in the altered domains, while U and Pb are absent (Williams et al. 2011). The lack of U, Pb, and Th is reflected in the reduced ages of these altered regions (Williams et al. 2011). Altered Th domains in monazite are interpreted to be the result of fluid mediated coupled dissolution-reprecipitation (Williams et al. 2011). Th substitution is huttonite-type substitution $(Th^{4+} + Si^{4+} = REE^{3+} + P^{5+})$ (Williams et al. 2011). Once in contact with the fluids, dissolution of the monazite releases Th into solution (Harlov and Hetherington 2010). Partial dissolution of the monazite occurs simultaneously with reprecipitation of altered monazite that is depleted in U, Pb, Th, Y, Nd, and Ca (Harlov and Hetherington 2010, Williams et al. 2011).

Regarding our samples, the composition of the patchy areas in monazite grains are consistent with the chemical effects of fluid mediated dissolution-reprecipitation reactions. Areas of grains displaying patchy Y texture are also depleted in Th and Ca (Fig. 29). In M1 from PF-2, areas depleted in Th correspond almost exactly with areas depleted in Ca (Fig. 29).

Some individual monazite grains have dates from different chemical domains that are confusing or hard to explain. Specifically, in some cases, the ages of what we interpret to be late stage rims are older than the cores. M11 and M16 in PF-2 are examples of this (Fig. 37). For M16, the apparent difference in age is greater than the combined standard deviations, i.e. the uncertainties, of the ages. We observe that the cores with the younger ages often also display the patchy Y texture that we interpret to be the result of a fluid alteration event. We speculate that the young dates are the consequence of the resetting of the U-Th-Pb system associated with fluid alteration in monazite. More work is needed to fully investigate the implications of these dates.

Given that the majority of the grains with these patchy textures have Devonian ages, we interpret the fluid alteration event to have occurred simultaneously with or shortly after the contact metamorphism with the Belchertown pluton. The wider distribution of dates from the outer-rims of PF-2 contain a cluster at 350-355 Ma (Fig. 21). This could be the fluid alteration event that resulted in the patchy texture in Y compositional domains of many of the grains. A likely source for the fluid that caused this alteration would be a water-rich fluid expelled from the magma near the end of crystallization of the Belchertown pluton. The presence of albitization of plagioclase observed in MAR20-1B (Fig. 13) also provides evidence for fluid alteration by an alkaline (Na-bearing) fluid.

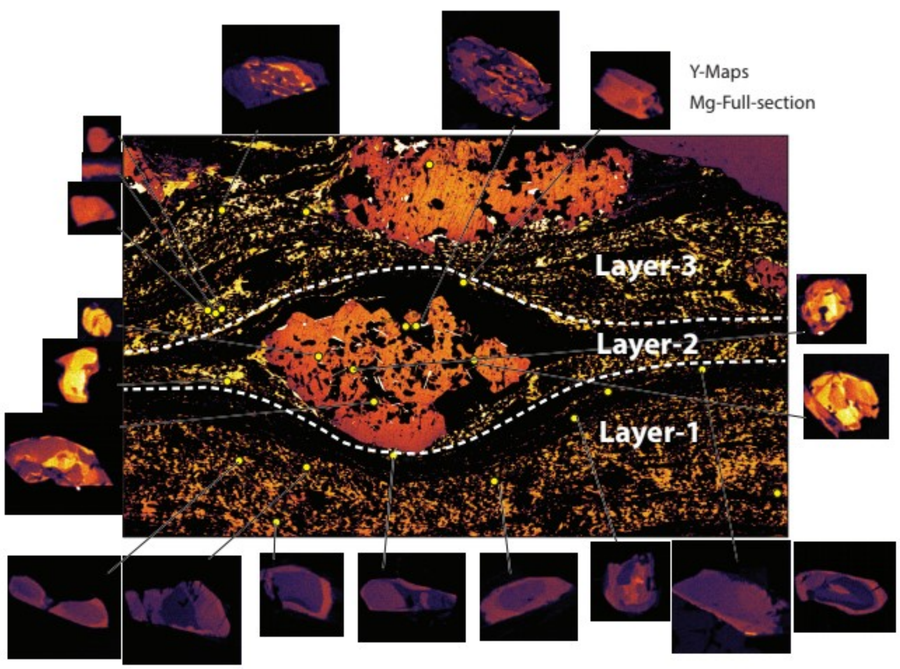

Figure 28: Altered monazite grains in layer 3 from Adirondack Mountains sample showing characteristic patchy Y composition texture. Figure taken from Williams et al. 2017.

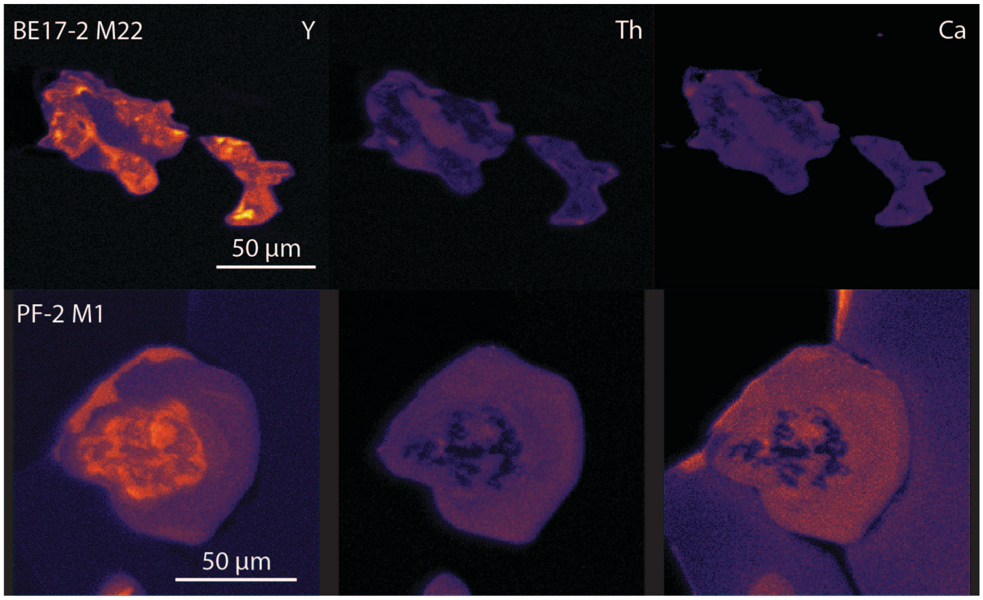

Figure 29: Examples of patchy Y, Th, and Ca texture in select monazite grains from BE17-2 and PF-2.

5.5 Interpretation of Theriak Domino Pseudosections

If we accept the results from the Theriak-domino calculations, then it is likely that the pressure of equilibration is greater than about 5 kbar, the minimum pressure for sample PF2, as the other samples have ranges that also extend above 5 kbar (Fig. 30). We might reasonably assume that all samples experienced the same pressure of metamorphism. Even though it is not required that all samples recrystallized at the same pressure, there is no reason to conclude otherwise. Thus, we conclude a pressure greater than 5 kbar for these samples.

The temperature stability range for MAR20-1 is lower than that of BE17-2 and PF-2 (Fig. 30). The coincidence of the upper temperature for MAR20-1 and lower temperature for PF2 and BE17-1 is due to the staurolite out reaction, which varies only slightly with sample composition. The more schistose character of MAR20-1 due to the abundant muscovite and biotite in this sample contrasts with the more gneissic texture of BE17-2 and PF-2. This can be explained by the expanded stability field of white mica for the composition of MAR20-1, but is also consistent with MAR20-1 being of lower metamorphic grade than BE17-2 and PF-2. We speculate that BE17-2 and PF-2 represent an area of the septum that was heated to a somewhat higher temperature by the Belchertown igneous intrusion than MAR20-1, and as a result these more gneissic samples experienced muscovite breakdown and the growth of large sillimanite porphyroblasts.

The odd occurrence of what appears to be garnet "coronas" surrounding some sillimanite porphyroblasts is not explained by the pseudosection assemblage fields. Garnet is stable everywhere in these equilibrium assemblage diagrams.

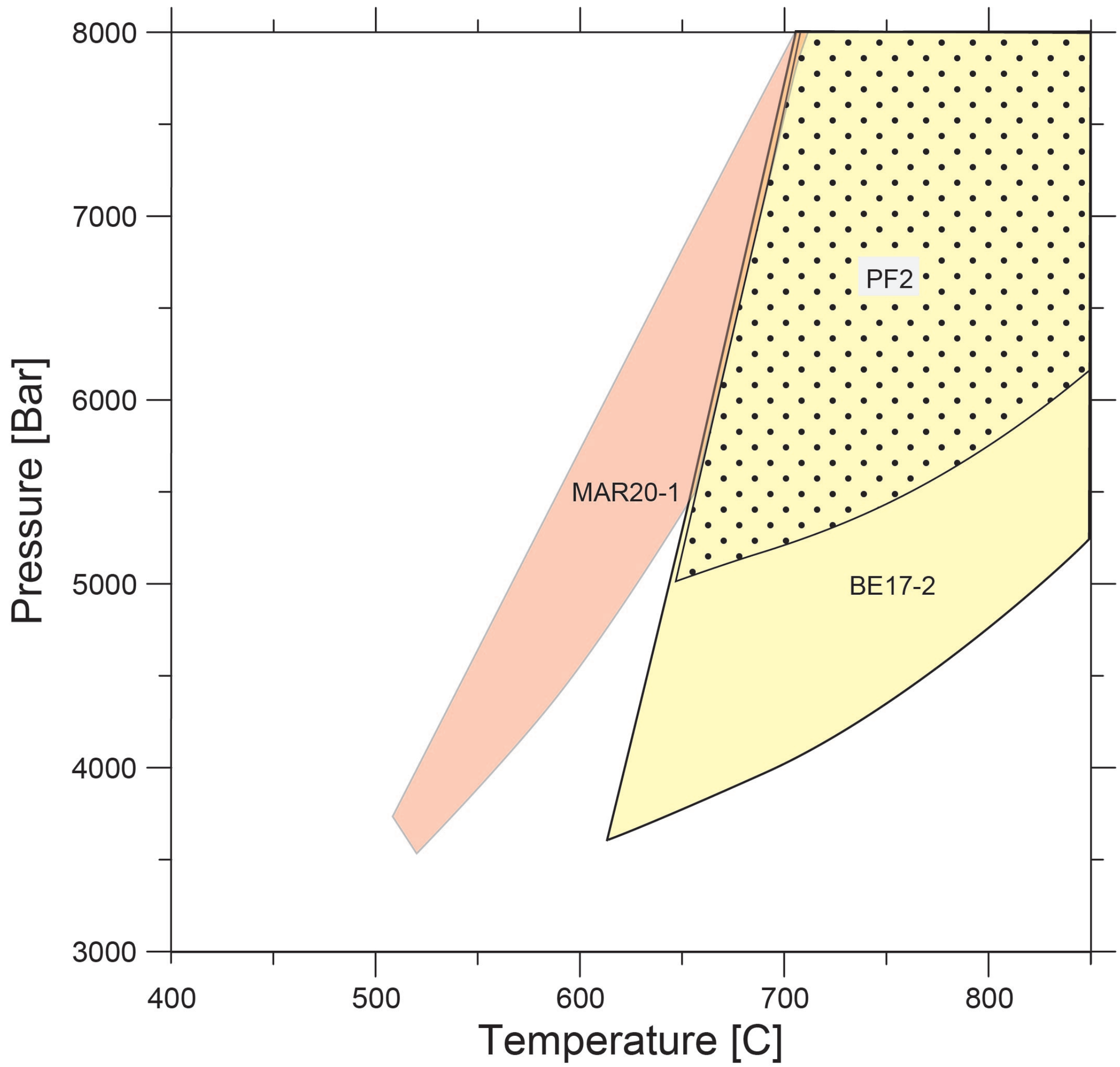

Figure 30: A comparison of the stability fields for BE17-1 (yellow), PF-2 (yellow with dots), and MAR20-1 (pink).

5.6 Additional Notes

Regarding the deformation of the fabric seen especially in MAR20-1, we speculate that fabric development occurred possibly during an earlier phase of the Acadian orogeny, prior to emplacement of the Belchertown complex.

Chiastolites were searched for, but no convincing chiastolite cross structures were found in any of the samples, as would be expected if the sillimanite were pseudomorphs after andalusite.

6 Conclusion

Monazite grains from our samples of Partridge Formation sillimanite gneiss reveal two episodes of monazite growth: the first and far most prevalent, at ~370 Ma in conjunction with the contact metamorphism event from the Belchertown pluton, and the second, at ~280 Ma, during the Alleghanian orogeny. The older cluster of ages appears to be a drawn out or protracted event spanning as much as 10 million years. The data are consistent with a fluid-mediated alteration event near the end of this event. Highly irregular, patchy textures in Y composition maps of these grains are interpreted to be the result of such a fluid-mediated alteration event. Because many grains with this patchy compositional texture show ages in the same range as unaltered grains, it is likely that the proposed fluid alteration event is, at least in part, related to the overall contact metamorphism. Felsic magmas such as the Belchertown complex typically contain several percent water. Release of magmatic water at the end of crystallization of the complex would be a likely source for the fluid that created the patchy-textured monazite grains. Based on pseudosection analysis, we conclude that the pressure of stability for all three samples is greater than 5 kbar, while the temperature stability range for MAR20-1 is lower than that of BE17-2 and PF-2. These rocks display a number of highly interesting features and warrant further study.

7 Future Work

Recommended future work on these samples includes the characterization of minerals adjacent to each monazite grain. We also recommend dating patchy monazites such that a date for a high Y section and an adjacent low Y section are obtained for comparison. Further analysis and photography of these samples with the SEM is also recommended.

A Appendix

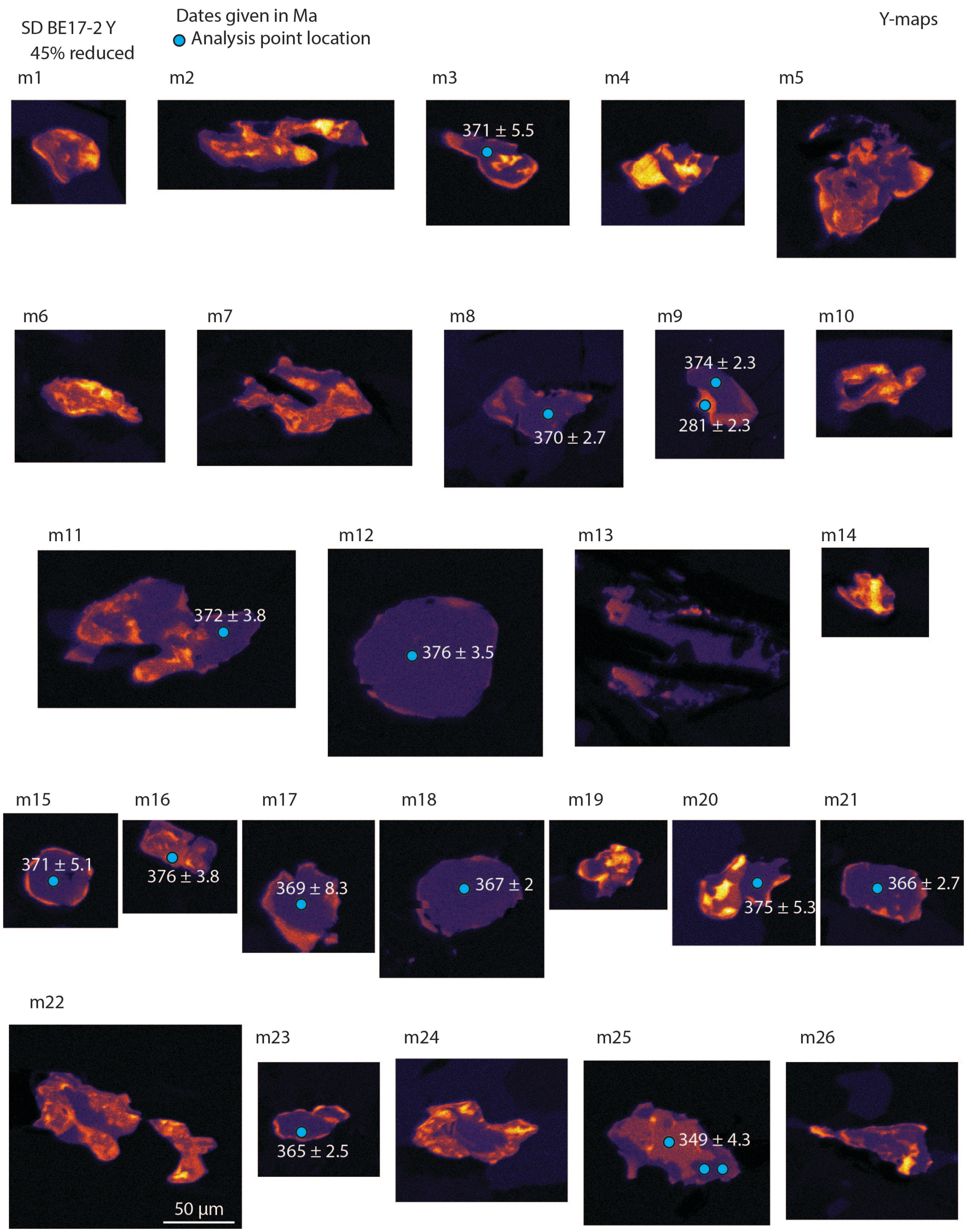

Figure 31: Catalogue of all mapped monazite grains in BE17-2, featuring Y maps and calculated ages for compositional domains. Analysis points of the ages are identified with a blue circle.

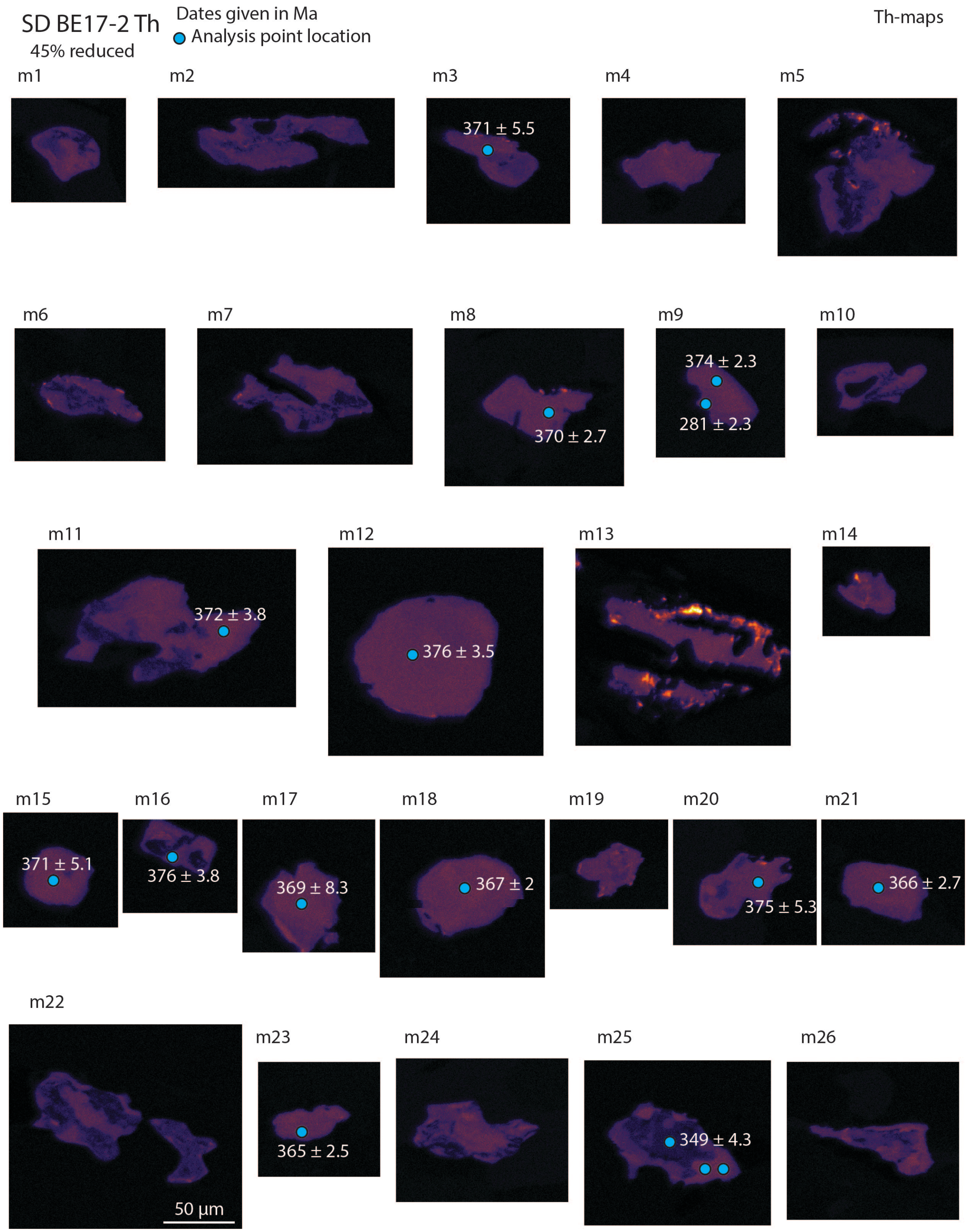

Figure 32: Catalogue of all mapped monazite grains in BE17-2, featuring Th maps and calculated ages for compositional domains. Analysis points of the ages are identified with a blue circle.

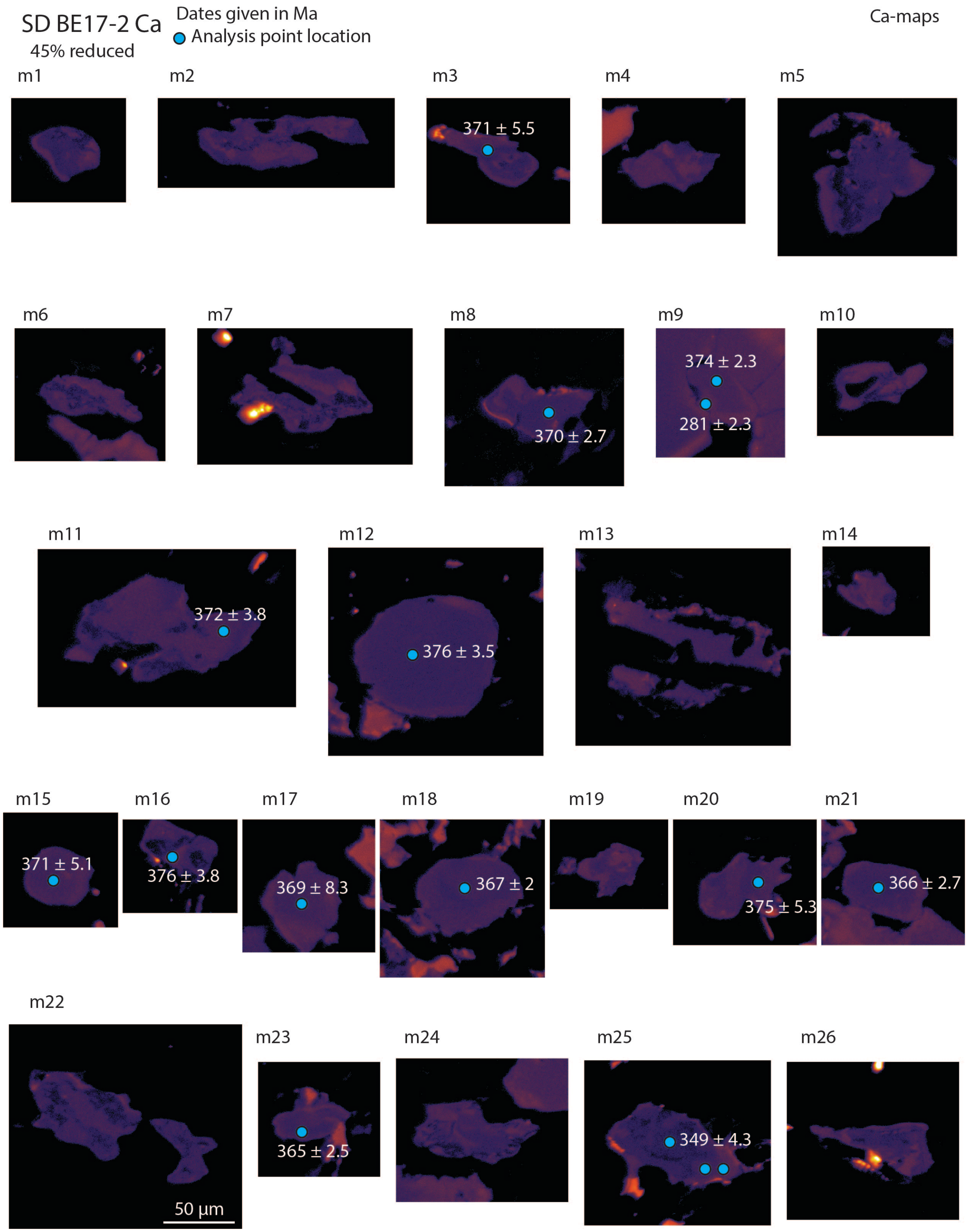

Figure 33: Catalogue of all mapped monazite grains in BE17-2, featuring Ca maps and calculated ages for compositional domains. Analysis points of the ages are identified with a blue circle.

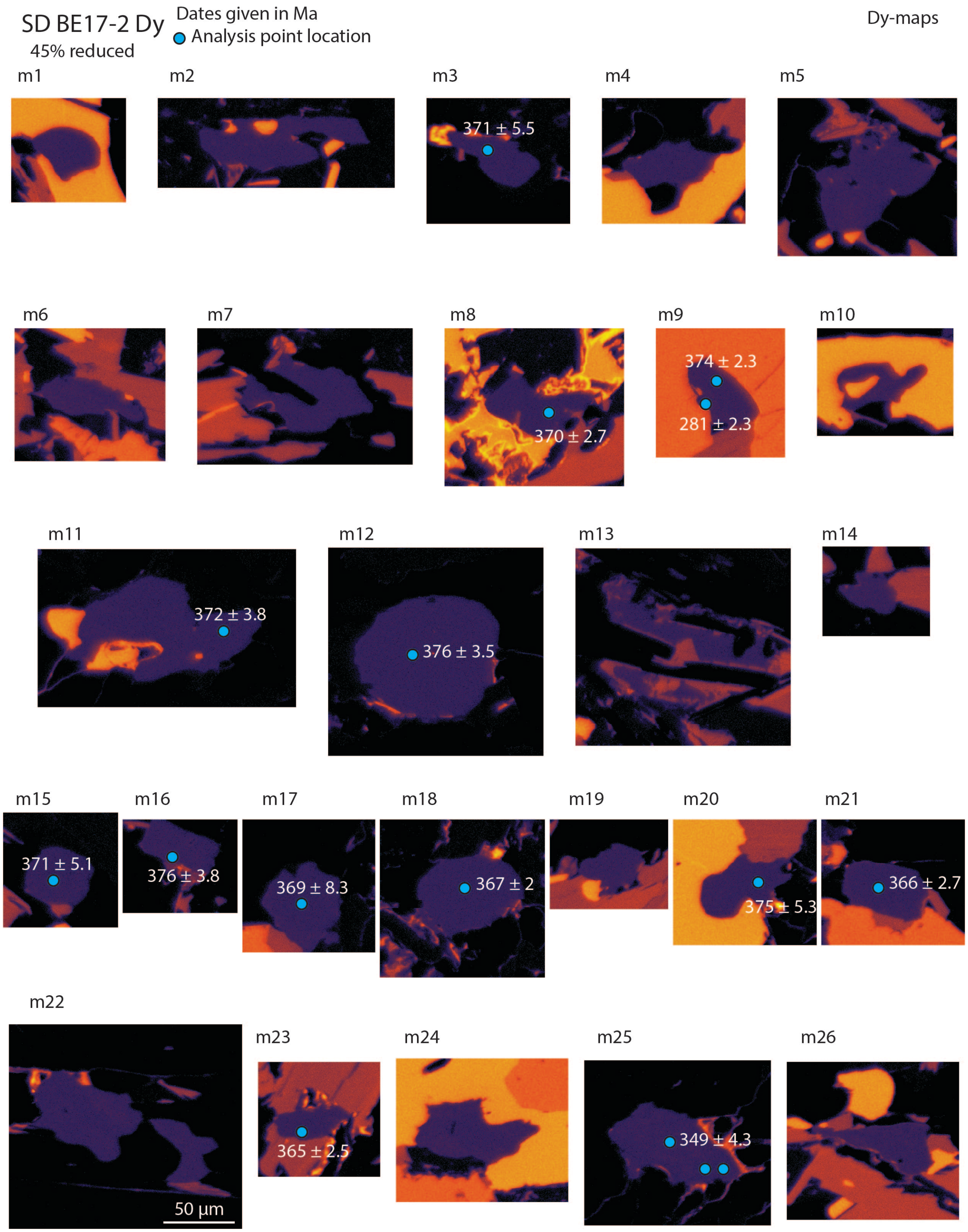

Figure 34: Catalogue of all mapped monazite grains in BE17-2, featuring Dy maps and calculated ages for compositional domains. Analysis points of the ages are identified with a blue circle.

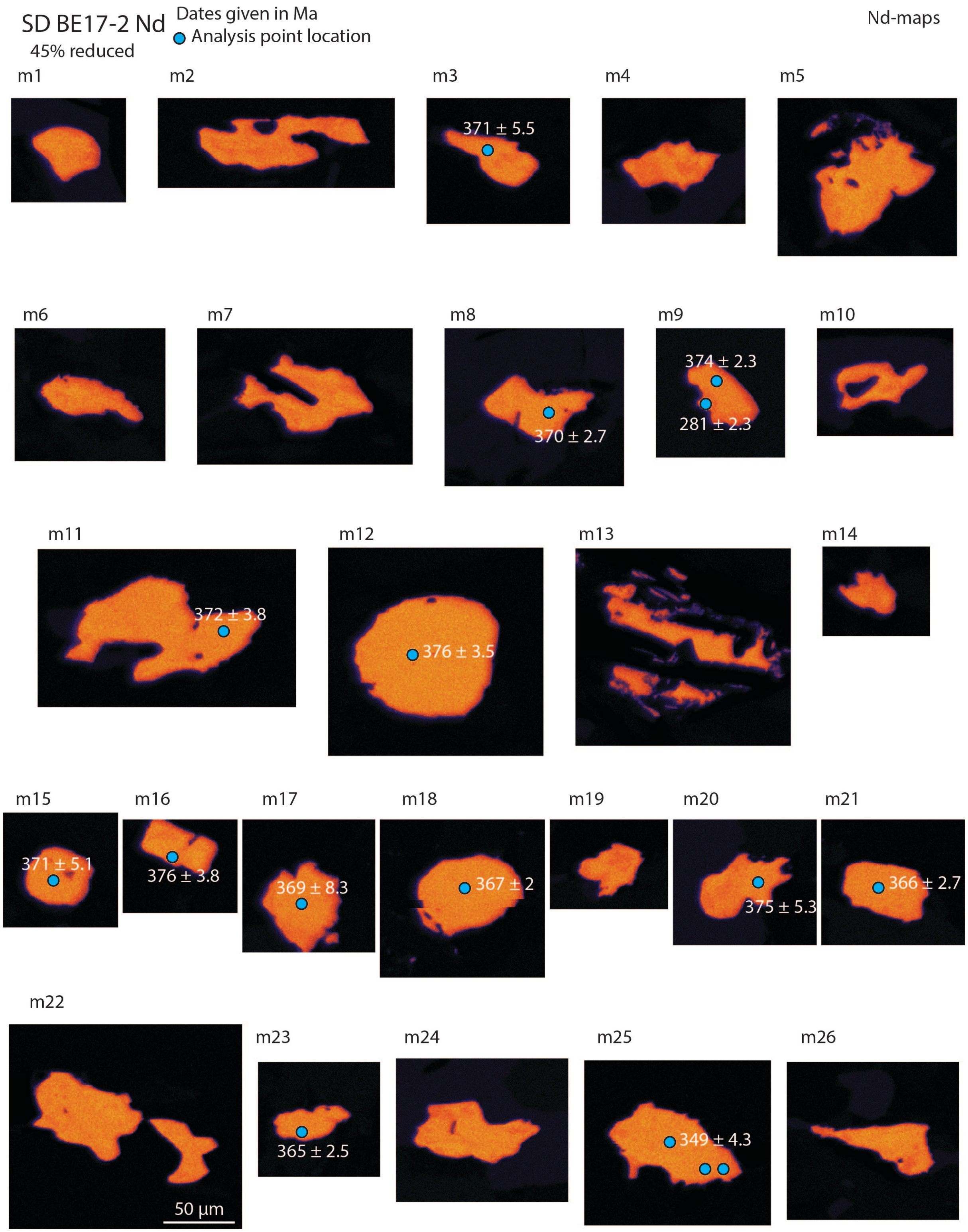

Figure 35: Catalogue of all mapped monazite grains in BE17-2, featuring Nd maps and calculated ages for compositional domains. Analysis points of the ages are identified with a blue circle.

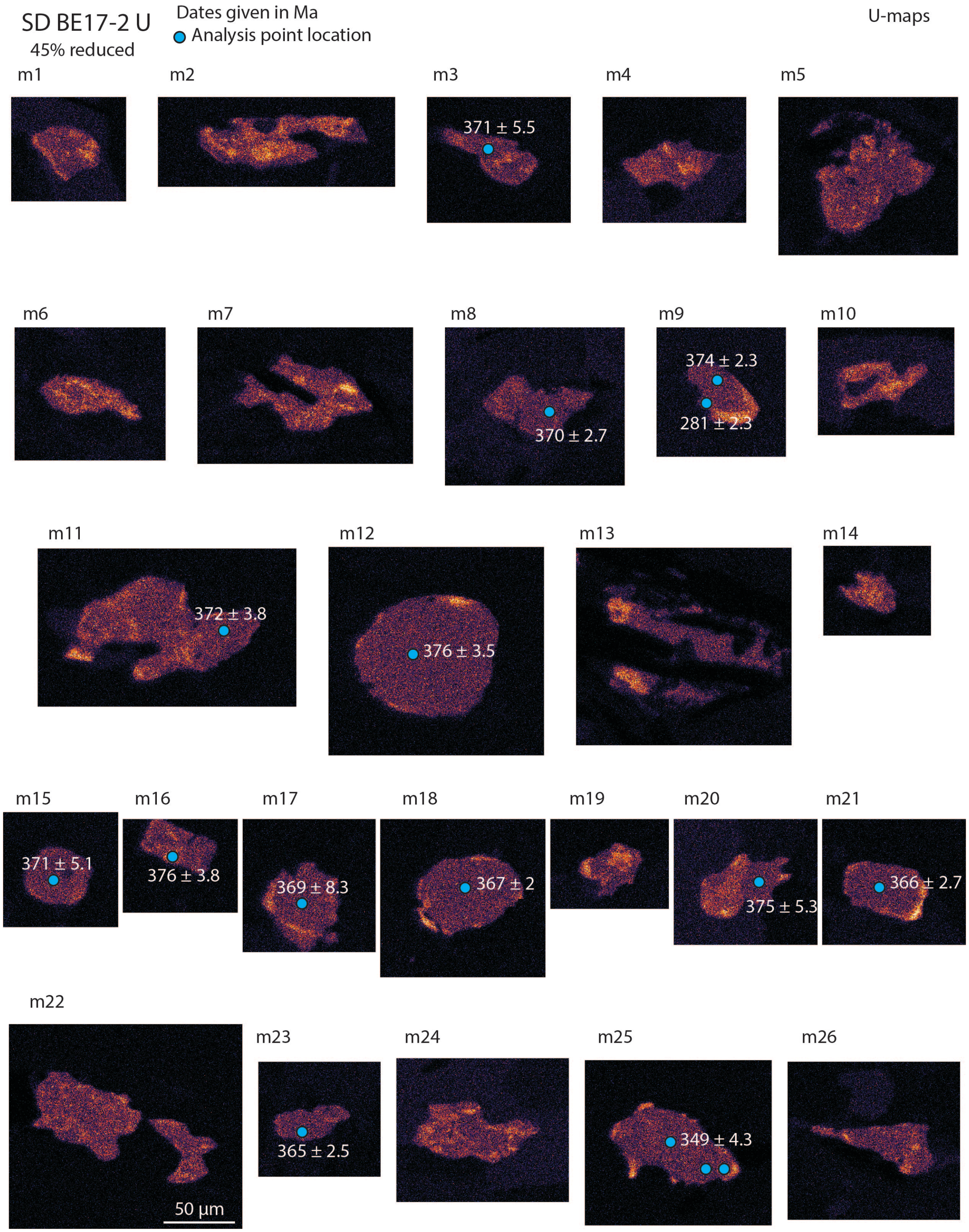

Figure 36: Catalogue of all mapped monazite grains in BE17-2, featuring U maps and calculated ages for compositional domains. Analysis points of the ages are identified with a blue circle.

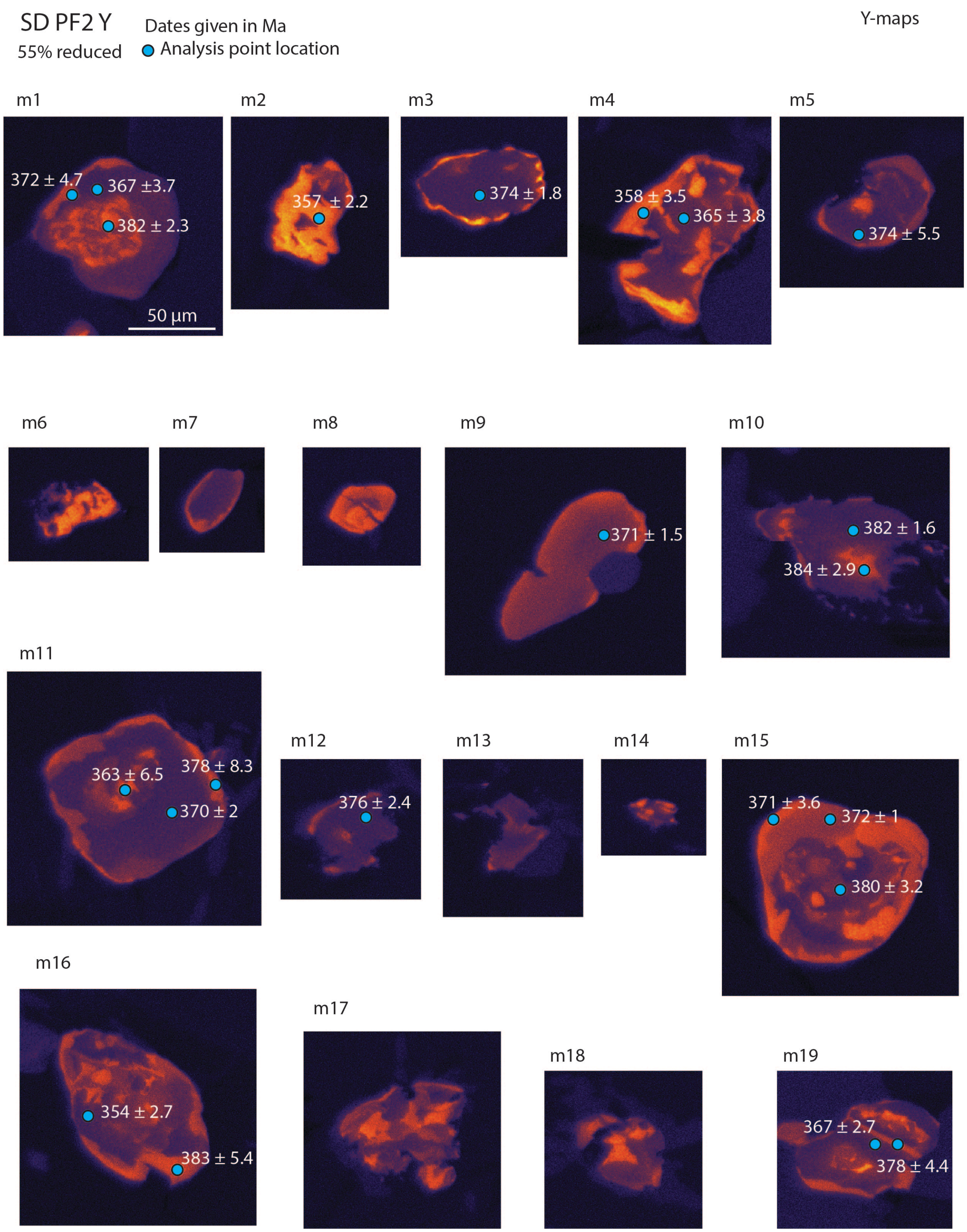

Figure 37: Catalogue of all mapped monazite grains in PF-2, featuring Y maps and calculated ages for compositional domains. Analysis points of the ages are identified with a blue circle.

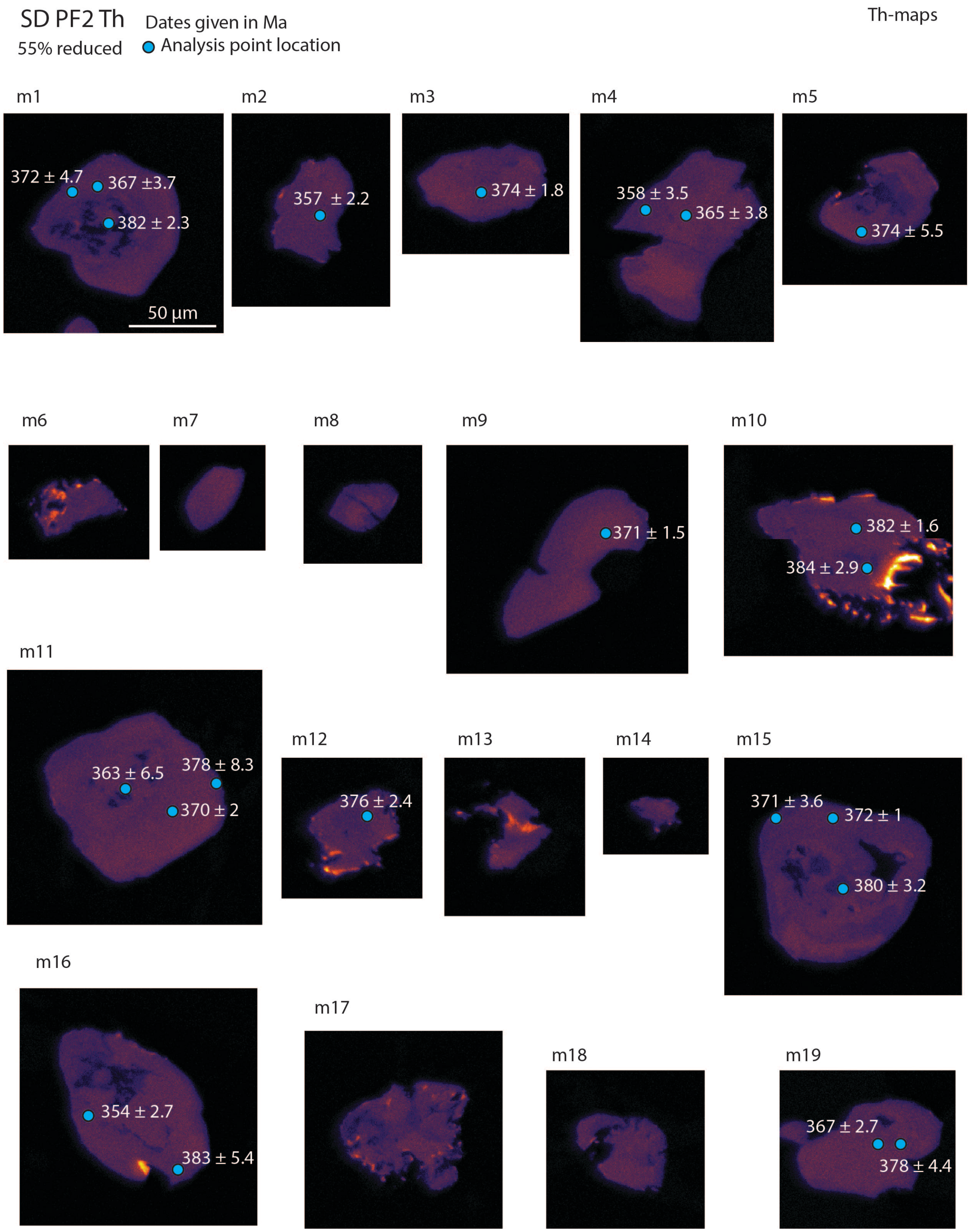

Figure 38: Catalogue of all mapped monazite grains in PF-2, featuring Th maps and calculated ages for compositional domains. Analysis points of the ages are identified with a blue circle.

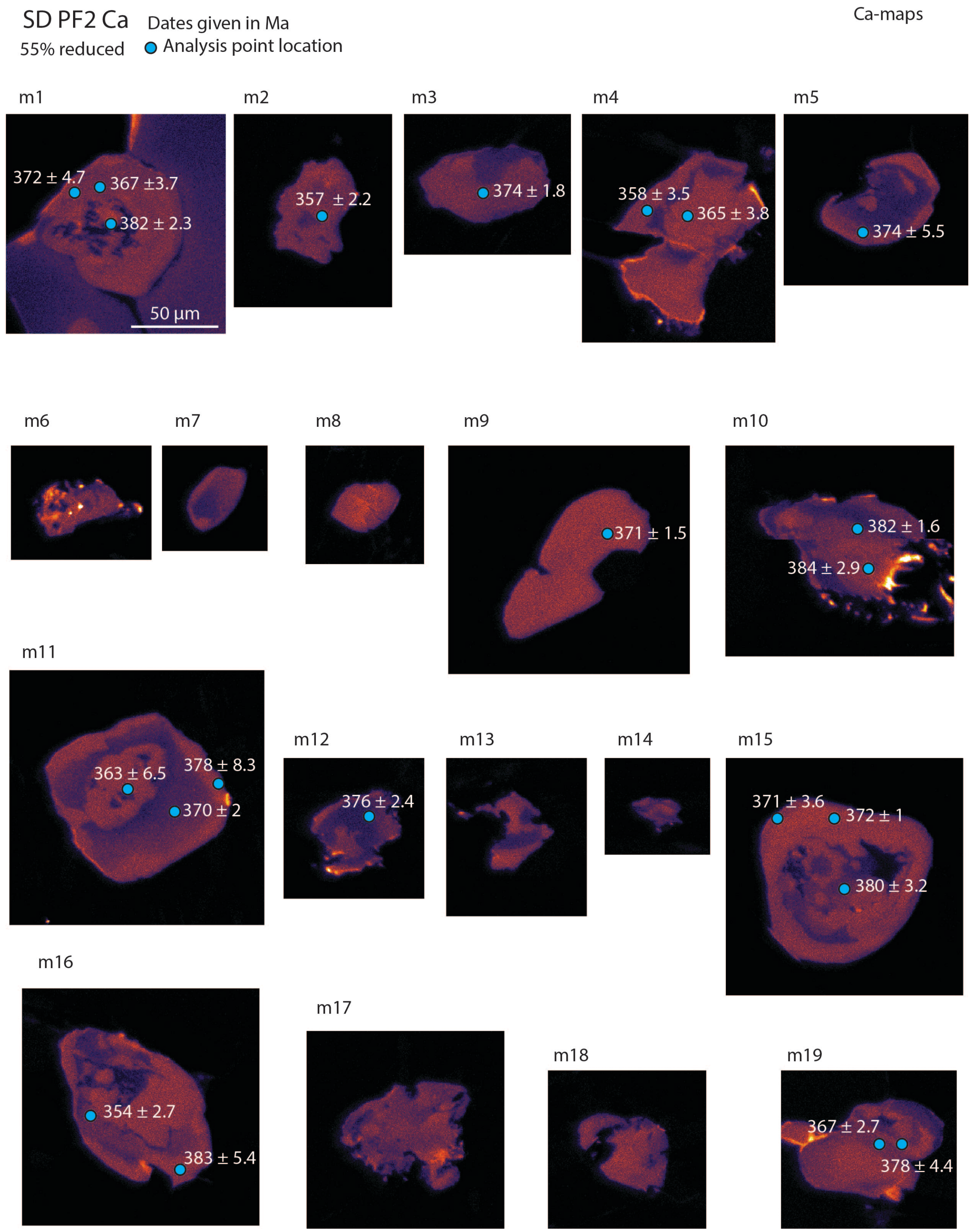

Figure 39: Catalogue of all mapped monazite grains in PF-2, featuring Ca maps and calculated ages for compositional domains. Analysis points of the ages are identified with a blue circle.

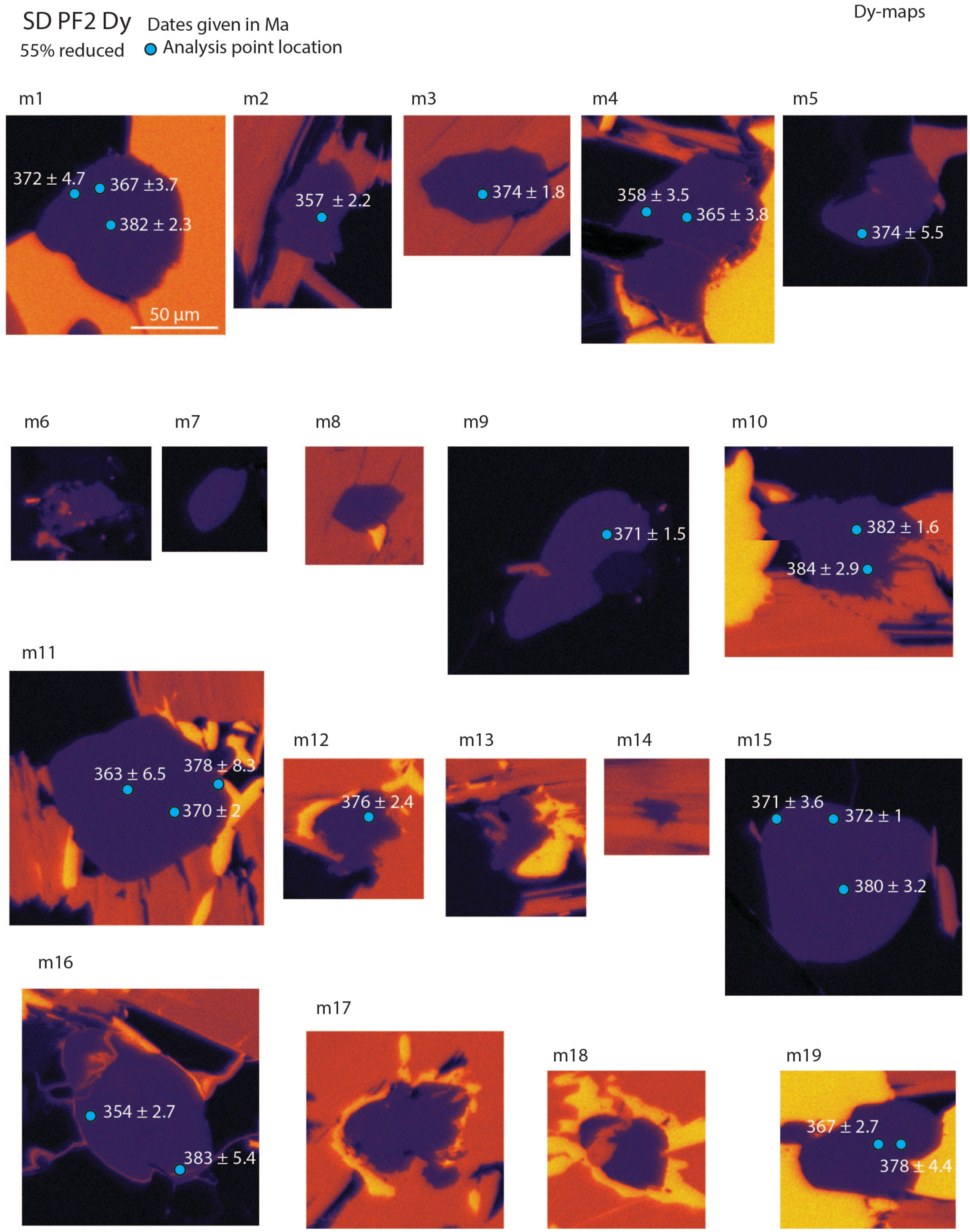

Figure 40: Catalogue of all mapped monazite grains in PF-2, featuring Dy maps and calculated ages for compositional domains. Analysis points of the ages are identified with a blue circle.

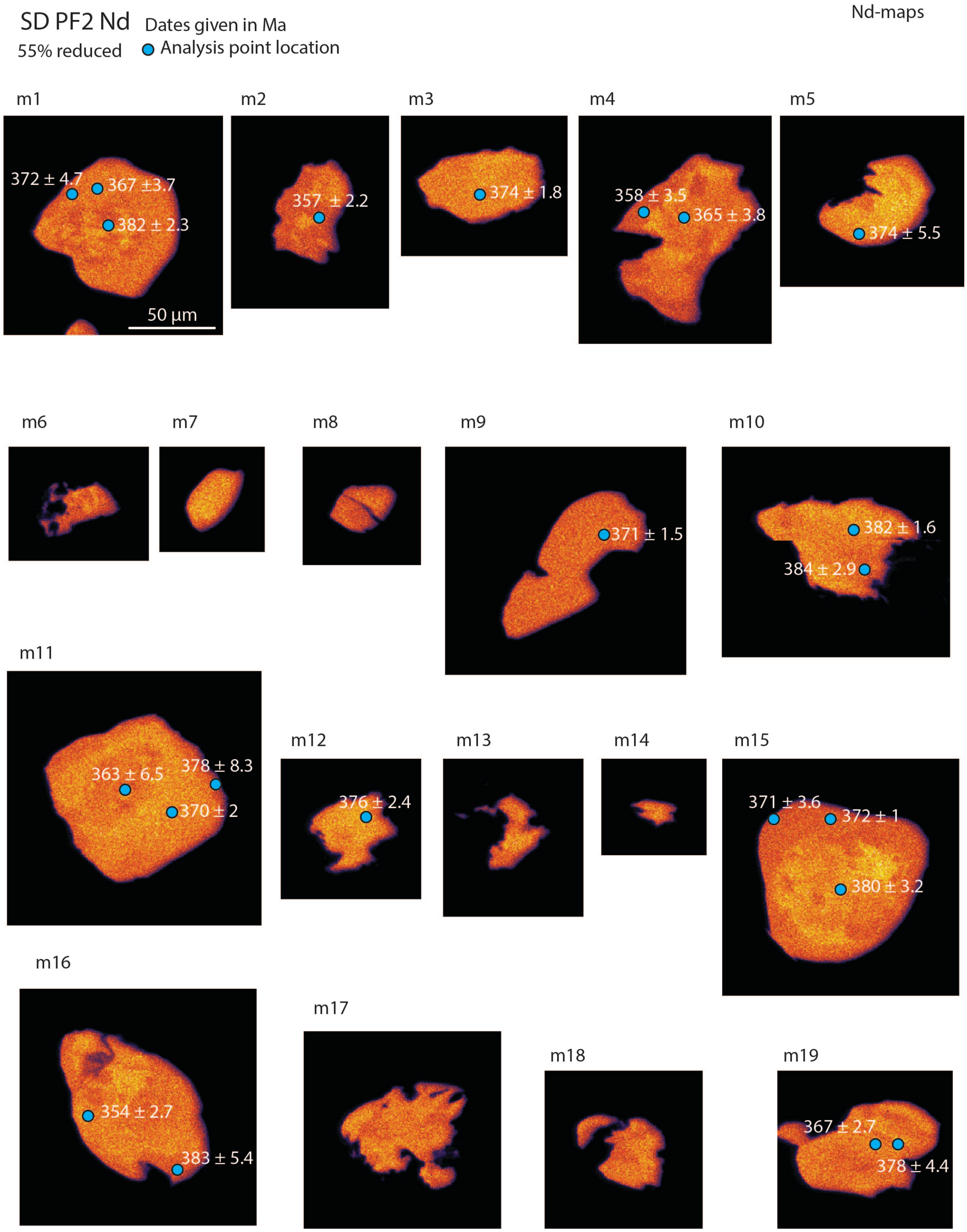

Figure 41: Catalogue of all mapped monazite grains in PF-2, featuring Nd maps and calculated ages for compositional domains. Analysis points of the ages are identified with a blue circle.

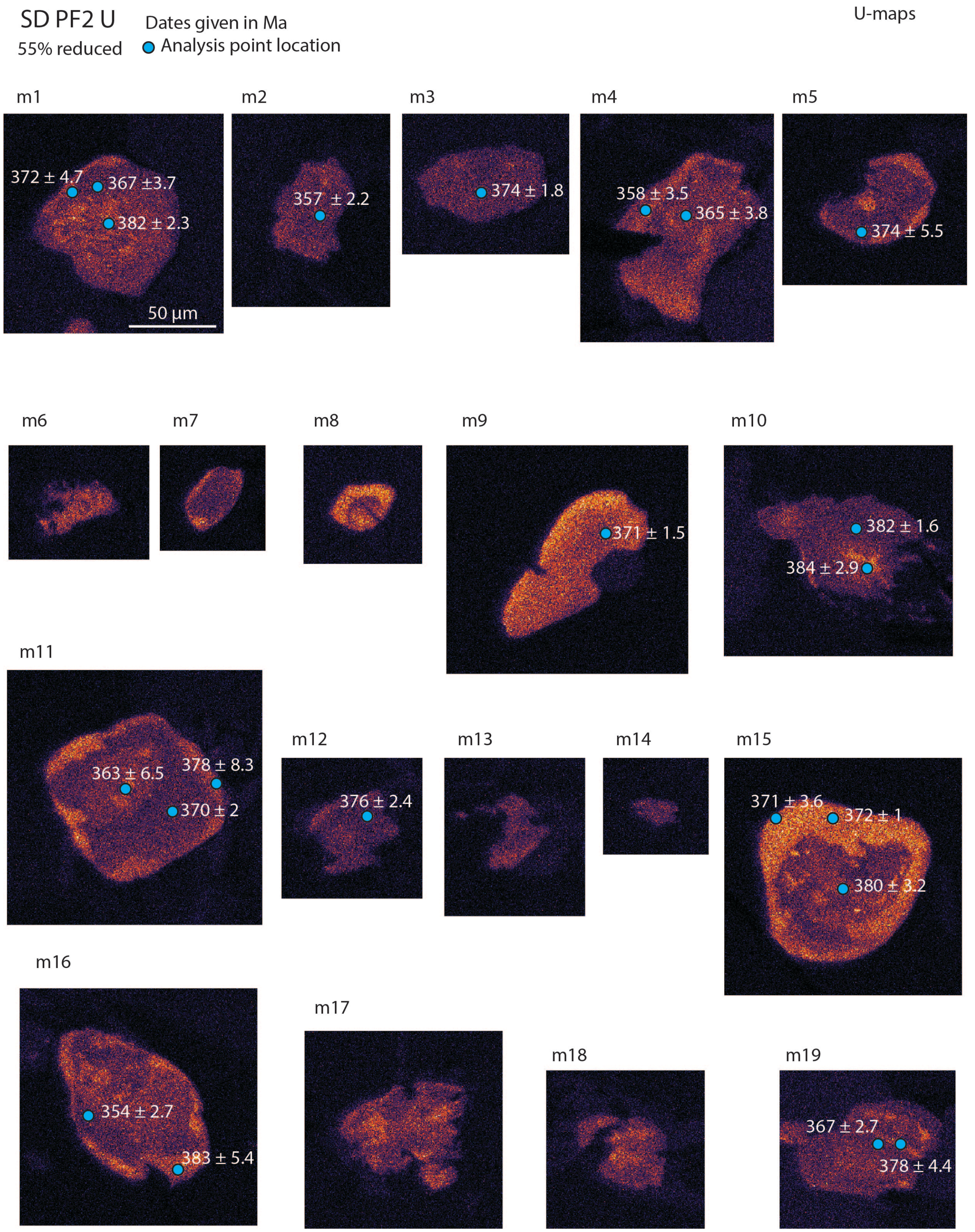

Figure 42: Catalogue of all mapped monazite grains in PF-2, featuring U maps and calculated ages for compositional domains. Analysis points of the ages are identified with a blue circle.

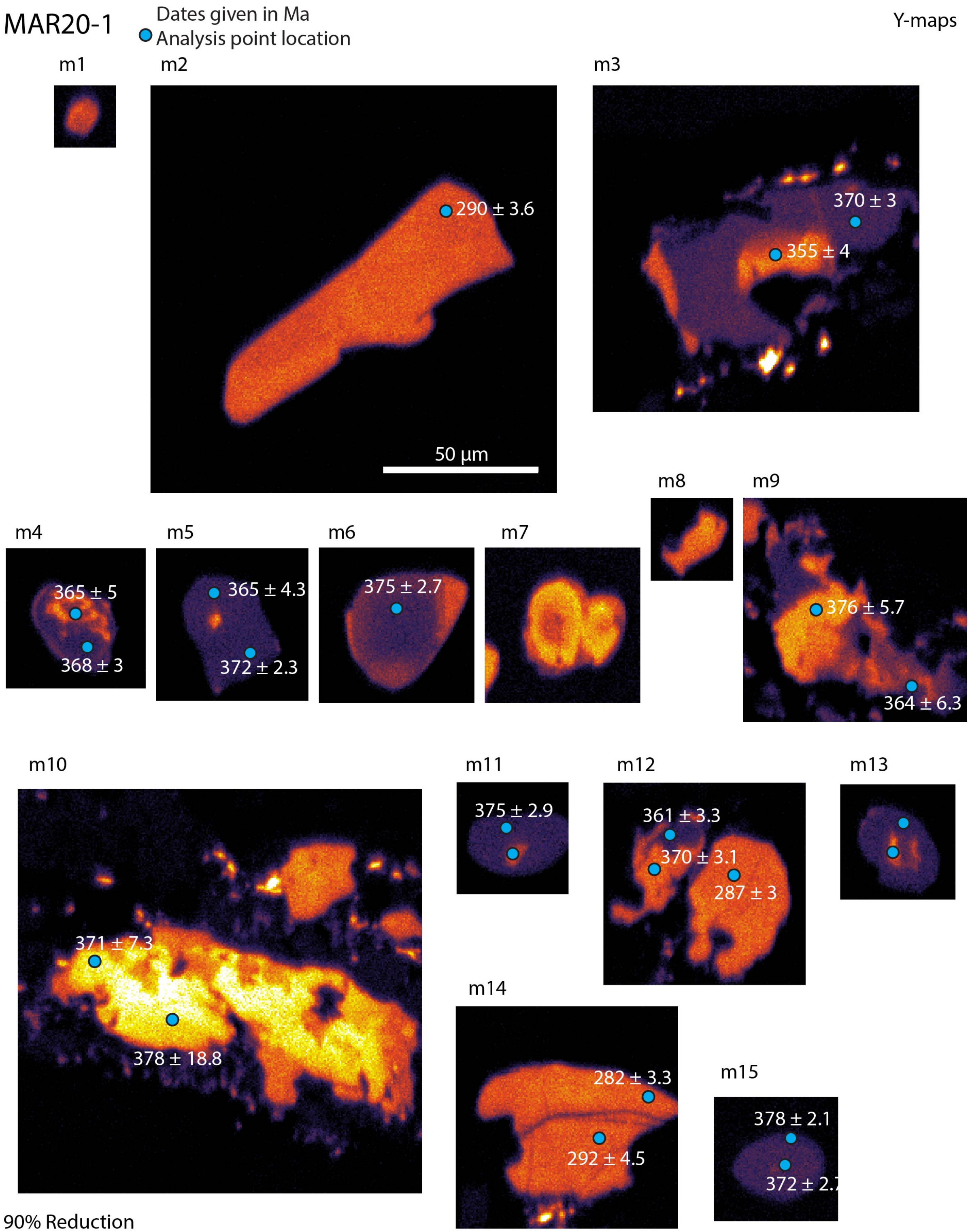

Figure 43: Catalogue of all mapped monazite grains in MAR20-1, featuring Y maps and calculated ages for compositional domains. Analysis points of the ages are identified with a blue circle.

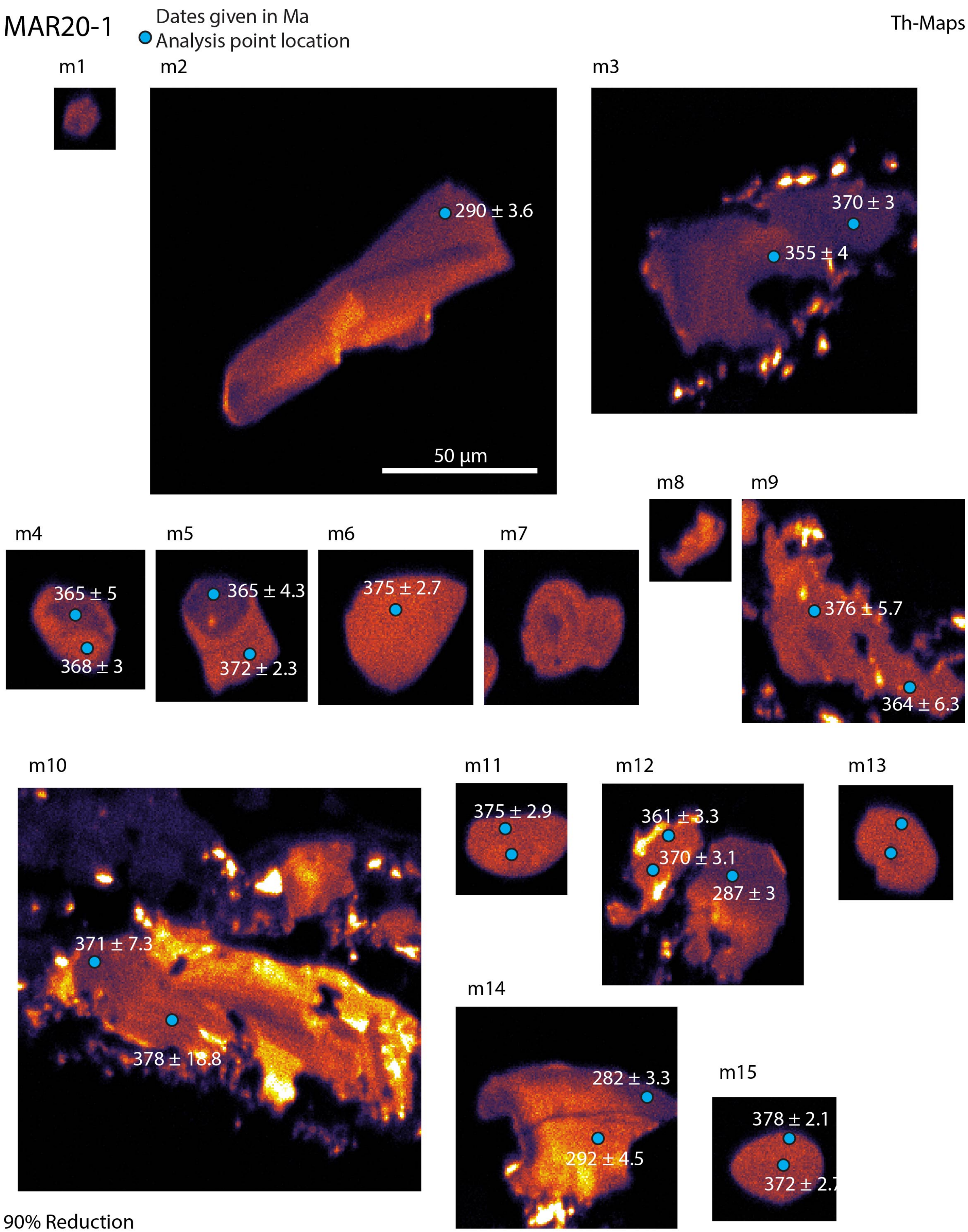

Figure 44: Catalogue of all mapped monazite grains in MAR20-1, featuring Th maps and calculated ages for compositional domains. Analysis points of the ages are identified with a blue circle.

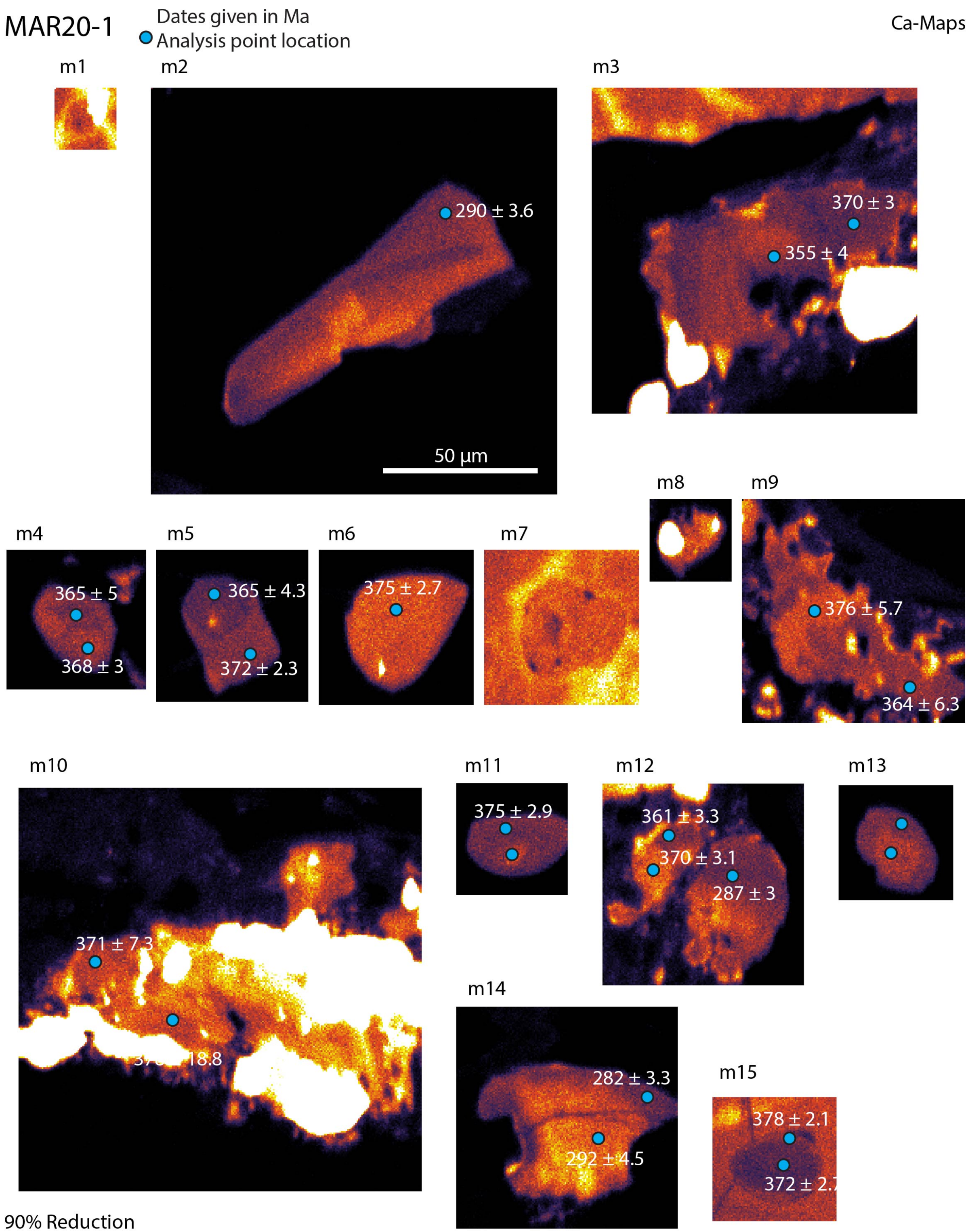

Figure 45: Catalogue of all mapped monazite grains in MAR20-1, featuring Ca maps and calculated ages for compositional domains. Analysis points of the ages are identified with a blue circle.

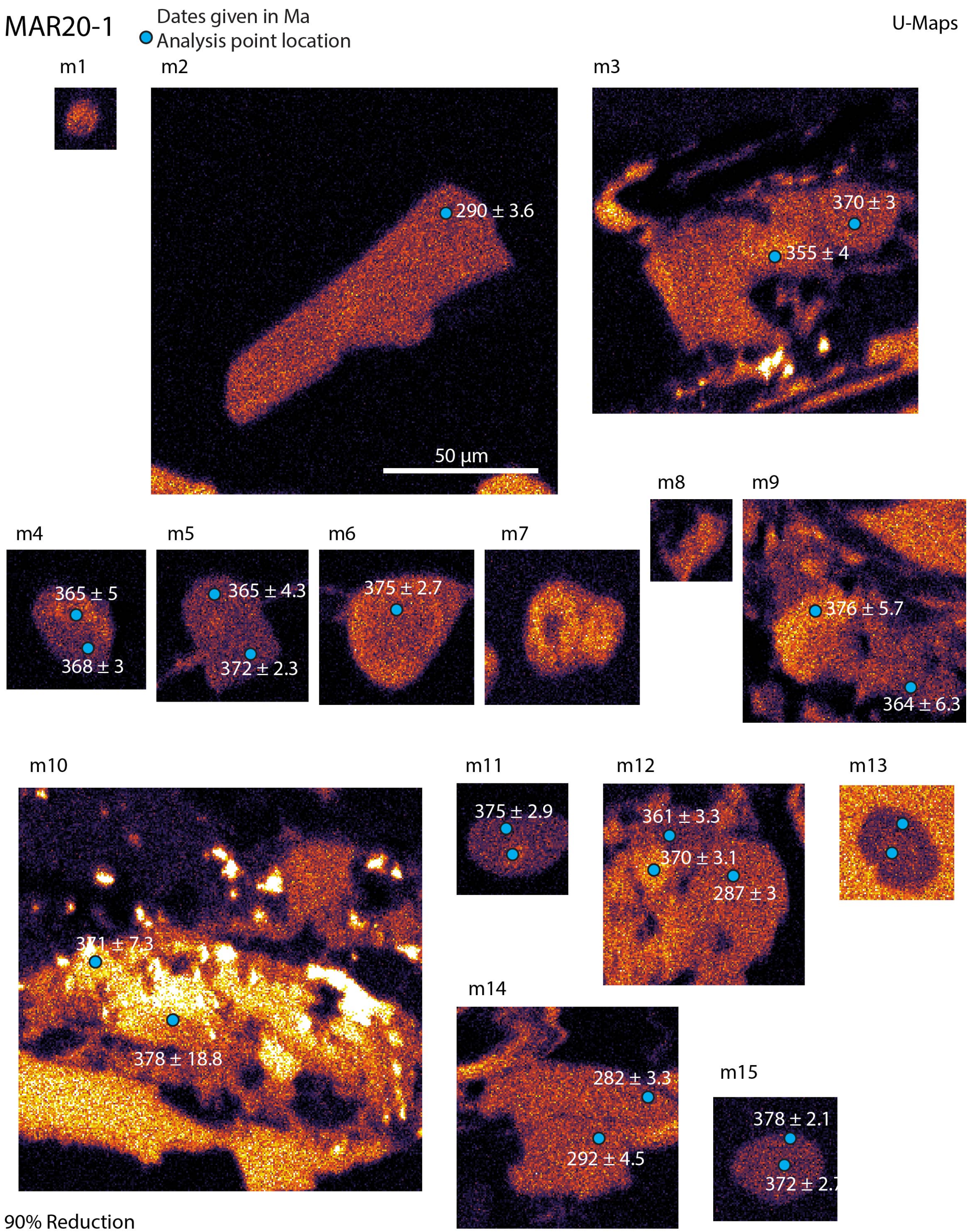

Figure 46: Catalogue of all mapped monazite grains in MAR20-1, featuring U maps and calculated ages for compositional domains. Analysis points of the ages are identified with a blue circle.

Table 2. BE17-2 monazite results, grain number, domain description, age, standard deviation, domain#.

ID Tag:		Grain:	Domain:	Ma	Sd	Dom
64	SD-BE17-2	M16	core	376	3.8	3
53	SD-BE17-2	M20	low Y-2nd grp	386	3.4	3
68	SD-BE17-2	M20	Hi Y core PbP	359	5.4	3
61	SD-BE17-2	M25	core	349	4.3	3
62	SD-BE17-2	M25	low Y low Th	391	10	3
65	SD-BE17-2	M4	Hi Y	361	3	3
56	SD-BE17-2	M11	low Y right	372	3.8	4
55	SD-BE17-2	M12	low Y	376	3.5	4
50	SD-BE17-2	M15	low Y	371	5.1	4
49	SD-BE17-2	M17	low Y	369	8.3	4
52	SD-BE17-2	M18	low Y	367	2	4
53	SD-BE17-2	M20	low Y	375	5.3	4
51	SD-BE17-2	M21	low Y	366	2.7	4
54	SD-BE17-2	M23	low Y	365	2.5	4
63	SD-BE17-2	M25	low Y higher Th	365	4.8	4
58	SD-BE17-2	M3	low Y	371	5.5	4
57	SD-BE17-2	M8	low Y	370	2.7	4
48	SD-BE17-2	M9	low Y	374	2.3	4
45	SD-BE17-2	M15	hi Y rim	374	7.2	5
46	SD-BE17-2	M17	hi Y rim	262	5.7	6
47	SD-BE17-2	M9	hi Y rim left	281	2.3	6

Table 2 Continued. BE17-2 monazite results, PPM.

ID Tag:		PPM Ca	K	Si	Sr	P	As	Th
64	SD-BE17-2	4225	93	1432	11	126316	384	38158
53	SD-BE17-2	3875	10	272	59	131722	91	20310
68	SD-BE17-2	2427	-1	208	110	130451	426	12441
61	SD-BE17-2	2484	2	241	167	129370	-60	13637
62	SD-BE17-2	6277	21	501	14	131180	1119	34632
65	SD-BE17-2	5057	28	826	-15	130390	448	33896
56	SD-BE17-2	3753	40	1903	59	125309	-48	40379
55	SD-BE17-2	3717	9	1962	-41	125690	398	41042
50	SD-BE17-2	4203	14	1726	57	126481	569	40858
49	SD-BE17-2	3143	9	1965	39	124717	505	38031
52	SD-BE17-2	3661	1	1998	70	125030	-167	41859
53	SD-BE17-2	3470	37	1661	-86	125448	384	36338
51	SD-BE17-2	3801	92	1552	49	125811	56	36840
54	SD-BE17-2	3327	-1	1850	44	125377	344	37686
63	SD-BE17-2	4025	44	1864	9	125700	902	41153
58	SD-BE17-2	3179	-2	1973	9	125405	-290	38411
57	SD-BE17-2	4270	180	1324	55	128890	159	36008
48	SD-BE17-2	3811	13	1844	-14	127088	45	40853
45	SD-BE17-2	5346	158	1131	124	128479	4	31883
46	SD-BE17-2	5622	25	229	520	130261	-141	35290
47	SD-BE17-2	5016	160	386	564	131081	5	31692

Table 2 Continued. BE17-2 monazite results, PPM.

ID	Tag:	PPM U	Y	La	Ce	Pr	Nd	Sm
64	SD-BE17-2	1483	740	133573	258518	26482	111337	16487
53	SD-BE17-2	4669	23159	125658	248566	25214	104378	15513
68	SD-BE17-2	1983	5984	114714	255884	29661	132192	24809
61	SD-BE17-2	1861	5738	114280	254173	29520	131513	24985
62	SD-BE17-2	5584	6027	128921	241551	24950	106744	20750
65	SD-BE17-2	3226	20099	125819	244600	24960	102759	15567
56	SD-BE17-2	1167	550	132647	258999	27242	113573	14884
55	SD-BE17-2	1116	354	131773	259634	27306	113602	14840
50	SD-BE17-2	1375	735	133147	259225	26889	111895	15654
49	SD-BE17-2	981	428	126161	263983	28236	118894	14176
52	SD-BE17-2	1103	303	123751	262687	28243	120508	14640
53	SD-BE17-2	1024	476	131324	263807	27531	115637	15093
51	SD-BE17-2	1172	547	125400	262177	28450	119711	15580
54	SD-BE17-2	1052	233	125190	266234	28983	120971	14432
63	SD-BE17-2	1281	384	123333	263295	28712	121324	15178
58	SD-BE17-2	986	271	129341	266029	28075	117178	14000
57	SD-BE17-2	1756	1049	139016	258292	26519	110616	17948
48	SD-BE17-2	1177	676	134156	260690	27254	114173	15665
45	SD-BE17-2	3159	13563	131134	234574	23557	97726	18333
46	SD-BE17-2	2057	13887	124240	237652	24155	101864	16603
47	SD-BE17-2	2203	8703	126910	240936	25059	106552	19129

Table 2 Continued. BE17-2 monazite results, PPM.

ID	Tag:	PPM Eu	Gd	Tb	Dy	Ho	Er	Tm
64	SD-BE17-2	1066	5903	5	374	-97	-38	-97
53	SD-BE17-2	1155	13152	1105	6875	847	1756	210
68	SD-BE17-2	5315	14611	750	3023	181	338	39
61	SD-BE17-2	5430	14766	735	2972	196	362	-55
62	SD-BE17-2	2143	17885	952	3202	230	304	-36
65	SD-BE17-2	958	12417	1089	6119	423	1550	152
56	SD-BE17-2	927	4762	-54	285	665	138	85
55	SD-BE17-2	928	4662	-128	260	448	64	167
50	SD-BE17-2	883	5038	-191	194	-591	-153	-264
49	SD-BE17-2	1011	4075	-88	208	151	-22	20
52	SD-BE17-2	985	4136	-124	210	585	113	125
53	SD-BE17-2	964	4653	-16	161	-224	-70	-64
51	SD-BE17-2	1013	4970	-153	268	7	-51	-158
54	SD-BE17-2	990	3982	-65	124	479	69	103
63	SD-BE17-2	939	4405	-111	209	321	33	113
58	SD-BE17-2	926	3949	-204	117	209	-30	-45
57	SD-BE17-2	1122	7765	118	772	283	141	112
48	SD-BE17-2	1211	5432	15	412	561	91	109
45	SD-BE17-2	5636	16448	1228	5409	302	858	104
46	SD-BE17-2	12527	13300	831	5070	-883	407	-292
47	SD-BE17-2	10687	13739	808	3693	275	183	18

Table 2 Continued. BE17-2 monazite results, PPM.

		PPM			
ID	Tag:	**Yb**	**S**	**Pb**	**Total**
64	SD-BE17-2	-103	-33	743	99.28
53	SD-BE17-2	585	-50	568	100.35
68	SD-BE17-2	-43	-23	294	100.7
61	SD-BE17-2	-24	-37	345	100.26
62	SD-BE17-2	-83	-44	885	100.5
65	SD-BE17-2	265	-50	716	100.36
56	SD-BE17-2	251	-18	734	99.4
55	SD-BE17-2	169	-40	742	99.44
50	SD-BE17-2	-441	-23	758	99.43
49	SD-BE17-2	10	-21	675	99.15
52	SD-BE17-2	222	-12	747	99.66
53	SD-BE17-2	-230	-39	665	99.31
51	SD-BE17-2	-167	-8	665	99.35
54	SD-BE17-2	125	-24	693	99.81
63	SD-BE17-2	-4	-21	756	99.98
58	SD-BE17-2	79	-11	689	99.67
57	SD-BE17-2	31	-28	693	100.78
48	SD-BE17-2	149	-25	730	100.5
45	SD-BE17-2	-23	-27	706	98.83
46	SD-BE17-2	-667	-42	526	99.34
47	SD-BE17-2	-129	-33	454	99.97

Table 2 Continued. BE17-2 monazite results, WEIGHT %.

		Weight%						
ID	Tag:	CaO	K_2O	SiO_2	SrO	P_2O_5	As_2O_5	ThO_2
64	SD-BE17-2	0.591	0.011	0.306	0.001	28.94	0	4.34
53	SD-BE17-2	0.542	0.001	0.058	0.007	30.18	0	2.31
68	SD-BE17-2	0.34	0	0.045	0.013	29.89	0	1.42
61	SD-BE17-2	0.348	0	0.052	0.02	29.64	0	1.55
62	SD-BE17-2	0.878	0.002	0.107	0.002	30.06	0	3.94
65	SD-BE17-2	0.708	0.003	0.177	-0.002	29.88	0	3.86
56	SD-BE17-2	0.525	0.005	0.407	0.007	28.71	0	4.59
55	SD-BE17-2	0.52	0.001	0.42	-0.005	28.8	0	4.67
50	SD-BE17-2	0.588	0.002	0.369	0.007	28.98	0	4.65
49	SD-BE17-2	0.44	0.001	0.42	0.005	28.58	0	4.33
52	SD-BE17-2	0.512	0	0.427	0.008	28.65	0	4.76
53	SD-BE17-2	0.486	0.004	0.355	-0.01	28.75	0	4.13
51	SD-BE17-2	0.532	0.011	0.332	0.006	28.83	0	4.19
54	SD-BE17-2	0.465	0	0.396	0.005	28.73	0	4.29
63	SD-BE17-2	0.563	0.005	0.399	0.001	28.8	0	4.68
58	SD-BE17-2	0.445	0	0.422	0.001	28.74	0	4.37
57	SD-BE17-2	0.598	0.022	0.283	0.006	29.53	0	4.1
48	SD-BE17-2	0.533	0.002	0.394	-0.002	29.12	0	4.65
45	SD-BE17-2	0.748	0.019	0.242	0.015	29.44	0	3.63
46	SD-BE17-2	0.787	0.003	0.049	0.062	29.85	0	4.02
47	SD-BE17-2	0.702	0.019	0.083	0.067	30.04	0	3.61

Table 2 Continued. BE17-2 monazite results, WEIGHT %.

	ID Tag:	Weight% UO_2	Y_2O_3	La_2O_3	Ce_2O_3	Pr_2O_3	Nd_2O_3	Sm_2O_3
64	SD-BE17-2	0.168	0.094	15.67	30.28	3.1	12.99	1.91
53	SD-BE17-2	0.53	2.94	14.74	29.11	2.95	12.17	1.8
68	SD-BE17-2	0.225	0.76	13.45	29.97	3.47	15.42	2.88
61	SD-BE17-2	0.211	0.729	13.4	29.77	3.45	15.34	2.9
62	SD-BE17-2	0.633	0.765	15.12	28.29	2.92	12.45	2.41
65	SD-BE17-2	0.366	2.55	14.76	28.65	2.92	11.99	1.81
56	SD-BE17-2	0.132	0.07	15.56	30.34	3.19	13.25	1.73
55	SD-BE17-2	0.127	0.045	15.45	30.41	3.2	13.25	1.72
50	SD-BE17-2	0.156	0.093	15.62	30.36	3.15	13.05	1.82
49	SD-BE17-2	0.111	0.054	14.8	30.92	3.3	13.87	1.64
52	SD-BE17-2	0.125	0.038	14.51	30.77	3.31	14.06	1.7
53	SD-BE17-2	0.116	0.06	15.4	30.9	3.22	13.49	1.75
51	SD-BE17-2	0.133	0.07	14.71	30.71	3.33	13.96	1.81
54	SD-BE17-2	0.119	0.03	14.68	31.18	3.39	14.11	1.67
63	SD-BE17-2	0.145	0.049	14.46	30.84	3.36	14.15	1.76
58	SD-BE17-2	0.112	0.034	15.17	31.16	3.29	13.67	1.62
57	SD-BE17-2	0.199	0.133	16.3	30.25	3.1	12.9	2.08
48	SD-BE17-2	0.134	0.086	15.73	30.53	3.19	13.32	1.82
45	SD-BE17-2	0.358	1.72	15.38	27.48	2.76	11.4	2.13
46	SD-BE17-2	0.233	1.76	14.57	27.84	2.83	11.88	1.93
47	SD-BE17-2	0.25	1.11	14.88	28.22	2.93	12.43	2.22

Table 2 Continued. BE17-2 monazite results, WEIGHT %.

ID	Tag:	Weight% Eu_2O_3	Gd_2O_3	Tb_2O_3	Dy_2O_3	Ho_2O_3	Er_2O_3	Tm_2O_3
64	SD-BE17-2	0.123	0.68	0.001	0.043	-0.011	-0.004	-0.011
53	SD-BE17-2	0.134	1.52	0.127	0.789	0.097	0.201	0.024
68	SD-BE17-2	0.615	1.68	0.086	0.347	0.021	0.039	0.004
61	SD-BE17-2	0.629	1.7	0.085	0.341	0.022	0.041	-0.006
62	SD-BE17-2	0.248	2.06	0.11	0.368	0.026	0.035	-0.004
65	SD-BE17-2	0.111	1.43	0.125	0.702	0.048	0.177	0.017
56	SD-BE17-2	0.107	0.549	-0.006	0.033	0.076	0.016	0.01
55	SD-BE17-2	0.107	0.537	-0.015	0.03	0.051	0.007	0.019
50	SD-BE17-2	0.102	0.581	-0.022	0.022	-0.068	-0.018	-0.03
49	SD-BE17-2	0.117	0.47	-0.01	0.024	0.017	-0.002	0.002
52	SD-BE17-2	0.114	0.477	-0.014	0.024	0.067	0.013	0.014
53	SD-BE17-2	0.112	0.536	-0.002	0.018	-0.026	-0.008	-0.007
51	SD-BE17-2	0.117	0.573	-0.018	0.031	0.001	-0.006	-0.018
54	SD-BE17-2	0.115	0.459	-0.007	0.014	0.055	0.008	0.012
63	SD-BE17-2	0.109	0.508	-0.013	0.024	0.037	0.004	0.013
58	SD-BE17-2	0.107	0.455	-0.023	0.013	0.024	-0.003	-0.005
57	SD-BE17-2	0.13	0.895	0.014	0.089	0.032	0.016	0.013
48	SD-BE17-2	0.14	0.626	0.002	0.047	0.064	0.01	0.012
45	SD-BE17-2	0.653	1.9	0.141	0.621	0.035	0.098	0.012
46	SD-BE17-2	1.45	1.53	0.096	0.582	-0.101	0.047	-0.033
47	SD-BE17-2	1.24	1.58	0.093	0.424	0.031	0.021	0.002

Table 2 Continued. BE17-2 monazite results, WEIGHT %.

		Weight%			
ID	Tag:	Yb_2O_3	SO_3	PbO	Total
64	SD-BE17-2	-0.012	-0.008	0.08	99.28
53	SD-BE17-2	0.067	-0.012	0.061	100.35
68	SD-BE17-2	-0.005	-0.006	0.032	100.70
61	SD-BE17-2	-0.003	-0.009	0.037	100.25
62	SD-BE17-2	-0.009	-0.011	0.095	100.50
65	SD-BE17-2	0.03	-0.012	0.077	100.38
56	SD-BE17-2	0.029	-0.004	0.079	99.41
55	SD-BE17-2	0.019	-0.01	0.08	99.43
50	SD-BE17-2	-0.05	-0.006	0.082	99.44
49	SD-BE17-2	0.001	-0.005	0.073	99.16
52	SD-BE17-2	0.025	-0.003	0.08	99.67
53	SD-BE17-2	-0.026	-0.01	0.072	99.31
51	SD-BE17-2	-0.019	-0.002	0.072	99.36
54	SD-BE17-2	0.014	-0.006	0.075	99.80
63	SD-BE17-2	0	-0.005	0.081	99.97
58	SD-BE17-2	0.009	-0.003	0.074	99.68
57	SD-BE17-2	0.004	-0.007	0.075	100.76
48	SD-BE17-2	0.017	-0.006	0.079	100.50
45	SD-BE17-2	-0.003	-0.007	0.076	98.85
46	SD-BE17-2	-0.076	-0.01	0.057	99.36
47	SD-BE17-2	-0.015	-0.008	0.049	99.98

Table 2 Continued. BE17-2 monazite results, CATIONS.

		Cations						
ID	Tag:	**Ca**	**K**	**Si**	**Sr**	**P**	**As**	**Th**
64	SD-BE17-2	0.0253	0.0006	0.0123	0	0.9803	0	0.0395
53	SD-BE17-2	0.0226	0.0001	0.0023	0.0002	0.9936	0	0.0205
68	SD-BE17-2	0.0143	0	0.0017	0.0003	0.9923	0	0.0126
61	SD-BE17-2	0.0147	0	0.002	0.0005	0.9903	0	0.0139
62	SD-BE17-2	0.0368	0.0001	0.0042	0	0.9952	0	0.0351
65	SD-BE17-2	0.0296	0.0002	0.0069	0	0.9876	0	0.0343
56	SD-BE17-2	0.0226	0.0002	0.0163	0.0002	0.9745	0	0.0419
55	SD-BE17-2	0.0223	0.0001	0.0168	-0.0001	0.976	0	0.0425
50	SD-BE17-2	0.0251	0.0001	0.0147	0.0002	0.9794	0	0.0422
49	SD-BE17-2	0.019	0.0001	0.0169	0.0001	0.9733	0	0.0396
52	SD-BE17-2	0.022	0	0.0171	0.0002	0.972	0	0.0434
53	SD-BE17-2	0.0209	0.0002	0.0143	-0.0002	0.9761	0	0.0377
51	SD-BE17-2	0.0228	0.0006	0.0133	0.0001	0.9776	0	0.0382
54	SD-BE17-2	0.02	0	0.0158	0.0001	0.9729	0	0.039
63	SD-BE17-2	0.0241	0.0003	0.0159	0	0.9732	0	0.0425
58	SD-BE17-2	0.0191	0	0.0169	0	0.9734	0	0.0398
57	SD-BE17-2	0.0252	0.0011	0.0111	0.0001	0.9833	0	0.0367
48	SD-BE17-2	0.0226	0.0001	0.0156	0	0.9764	0	0.0419
45	SD-BE17-2	0.0318	0.001	0.0096	0.0003	0.9887	0	0.0328
46	SD-BE17-2	0.0332	0.0002	0.0019	0.0014	0.9959	0	0.036
47	SD-BE17-2	0.0295	0.001	0.0032	0.0015	0.9972	0	0.0322

Table 2 Continued. BE17-2 monazite results, CATIONS.

		Cations						
ID	Tag:	**U**	**Y**	**La**	**Ce**	**Pr**	**Nd**	**Sm**
64	SD-BE17-2	0.0015	0.002	0.2312	0.4435	0.0452	0.1856	0.0264
53	SD-BE17-2	0.0046	0.0609	0.2114	0.4145	0.0418	0.1691	0.0241
68	SD-BE17-2	0.002	0.0159	0.1946	0.4303	0.0496	0.216	0.0389
61	SD-BE17-2	0.0019	0.0153	0.1951	0.4301	0.0497	0.2162	0.0394
62	SD-BE17-2	0.0055	0.0159	0.2181	0.4051	0.0416	0.1739	0.0324
65	SD-BE17-2	0.0032	0.053	0.2125	0.4096	0.0416	0.1672	0.0243
56	SD-BE17-2	0.0012	0.0015	0.23	0.4453	0.0466	0.1897	0.0238
55	SD-BE17-2	0.0011	0.001	0.2282	0.4457	0.0466	0.1895	0.0237
50	SD-BE17-2	0.0014	0.002	0.2299	0.4437	0.0458	0.1861	0.025
49	SD-BE17-2	0.001	0.0012	0.2195	0.4554	0.0484	0.1993	0.0228
52	SD-BE17-2	0.0011	0.0008	0.2145	0.4515	0.0483	0.2012	0.0234
53	SD-BE17-2	0.001	0.0013	0.2278	0.4538	0.0471	0.1932	0.0242
51	SD-BE17-2	0.0012	0.0015	0.2173	0.4504	0.0486	0.1998	0.0249
54	SD-BE17-2	0.0011	0.0006	0.2166	0.4567	0.0494	0.2016	0.0231
63	SD-BE17-2	0.0013	0.001	0.2129	0.4507	0.0489	0.2018	0.0242
58	SD-BE17-2	0.001	0.0007	0.2239	0.4565	0.0479	0.1953	0.0224
57	SD-BE17-2	0.0017	0.0028	0.2365	0.4356	0.0445	0.1813	0.0282
48	SD-BE17-2	0.0012	0.0018	0.2298	0.4428	0.046	0.1884	0.0248
45	SD-BE17-2	0.0032	0.0364	0.225	0.3991	0.0399	0.1615	0.0291
46	SD-BE17-2	0.002	0.037	0.2118	0.4017	0.0406	0.1673	0.0261
47	SD-BE17-2	0.0022	0.0231	0.2153	0.4052	0.0419	0.1741	0.03

Table 2 Continued. BE17-2 monazite results, CATIONS.

		Cations					
ID	Tag:	**Eu**	**Gd**	**Tb**	**Dy**	**Ho**	**Er**
64	SD-BE17-2	0.0017	0.009	0	0.0006	-0.0001	-0.0001
53	SD-BE17-2	0.0018	0.0195	0.0016	0.0099	0.0012	0.0025
68	SD-BE17-2	0.0082	0.0219	0.0011	0.0044	0.0003	0.0005
61	SD-BE17-2	0.0085	0.0223	0.0011	0.0043	0.0003	0.0005
62	SD-BE17-2	0.0033	0.0267	0.0014	0.0046	0.0003	0.0004
65	SD-BE17-2	0.0015	0.0185	0.0016	0.0088	0.0006	0.0022
56	SD-BE17-2	0.0015	0.0073	-0.0001	0.0004	0.001	0.0002
55	SD-BE17-2	0.0015	0.0071	-0.0002	0.0004	0.0007	0.0001
50	SD-BE17-2	0.0014	0.0077	-0.0003	0.0003	-0.0009	-0.0002
49	SD-BE17-2	0.0016	0.0063	-0.0001	0.0003	0.0002	0
52	SD-BE17-2	0.0016	0.0063	-0.0002	0.0003	0.0009	0.0002
53	SD-BE17-2	0.0015	0.0071	0	0.0002	-0.0003	-0.0001
51	SD-BE17-2	0.0016	0.0076	-0.0002	0.0004	0	-0.0001
54	SD-BE17-2	0.0016	0.0061	-0.0001	0.0002	0.0007	0.0001
63	SD-BE17-2	0.0015	0.0067	-0.0002	0.0003	0.0005	0
58	SD-BE17-2	0.0015	0.006	-0.0003	0.0002	0.0003	0
57	SD-BE17-2	0.0017	0.0117	0.0002	0.0011	0.0004	0.0002
48	SD-BE17-2	0.0019	0.0082	0	0.0006	0.0008	0.0001
45	SD-BE17-2	0.0088	0.0249	0.0018	0.0079	0.0004	0.0012
46	SD-BE17-2	0.0195	0.02	0.0012	0.0074	-0.0013	0.0006
47	SD-BE17-2	0.0166	0.0206	0.0012	0.0054	0.0004	0.0003

Table 2 Continued. BE17-2 monazite results, CATIONS.

		Cations				
ID	Tag:	**Tm**	**Yb**	**S**	**Pb**	**CatSum**
64	SD-BE17-2	-0.0001	-0.0001	-0.0002	0.0009	1.0244
53	SD-BE17-2	0.0003	0.0008	-0.0004	0.0006	1.0097
68	SD-BE17-2	0.0001	-0.0001	-0.0002	0.0003	1.0126
61	SD-BE17-2	-0.0001	0	-0.0003	0.0004	1.0157
62	SD-BE17-2	-0.0001	-0.0001	-0.0003	0.001	1.0062
65	SD-BE17-2	0.0002	0.0004	-0.0004	0.0008	1.0164
56	SD-BE17-2	0.0001	0.0003	-0.0001	0.0009	1.0308
55	SD-BE17-2	0.0002	0.0002	-0.0003	0.0009	1.0279
50	SD-BE17-2	-0.0004	-0.0006	-0.0002	0.0009	1.0239
49	SD-BE17-2	0	0	-0.0002	0.0008	1.0322
52	SD-BE17-2	0.0002	0.0003	-0.0001	0.0009	1.0339
53	SD-BE17-2	-0.0001	-0.0003	-0.0003	0.0008	1.0298
51	SD-BE17-2	-0.0002	-0.0002	-0.0001	0.0008	1.0282
54	SD-BE17-2	0.0001	0.0002	-0.0002	0.0008	1.0336
63	SD-BE17-2	0.0002	0	-0.0002	0.0009	1.0333
58	SD-BE17-2	-0.0001	0.0001	-0.0001	0.0008	1.0319
57	SD-BE17-2	0.0002	0	-0.0002	0.0008	1.0209
48	SD-BE17-2	0.0002	0.0002	-0.0002	0.0008	1.0277
45	SD-BE17-2	0.0001	0	-0.0002	0.0008	1.0154
46	SD-BE17-2	-0.0004	-0.0009	-0.0003	0.0006	1.0057
47	SD-BE17-2	0	-0.0002	-0.0002	0.0005	1.0036

Table 3. PF2-A monazite results: grain number, domain description, age, standard deviation, domain#.

ID	Tag:	Grain:	Domain:	Ma	Sd	Dom
21	SD-PF2A	M1	hi-Y-core	382	2.3	2
38	SD-PF2A	M10	hi Y core	384	2.9	2
41	SD-PF2A	M11	hi Y core	363	6.5	4
4	SD-PF2A	M3	core	374	1.8	4
5	SD-PF2A	M5	lower-core	374	5.5	4
22	SD-PF2A	M1	low Y upper	367	3.7	4
23	SD-PF2A	M9	core upper	371	1.5	4
24	SD-PF2A	M10	low Y upper	382	1.6	4
25	SD-PF2A	M11	low Y right	370	2	4
26	SD-PF2A	M12	low Y right	376	2.4	4
27	SD-PF2A	M15	core center	380	3.2	4
34	SD-PF2A	M4	low Y	365	3.8	4
35	SD-PF2A	M19	low Y	367	2.7	4
3	SD-PF2A	M2	hi-Y-core	357	2.2	5
28	SD-PF2A	M15	high Y upper	372	1	5
31	SD-PF2A	M11	hi Y rim right	378	8.3	5
32	SD-PF2A	M19	hi Y strip	378	4.4	5
33	SD-PF2A	M4	hi Y left	358	3.5	5
37	SD-PF2A	M16	hi Y rim lower	383	5.4	5
40	SD-PF2A	M1	hi Y rim	372	4.7	5
30	SD-PF2A	M15	high Y outer rim	371	3.6	5
36	SD-PF2A	M16	low Y	354	2.7	5

Table 3, Continued. PF2-A monazite result: PPM

ID Tag:	PPM Ca	K	Si	Sr	P	As	Th
21 SD-PF2A	7116	-11	264	147	134483	324	38941
38 SD-PF2A	5408	8	238	182	133405	783	24804
41 SD-PF2A	6055	7	242	56	132412	-431	33265
4 SD-PF2A	4926	48	939	108	131067	500	36713
5 SD-PF2A	3294	18	1818	36	130271	3	36043
22 SD-PF2A	5189	15	964	54	131693	26	38078
23 SD-PF2A	6455	34	830	119	132815	183	41897
24 SD-PF2A	4000	73	1141	97	131724	395	33313
25 SD-PF2A	4040	22	1509	88	131152	756	38488
26 SD-PF2A	2884	10	1781	66	130590	178	33959
27 SD-PF2A	4607	-8	350	30	134187	-14	25252
34 SD-PF2A	6101	-4	477	83	132059	596	38141
35 SD-PF2A	4882	2	1057	130	131673	383	38132
3 SD-PF2A	5774	86	266	110	134586	-279	33530
28 SD-PF2A	6800	7	578	92	132806	78	36314
31 SD-PF2A	6316	55	538	106	134352	59	36069
32 SD-PF2A	5997	4	313	65	133795	892	33372
33 SD-PF2A	5531	5	488	147	134782	-217	32388
37 SD-PF2A	6612	26	479	79	132807	420	34891
40 SD-PF2A	6244	29	635	79	131108	584	34197
30 SD-PF2A	6018	4	750	57	135659	789	30943
36 SD-PF2A	5183	0	837	86	132477	-242	37265

Table 3, Continued. PF2-A monazite result: PPM

ID Tag:	PPM U	Y	La	Ce	Pr	Nd	Sm
21 SD-PF2A	6113	17987	125166	238761	24314	101250	16352
38 SD-PF2A	9414	15019	119318	241198	26447	121205	22147
41 SD-PF2A	5927	16087	125115	240995	24757	104810	17342
4 SD-PF2A	1542	1044	131530	259387	27069	113866	17723
5 SD-PF2A	900	500	132469	266085	27851	116940	15103
22 SD-PF2A	1591	1361	129812	256418	26938	114101	17974
23 SD-PF2A	4366	3940	126040	244927	25440	109023	21204
24 SD-PF2A	1207	878	129830	263804	27872	118450	17469
25 SD-PF2A	1189	794	133608	264109	27425	115526	16838
26 SD-PF2A	815	389	133916	269279	28349	119556	15087
27 SD-PF2A	3895	4815	120509	254546	28065	126472	22712
34 SD-PF2A	2618	2984	130636	255222	26235	111625	17903
35 SD-PF2A	1449	1011	129439	259288	27202	115878	17825
3 SD-PF2A	2086	22543	130254	239636	23917	96353	14460
28 SD-PF2A	8486	9082	122986	243670	25423	108804	19216
31 SD-PF2A	4666	14617	123625	239998	24770	105379	18600
32 SD-PF2A	4794	13536	126616	246733	25204	107887	17016
33 SD-PF2A	2624	19109	125029	236516	24031	101186	17469
37 SD-PF2A	7182	13741	122924	242250	25219	107825	18149
40 SD-PF2A	5551	13788	122980	239044	24892	105432	17580
30 SD-PF2A	6979	17645	122508	240478	24946	104888	18329
36 SD-PF2A	1657	1778	130432	258492	27314	115718	18136

Table 3, Continued. PF2-A monazite result: PPM

ID Tag:	PPM Eu	Gd	Tb	Dy	Ho	Er	Tm
21 SD-PF2A	1950	14334	1226	6407	813	1254	206
38 SD-PF2A	3071	15128	1088	5579	707	1149	203
41 SD-PF2A	1892	14274	1170	5837	592	1140	146
4 SD-PF2A	1195	9170	107	554	158	-6	-39
5 SD-PF2A	1011	5127	-23	351	337	113	15
22 SD-PF2A	1164	9758	206	836	-5	1	-29
23 SD-PF2A	1531	14189	524	2054	316	231	116
24 SD-PF2A	1285	8363	126	641	450	78	165
25 SD-PF2A	1096	6246	54	462	527	75	50
26 SD-PF2A	1013	4743	-83	205	312	-27	-22
27 SD-PF2A	1171	14588	706	2360	468	216	50
34 SD-PF2A	1006	11059	385	1593	590	131	118
35 SD-PF2A	1164	9225	171	666	158	25	-40
3 SD-PF2A	5863	14780	1428	8069	708	1398	187
28 SD-PF2A	2007	15621	1050	4257	452	458	90
31 SD-PF2A	3086	15073	1077	5195	-46	616	-76
32 SD-PF2A	2800	12605	888	4536	581	841	172
33 SD-PF2A	7319	18098	1659	7420	852	1398	254
37 SD-PF2A	2454	13661	1026	4983	556	812	140
40 SD-PF2A	2525	14881	1142	5512	514	699	157
30 SD-PF2A	3166	16433	1288	6323	728	995	135
36 SD-PF2A	1190	10259	355	1138	231	89	-68

Table 3, Continued. PF2-A monazite result: PPM

ID Tag:	PPM Yb	S	Pb
21 SD-PF2A	420	-33	1004
38 SD-PF2A	315	-48	951
41 SD-PF2A	286	-63	850
4 SD-PF2A	27	-9	698
5 SD-PF2A	44	-28	652
22 SD-PF2A	-106	-11	710
23 SD-PF2A	10	-32	931
24 SD-PF2A	196	-44	636
25 SD-PF2A	145	-11	702
26 SD-PF2A	-76	-20	617
27 SD-PF2A	34	-15	645
34 SD-PF2A	130	-21	764
35 SD-PF2A	-188	-17	704
3 SD-PF2A	165	-28	645
28 SD-PF2A	-55	-32	1062
31 SD-PF2A	-270	-53	866
32 SD-PF2A	175	-38	827
33 SD-PF2A	342	-44	655
37 SD-PF2A	125	-41	992
40 SD-PF2A	-33	-32	869
30 SD-PF2A	146	-49	888
36 SD-PF2A	-69	-40	675

Table 3, Continued. PF2-A monazite result: WEIGHT %

ID Tag:	Weight% CaO	K_2O	SiO_2	SrO	P_2O_5	As_2O_5	ThO_2
21 SD-PF2A	0.996	-0.001	0.056	0.017	30.82	0	4.43
38 SD-PF2A	0.757	0.001	0.051	0.022	30.57	0	2.82
41 SD-PF2A	0.847	0.001	0.052	0.007	30.34	0	3.79
4 SD-PF2A	0.689	0.006	0.201	0.013	30.03	0	4.18
5 SD-PF2A	0.461	0.002	0.389	0.004	29.85	0	4.1
22 SD-PF2A	0.726	0.002	0.206	0.006	30.18	0	4.33
23 SD-PF2A	0.903	0.004	0.178	0.014	30.43	0	4.77
24 SD-PF2A	0.56	0.009	0.244	0.011	30.18	0	3.79
25 SD-PF2A	0.565	0.003	0.323	0.01	30.05	0	4.38
26 SD-PF2A	0.403	0.001	0.381	0.008	29.92	0	3.86
27 SD-PF2A	0.645	-0.001	0.075	0.004	30.75	0	2.87
34 SD-PF2A	0.854	0	0.102	0.01	30.26	0	4.34
35 SD-PF2A	0.683	0	0.226	0.015	30.17	0	4.34
3 SD-PF2A	0.808	0.01	0.057	0.013	30.84	0	3.82
28 SD-PF2A	0.951	0.001	0.124	0.011	30.43	0	4.13
31 SD-PF2A	0.884	0.007	0.115	0.013	30.79	0	4.1
32 SD-PF2A	0.839	0.001	0.067	0.008	30.66	0	3.8
33 SD-PF2A	0.774	0.001	0.104	0.017	30.88	0	3.69
37 SD-PF2A	0.925	0.003	0.102	0.009	30.43	0	3.97
40 SD-PF2A	0.874	0.003	0.136	0.009	30.04	0	3.89
30 SD-PF2A	0.842	0	0.16	0.007	31.09	0	3.52
36 SD-PF2A	0.725	0	0.179	0.01	30.36	0	4.24

Table 3, Continued. PF2-A monazite result: WEIGHT %

ID Tag:	Weight% UO_2	Y_2O_3	La_2O_3	Ce_2O_3	Pr_2O_3	Nd_2O_3	Sm_2O_3
21 SD-PF2A	0.693	2.28	14.68	27.97	2.85	11.81	1.9
38 SD-PF2A	1.07	1.91	13.99	28.25	3.1	14.14	2.57
41 SD-PF2A	0.672	2.04	14.67	28.23	2.9	12.22	2.01
4 SD-PF2A	0.175	0.133	15.43	30.38	3.17	13.28	2.06
5 SD-PF2A	0.102	0.064	15.54	31.17	3.26	13.64	1.75
22 SD-PF2A	0.18	0.173	15.22	30.03	3.15	13.31	2.08
23 SD-PF2A	0.495	0.5	14.78	28.69	2.98	12.72	2.46
24 SD-PF2A	0.137	0.111	15.23	30.9	3.26	13.82	2.03
25 SD-PF2A	0.135	0.101	15.67	30.93	3.21	13.47	1.95
26 SD-PF2A	0.092	0.049	15.71	31.54	3.32	13.94	1.75
27 SD-PF2A	0.442	0.611	14.13	29.81	3.28	14.75	2.63
34 SD-PF2A	0.297	0.379	15.32	29.89	3.07	13.02	2.08
35 SD-PF2A	0.164	0.128	15.18	30.37	3.18	13.52	2.07
3 SD-PF2A	0.237	2.86	15.28	28.07	2.8	11.24	1.68
28 SD-PF2A	0.963	1.15	14.42	28.54	2.98	12.69	2.23
31 SD-PF2A	0.529	1.86	14.5	28.11	2.9	12.29	2.16
32 SD-PF2A	0.544	1.72	14.85	28.9	2.95	12.58	1.97
33 SD-PF2A	0.298	2.43	14.66	27.7	2.81	11.8	2.03
37 SD-PF2A	0.815	1.75	14.42	28.37	2.95	12.58	2.1
40 SD-PF2A	0.63	1.75	14.42	28	2.91	12.3	2.04
30 SD-PF2A	0.792	2.24	14.37	28.17	2.92	12.23	2.13
36 SD-PF2A	0.188	0.226	15.3	30.28	3.2	13.5	2.1

Table 3, Continued. PF2-A monazite result: WEIGHT %

	Weight%					
ID Tag:	Eu_2O_3	Gd_2O_3	Tb_2O_3	Dy_2O_3	Ho_2O_3	Er_2O_3
21 SD-PF2A	0.226	1.65	0.141	0.735	0.093	0.143
38 SD-PF2A	0.356	1.74	0.125	0.64	0.081	0.131
41 SD-PF2A	0.219	1.65	0.135	0.67	0.068	0.13
4 SD-PF2A	0.138	1.06	0.012	0.064	0.018	-0.001
5 SD-PF2A	0.117	0.591	-0.003	0.04	0.039	0.013
22 SD-PF2A	0.135	1.12	0.024	0.096	-0.001	0
23 SD-PF2A	0.177	1.64	0.06	0.236	0.036	0.026
24 SD-PF2A	0.149	0.964	0.015	0.074	0.052	0.009
25 SD-PF2A	0.127	0.72	0.006	0.053	0.06	0.009
26 SD-PF2A	0.117	0.547	-0.01	0.024	0.036	-0.003
27 SD-PF2A	0.136	1.68	0.081	0.271	0.054	0.025
34 SD-PF2A	0.116	1.27	0.044	0.183	0.068	0.015
35 SD-PF2A	0.135	1.06	0.02	0.076	0.018	0.003
3 SD-PF2A	0.679	1.7	0.164	0.926	0.081	0.16
28 SD-PF2A	0.232	1.8	0.121	0.489	0.052	0.052
31 SD-PF2A	0.357	1.74	0.124	0.596	-0.005	0.07
32 SD-PF2A	0.324	1.45	0.102	0.521	0.067	0.096
33 SD-PF2A	0.847	2.09	0.191	0.852	0.098	0.16
37 SD-PF2A	0.284	1.57	0.118	0.572	0.064	0.093
40 SD-PF2A	0.292	1.72	0.131	0.633	0.059	0.08
30 SD-PF2A	0.367	1.89	0.148	0.726	0.083	0.114
36 SD-PF2A	0.138	1.18	0.041	0.131	0.027	0.01

Table 3, Continued. PF2-A monazite result: WEIGHT %

ID Tag:	Weight% Tm_2O_3	Yb_2O_3	SO_3	PbO	Total
21 SD-PF2A	0.024	0.048	-0.008	0.108	101.66
38 SD-PF2A	0.023	0.036	-0.012	0.102	102.47
41 SD-PF2A	0.017	0.033	-0.016	0.092	100.78
4 SD-PF2A	-0.004	0.003	-0.002	0.075	101.11
5 SD-PF2A	0.002	0.005	-0.007	0.07	101.20
22 SD-PF2A	-0.003	-0.012	-0.003	0.076	101.03
23 SD-PF2A	0.013	0.001	-0.008	0.1	101.21
24 SD-PF2A	0.019	0.022	-0.011	0.069	101.64
25 SD-PF2A	0.006	0.016	-0.003	0.076	101.87
26 SD-PF2A	-0.002	-0.009	-0.005	0.066	101.74
27 SD-PF2A	0.006	0.004	-0.004	0.07	102.32
34 SD-PF2A	0.014	0.015	-0.005	0.082	101.42
35 SD-PF2A	-0.005	-0.021	-0.004	0.076	101.40
3 SD-PF2A	0.021	0.019	-0.007	0.069	101.53
28 SD-PF2A	0.01	-0.006	-0.008	0.114	101.48
31 SD-PF2A	-0.009	-0.031	-0.013	0.093	101.18
32 SD-PF2A	0.02	0.02	-0.01	0.089	101.57
33 SD-PF2A	0.029	0.039	-0.011	0.071	101.56
37 SD-PF2A	0.016	0.014	-0.01	0.107	101.25
40 SD-PF2A	0.018	-0.004	-0.008	0.094	100.02
30 SD-PF2A	0.015	0.017	-0.012	0.096	101.92
36 SD-PF2A	-0.008	-0.008	-0.01	0.073	101.88

Table 3, Continued. PF2-A monazite result: CATIONS

ID Tag:		Cations Ca	K	Si	Sr	P	As	Th
21	SD-PF2A	0.0409	-0.0001	0.0022	0.0004	0.9994	0	0.0386
38	SD-PF2A	0.0311	0.0001	0.002	0.0005	0.9924	0	0.0246
41	SD-PF2A	0.0352	0	0.002	0.0001	0.9965	0	0.0334
4	SD-PF2A	0.0288	0.0003	0.0078	0.0003	0.9914	0	0.0371
5	SD-PF2A	0.0193	0.0001	0.0152	0.0001	0.9859	0	0.0364
22	SD-PF2A	0.0303	0.0001	0.008	0.0001	0.9941	0	0.0384
23	SD-PF2A	0.0375	0.0002	0.0069	0.0003	0.9979	0	0.042
24	SD-PF2A	0.0233	0.0004	0.0095	0.0003	0.9912	0	0.0335
25	SD-PF2A	0.0235	0.0001	0.0125	0.0002	0.9866	0	0.0387
26	SD-PF2A	0.0168	0.0001	0.0148	0.0002	0.9845	0	0.0342
27	SD-PF2A	0.0265	0	0.0029	0.0001	0.9984	0	0.0251
34	SD-PF2A	0.0355	0	0.004	0.0002	0.9942	0	0.0383
35	SD-PF2A	0.0284	0	0.0088	0.0003	0.9921	0	0.0384
3	SD-PF2A	0.0331	0.0005	0.0022	0.0003	0.999	0	0.0332
28	SD-PF2A	0.0394	0	0.0048	0.0002	0.9955	0	0.0363
31	SD-PF2A	0.0364	0.0003	0.0044	0.0003	1.0016	0	0.0359
32	SD-PF2A	0.0346	0	0.0026	0.0002	0.9981	0	0.0332
33	SD-PF2A	0.0317	0	0.004	0.0004	1.0006	0	0.0321
37	SD-PF2A	0.0383	0.0002	0.004	0.0002	0.9954	0	0.0349
40	SD-PF2A	0.0366	0.0002	0.0053	0.0002	0.9945	0	0.0346
30	SD-PF2A	0.0343	0	0.0061	0.0001	1.0017	0	0.0305
36	SD-PF2A	0.03	0	0.0069	0.0002	0.9933	0	0.0373

Table 3, Continued. PF2-A monazite result: CATIONS

ID Tag:	Cations U	Y	La	Ce	Pr	Nd	Sm
21 SD-PF2A	0.0059	0.0466	0.2074	0.3922	0.0397	0.1616	0.025
38 SD-PF2A	0.0091	0.0389	0.1979	0.3967	0.0432	0.1937	0.0339
41 SD-PF2A	0.0058	0.0422	0.21	0.401	0.041	0.1694	0.0269
4 SD-PF2A	0.0015	0.0028	0.2218	0.4337	0.045	0.185	0.0276
5 SD-PF2A	0.0009	0.0013	0.2236	0.4452	0.0463	0.1901	0.0235
22 SD-PF2A	0.0016	0.0036	0.2185	0.4279	0.0447	0.185	0.0279
23 SD-PF2A	0.0043	0.0103	0.2112	0.4068	0.042	0.1759	0.0328
24 SD-PF2A	0.0012	0.0023	0.2178	0.4388	0.0461	0.1914	0.0271
25 SD-PF2A	0.0012	0.0021	0.2241	0.4392	0.0454	0.1867	0.0261
26 SD-PF2A	0.0008	0.001	0.2251	0.4488	0.047	0.1936	0.0234
27 SD-PF2A	0.0038	0.0125	0.1999	0.4187	0.0459	0.2021	0.0348
34 SD-PF2A	0.0026	0.0078	0.2193	0.4248	0.0434	0.1805	0.0278
35 SD-PF2A	0.0014	0.0027	0.2175	0.4319	0.0451	0.1875	0.0277
3 SD-PF2A	0.002	0.0583	0.2156	0.3932	0.039	0.1536	0.0221
28 SD-PF2A	0.0083	0.0237	0.2056	0.4038	0.0419	0.1752	0.0297
31 SD-PF2A	0.0045	0.038	0.2055	0.3956	0.0406	0.1687	0.0286
32 SD-PF2A	0.0047	0.0352	0.2106	0.4069	0.0413	0.1729	0.0261
33 SD-PF2A	0.0025	0.0494	0.207	0.3882	0.0392	0.1613	0.0267
37 SD-PF2A	0.007	0.0359	0.2054	0.4014	0.0416	0.1736	0.028
40 SD-PF2A	0.0055	0.0364	0.208	0.4009	0.0415	0.1718	0.0275
30 SD-PF2A	0.0067	0.0454	0.2017	0.3925	0.0405	0.1663	0.0279
36 SD-PF2A	0.0016	0.0046	0.2181	0.4285	0.045	0.1864	0.028

Table 3, Continued. PF2-A monazite result: CATIONS

ID Tag:		Cations Eu	Gd	Tb	Dy	Ho	Er
21	SD-PF2A	0.003	0.021	0.0018	0.0091	0.0011	0.0017
38	SD-PF2A	0.0047	0.0222	0.0016	0.0079	0.001	0.0016
41	SD-PF2A	0.0029	0.0212	0.0017	0.0084	0.0008	0.0016
4	SD-PF2A	0.0018	0.0137	0.0002	0.0008	0.0002	0
5	SD-PF2A	0.0016	0.0076	0	0.0005	0.0005	0.0002
22	SD-PF2A	0.0018	0.0145	0.0003	0.0012	0	0
23	SD-PF2A	0.0023	0.021	0.0008	0.0029	0.0004	0.0003
24	SD-PF2A	0.002	0.0124	0.0002	0.0009	0.0006	0.0001
25	SD-PF2A	0.0017	0.0093	0.0001	0.0007	0.0007	0.0001
26	SD-PF2A	0.0016	0.007	-0.0001	0.0003	0.0004	0
27	SD-PF2A	0.0018	0.0214	0.001	0.0033	0.0007	0.0003
34	SD-PF2A	0.0015	0.0164	0.0006	0.0023	0.0008	0.0002
35	SD-PF2A	0.0018	0.0137	0.0003	0.001	0.0002	0
3	SD-PF2A	0.0089	0.0216	0.0021	0.0114	0.001	0.0019
28	SD-PF2A	0.0031	0.0231	0.0015	0.0061	0.0006	0.0006
31	SD-PF2A	0.0047	0.0221	0.0016	0.0074	-0.0001	0.0009
32	SD-PF2A	0.0043	0.0185	0.0013	0.0064	0.0008	0.0012
33	SD-PF2A	0.0111	0.0265	0.0024	0.0105	0.0012	0.0019
37	SD-PF2A	0.0037	0.0202	0.0015	0.0071	0.0008	0.0011
40	SD-PF2A	0.0039	0.0222	0.0017	0.008	0.0007	0.001
30	SD-PF2A	0.0048	0.0239	0.0019	0.0089	0.001	0.0014
36	SD-PF2A	0.0018	0.0151	0.0005	0.0016	0.0003	0.0001

Table 3, Continued. PF2-A monazite result: CATIONS

ID Tag:	Cations Tm	Yb	S	Pb	CatSum
21 SD-PF2A	0.0003	0.0006	-0.0002	0.0011	0.9998
38 SD-PF2A	0.0003	0.0004	-0.0003	0.0011	1.012
41 SD-PF2A	0.0002	0.0004	-0.0005	0.001	1.0046
4 SD-PF2A	-0.0001	0	-0.0001	0.0008	1.0091
5 SD-PF2A	0	0.0001	-0.0002	0.0007	1.0129
22 SD-PF2A	0	-0.0001	-0.0001	0.0008	1.0044
23 SD-PF2A	0.0002	0	-0.0002	0.001	0.9991
24 SD-PF2A	0.0002	0.0003	-0.0003	0.0007	1.0087
25 SD-PF2A	0.0001	0.0002	-0.0001	0.0008	1.0132
26 SD-PF2A	0	-0.0001	-0.0001	0.0007	1.0153
27 SD-PF2A	0.0001	0	-0.0001	0.0007	1.0013
34 SD-PF2A	0.0002	0.0002	-0.0002	0.0009	1.007
35 SD-PF2A	-0.0001	-0.0003	-0.0001	0.0008	1.0069
3 SD-PF2A	0.0003	0.0002	-0.0002	0.0007	1.0011
28 SD-PF2A	0.0001	-0.0001	-0.0002	0.0012	1.0049
31 SD-PF2A	-0.0001	-0.0004	-0.0004	0.001	0.9954
32 SD-PF2A	0.0002	0.0002	-0.0003	0.0009	1.0019
33 SD-PF2A	0.0003	0.0005	-0.0003	0.0007	0.9974
37 SD-PF2A	0.0002	0.0002	-0.0003	0.0011	1.006
40 SD-PF2A	0.0002	0	-0.0002	0.001	1.0069
30 SD-PF2A	0.0002	0.0002	-0.0003	0.001	0.995
36 SD-PF2A	-0.0001	-0.0001	-0.0003	0.0008	1.0065

Table 4. MAR20-1 monazite results, grain number, domain, age, standard dev., CR, domain#.

ID Tag:	Grain number:	Domain:	Ma	Sd	CR	Dom
7 SD-MAR20-1	M3	hi Y	355	4	0	2
8 SD-MAR20-1	M4	low Y core	365	5	0	2
19 SD-MAR20-1	M4	rim	368	3	0	3
20 SD-MAR20-1	M5	top	365	4.3	0	3
28 SD-MAR20-1	M5	bot	372	2.4	0	3
29 SD-MAR20-1	M6	core	375	2.7	0	3
9 SD-MAR20-1	M9	hi Y	376	5.7	0	3
10 SD-MAR20-1	M10	hi y core	378	18.8	0	3
11 SD-MAR20-1	M13	core	368	11.6	0	3
17 SD-MAR20-1	M15	core	372	2.7	0	3
18 SD-MAR20-1	M3	right	370	3	0	4
15 SD-MAR20-1	M9	right	364	6.3	0	4
16 SD-MAR20-1	M10	left	363	2.8	0	4
12 SD-MAR20-1	M10	low y up	371	7.3	0	4
3 SD-MAR20-1	M11	top	375	2.9	0	4
5 SD-MAR20-1	M12	hi Y left	370	3.1	1	4
14 SD-MAR20-1	M12	low Y left	361	3.3	2	4
4 SD-MAR20-1	M13	low Y rim	379	9.5	0	4
6 SD-MAR20-1	M15	hi Y rim	378	2.1	0	4
24 SD-MAR20-1	M2	up-right	290	3.6	0	5
7 SD-MAR20-1	M2	bo-edge	300	9.3	0	5
8 SD-MAR20-1	M12	up right	287	3	3	5
9 SD-MAR20-1	M14	lower	292	4.5	0	5
13 SD-MAR20-1	M14	up right rim	282	3.3	0	5

Table 4 Continued. MAR20-1 monazite results, PPM.

ID Tag:	PPM Ca	K	Si	Sr	P	As	Th
7 SD-MAR20-1	4190	42	308	49	129362	-49	20448
8 SD-MAR20-1	4011	3	1189	101	124240	346	25214
19 SD-MAR20-1	5066	22	1697	-5	121027	68	40441
20 SD-MAR20-1	3687	2	475	39	114152	388	22568
28 SD-MAR20-1	4560	18	1224	-37	111322	198	37923
29 SD-MAR20-1	6501	7	783	-4	113984	494	41816
9 SD-MAR20-1	6464	70	494	144	128952	344	34228
10 SD-MAR20-1	6382	-7	557	316	125538	-110	36945
11 SD-MAR20-1	5503	386	814	-11	126492	844	37072
17 SD-MAR20-1	3232	-2	2018	-24	123334	-81	36735
18 SD-MAR20-1	3494	19	337	17	125969	594	18367
15 SD-MAR20-1	4776	132	1349	-13	126866	-418	37459
16 SD-MAR20-1	7539	10	565	13	127378	-77	35917
12 SD-MAR20-1	6648	59	432	-4	127454	561	25258
3 SD-MAR20-1	3877	9	1576	21	126211	867	37472
5 SD-MAR20-1	7510	101	480	91	125548	-203	37901
14 SD-MAR20-1	4276	186	1902	21	124841	440	38873
4 SD-MAR20-1	4344	610	1584	24	124108	1005	38576
6 SD-MAR20-1	4815	16	1614	81	124990	268	40268
24 SD-MAR20-1	4051	1	603	75	115773	738	25370
7 SD-MAR20-1	7132	-4	1308	171	112894	-8273	51073
8 SD-MAR20-1	3760	74	599	166	128051	446	22982
9 SD-MAR20-1	7445	30	1148	258	125507	-125	52988
13 SD-MAR20-1	3633	311	650	98	124328	0	21980

Table 4 Continued. MAR20-1 monazite results, PPM.

ID Tag:	PPM U	Y	La	Ce	Pr	Nd	Sm
7 SD-MAR20-1	4998	16383	127060	262993	27536	114998	19029
8 SD-MAR20-1	3033	7777	123184	250102	27326	111296	17289
19 SD-MAR20-1	829	301	124230	253717	27486	115834	14814
20 SD-MAR20-1	2027	2683	116506	249212	28975	120862	18338
28 SD-MAR20-1	1063	288	121332	244409	27952	114713	14973
29 SD-MAR20-1	3288	1376	120291	238780	27004	109923	20157
9 SD-MAR20-1	6782	18107	127112	251666	25775	106690	17777
10 SD-MAR20-1	5637	10982	122227	247961	26177	109892	17691
11 SD-MAR20-1	2500	7013	129619	261814	27565	116452	18316
17 SD-MAR20-1	1324	1547	129507	269140	28699	122252	16681
18 SD-MAR20-1	4103	1598	131631	274396	29075	120246	20284
15 SD-MAR20-1	2235	6733	127293	264370	27841	118888	17714
16 SD-MAR20-1	13954	29109	110267	229435	24579	103305	22315
12 SD-MAR20-1	13702	31830	115686	235752	24607	102102	21854
3 SD-MAR20-1	905	318	134705	269412	28400	120036	14655
5 SD-MAR20-1	9169	16139	123490	245161	25248	107174	17103
14 SD-MAR20-1	828	440	134972	270142	28266	119738	14308
4 SD-MAR20-1	925	367	134874	268890	28071	119557	14805
6 SD-MAR20-1	891	434	128511	265674	28420	122006	15452
24 SD-MAR20-1	3695	13031	121535	238459	26479	108169	18175
7 SD-MAR20-1	4209	14509	112310	222808	24915	103436	17553
8 SD-MAR20-1	4156	13622	128758	255324	26741	112584	18729
9 SD-MAR20-1	3950	13634	123464	243064	24804	105403	15810
13 SD-MAR20-1	4368	14244	126747	251919	26304	111408	18258

Table 4 Continued. MAR20-1 monazite results, PPM.

ID Tag:	PPM Eu	Gd	Dy	Er	Yb	S	Pb	Total
7 SD-MAR20-1	2910	12468	4666	1298	134	-41	582	102.35
8 SD-MAR20-1	1244	10775	3320	793	373	49	572	97.4
19 SD-MAR20-1	868	5785	441	368	441	23	711	97.27
20 SD-MAR20-1	1360	8313	1138	376	193	-42	475	93.74
28 SD-MAR20-1	1160	4851	358	244	6	-32	690	92.95
29 SD-MAR20-1	1361	8916	915	224	222	-37	881	94.32
9 SD-MAR20-1	2096	15101	6439	1400	313	-39	948	102.46
10 SD-MAR20-1	3588	13777	4766	947	45	-43	935	100.12
11 SD-MAR20-1	1466	11410	2806	703	223	-36	748	102.15
17 SD-MAR20-1	1214	6456	848	220	45	-51	683	101.01
18 SD-MAR20-1	1610	10313	977	154	-210	-33	523	101.07
15 SD-MAR20-1	1373	10270	2627	617	131	-53	732	102.28
16 SD-MAR20-1	1866	22434	9761	2306	538	-90	1312	101.42
12 SD-MAR20-1	1843	22462	10227	2561	545	-79	1149	101.64
3 SD-MAR20-1	1241	4833	492	354	399	-33	678	101.5
5 SD-MAR20-1	2197	13203	5660	1068	49	-55	1120	100.64
14 SD-MAR20-1	1286	4702	444	103	41	-34	672	101.44
4 SD-MAR20-1	1352	5707	466	177	272	-34	691	101.25
6 SD-MAR20-1	1260	4993	497	174	88	-8	730	100.83
24 SD-MAR20-1	4187	15045	5883	1014	262	-49	482	95.28
7 SD-MAR20-1	3559	14601	5775	1062	148	-46	865	94.56
8 SD-MAR20-1	4633	15936	6175	902	113	-50	466	101.52
9 SD-MAR20-1	2779	12402	4591	903	320	-46	855	100.77
13 SD-MAR20-1	4385	15663	6294	926	133	-63	454	99.74

Table 4 Continued. MAR20-1 monazite results, WEIGHT %..

ID Tag:	Weight% CaO	K_2O	SiO_2	SrO	P_2O_5	As_2O_5	ThO_2	UO_2
7 SD-MAR20-1	0.586	0.005	0.066	0.006	29.64	-0.008	2.33	0.567
8 SD-MAR20-1	0.561	0	0.254	0.012	28.47	0.053	2.87	0.344
19 SD-MAR20-1	0.709	0.003	0.363	-0.001	27.73	0.01	4.6	0.094
20 SD-MAR20-1	0.516	0	0.102	0.005	26.16	0.06	2.57	0.23
28 SD-MAR20-1	0.638	0.002	0.262	-0.004	25.51	0.03	4.32	0.121
29 SD-MAR20-1	0.91	0.001	0.168	0	26.12	0.076	4.76	0.373
9 SD-MAR20-1	0.904	0.008	0.106	0.017	29.55	0.053	3.89	0.769
10 SD-MAR20-1	0.893	-0.001	0.119	0.037	28.77	-0.017	4.2	0.64
11 SD-MAR20-1	0.77	0.047	0.174	-0.001	28.98	0.13	4.22	0.284
17 SD-MAR20-1	0.452	0	0.432	-0.003	28.26	-0.012	4.18	0.15
18 SD-MAR20-1	0.489	0.002	0.072	0.002	28.86	0.091	2.09	0.466
15 SD-MAR20-1	0.668	0.016	0.289	-0.002	29.07	-0.064	4.26	0.254
16 SD-MAR20-1	1.05	0.001	0.121	0.002	29.19	-0.012	4.09	1.58
12 SD-MAR20-1	0.93	0.007	0.092	0	29.2	0.086	2.87	1.55
3 SD-MAR20-1	0.542	0.001	0.337	0.002	28.92	0.133	4.26	0.103
5 SD-MAR20-1	1.05	0.012	0.103	0.011	28.77	-0.031	4.31	1.04
14 SD-MAR20-1	0.598	0.022	0.407	0.002	28.61	0.067	4.42	0.094
4 SD-MAR20-1	0.608	0.074	0.339	0.003	28.44	0.154	4.39	0.105
6 SD-MAR20-1	0.674	0.002	0.345	0.01	28.64	0.041	4.58	0.101
24 SD-MAR20-1	0.567	0	0.129	0.009	26.53	0.113	2.89	0.419
7 SD-MAR20-1	0.998	-0.001	0.28	0.02	25.87	-1.269	5.81	0.477
8 SD-MAR20-1	0.526	0.009	0.128	0.02	29.34	0.068	2.62	0.471
9 SD-MAR20-1	1.04	0.004	0.246	0.03	28.76	-0.019	6.03	0.448
13 SD-MAR20-1	0.508	0.038	0.139	0.012	28.49	0	2.5	0.496

Table 4 Continued. MAR20-1 monazite results, WEIGHT %..

ID Tag:	Weight% Y_2O_3	La_2O_3	Ce_2O_3	Pr_2O_3	Nd_2O_3	Sm_2O_3	Eu_2O_3	Gd_2O_3
7 SD-MAR20-1	2.08	14.9	30.8	3.22	13.41	2.21	0.337	1.44
8 SD-MAR20-1	0.988	14.45	29.29	3.2	12.98	2	0.144	1.24
19 SD-MAR20-1	0.038	14.57	29.72	3.22	13.51	1.72	0.101	0.667
20 SD-MAR20-1	0.341	13.66	29.19	3.39	14.1	2.13	0.157	0.958
28 SD-MAR20-1	0.037	14.23	28.63	3.27	13.38	1.74	0.134	0.559
29 SD-MAR20-1	0.175	14.11	27.97	3.16	12.82	2.34	0.158	1.03
9 SD-MAR20-1	2.3	14.91	29.48	3.02	12.44	2.06	0.243	1.74
10 SD-MAR20-1	1.39	14.33	29.04	3.06	12.82	2.05	0.415	1.59
11 SD-MAR20-1	0.891	15.2	30.67	3.23	13.58	2.12	0.17	1.32
17 SD-MAR20-1	0.196	15.19	31.52	3.36	14.26	1.93	0.141	0.744
18 SD-MAR20-1	0.203	15.44	32.14	3.4	14.03	2.35	0.186	1.19
15 SD-MAR20-1	0.855	14.93	30.97	3.26	13.87	2.05	0.159	1.18
16 SD-MAR20-1	3.7	12.93	26.87	2.88	12.05	2.59	0.216	2.59
12 SD-MAR20-1	4.04	13.57	27.61	2.88	11.91	2.53	0.213	2.59
3 SD-MAR20-1	0.04	15.8	31.56	3.32	14	1.7	0.144	0.557
5 SD-MAR20-1	2.05	14.48	28.72	2.95	12.5	1.98	0.254	1.52
14 SD-MAR20-1	0.056	15.83	31.64	3.31	13.97	1.66	0.149	0.542
4 SD-MAR20-1	0.047	15.82	31.49	3.29	13.95	1.72	0.157	0.658
6 SD-MAR20-1	0.055	15.07	31.12	3.33	14.23	1.79	0.146	0.576
24 SD-MAR20-1	1.65	14.25	27.93	3.1	12.62	2.11	0.485	1.73
7 SD-MAR20-1	1.84	13.17	26.1	2.92	12.06	2.04	0.412	1.68
8 SD-MAR20-1	1.73	15.1	29.91	3.13	13.13	2.17	0.537	1.84
9 SD-MAR20-1	1.73	14.48	28.47	2.9	12.29	1.83	0.322	1.43
13 SD-MAR20-1	1.81	14.86	29.51	3.08	12.99	2.12	0.508	1.81

Table 4 Continued. MAR20-1 monazite results, WEIGHT %.

ID Tag:	Weight% Dy_2O_3	Er_2O_3	Yb_2O_3	SO_3	PbO
7 SD-MAR20-1	0.536	0.148	0.015	-0.01	0.063
8 SD-MAR20-1	0.381	0.091	0.042	0.012	0.062
19 SD-MAR20-1	0.051	0.042	0.05	0.006	0.077
20 SD-MAR20-1	0.131	0.043	0.022	-0.011	0.051
28 SD-MAR20-1	0.041	0.028	0.001	-0.008	0.074
29 SD-MAR20-1	0.105	0.026	0.025	-0.009	0.095
9 SD-MAR20-1	0.739	0.16	0.036	-0.01	0.102
10 SD-MAR20-1	0.547	0.108	0.005	-0.011	0.101
11 SD-MAR20-1	0.322	0.08	0.025	-0.009	0.081
17 SD-MAR20-1	0.097	0.025	0.005	-0.013	0.074
18 SD-MAR20-1	0.112	0.018	-0.024	-0.008	0.056
15 SD-MAR20-1	0.302	0.071	0.015	-0.013	0.079
16 SD-MAR20-1	1.12	0.264	0.061	-0.022	0.141
12 SD-MAR20-1	1.17	0.293	0.062	-0.02	0.124
3 SD-MAR20-1	0.056	0.041	0.045	-0.008	0.073
5 SD-MAR20-1	0.65	0.122	0.006	-0.014	0.121
14 SD-MAR20-1	0.051	0.012	0.005	-0.009	0.072
4 SD-MAR20-1	0.054	0.02	0.031	-0.009	0.074
6 SD-MAR20-1	0.057	0.02	0.01	-0.002	0.079
24 SD-MAR20-1	0.675	0.116	0.03	-0.012	0.052
7 SD-MAR20-1	0.663	0.121	0.017	-0.011	0.093
8 SD-MAR20-1	0.709	0.103	0.013	-0.013	0.05
9 SD-MAR20-1	0.527	0.103	0.036	-0.011	0.092
13 SD-MAR20-1	0.722	0.106	0.015	-0.016	0.049

Table 4 Continued. MAR20-1 monazite results, CATIONS.

	Cations						
ID Tag:	**Ca**	**K**	**Si**	**Sr**	**P**	**As**	**Th**
7 SD-MAR20-1	0.0244	0.0003	0.0026	0.0001	0.9751	-0.0002	0.0206
8 SD-MAR20-1	0.0244	0	0.0103	0.0003	0.9795	0.0011	0.0265
19 SD-MAR20-1	0.0313	0.0001	0.015	0	0.9672	0.0002	0.0431
20 SD-MAR20-1	0.0239	0	0.0044	0.0001	0.9586	0.0013	0.0253
28 SD-MAR20-1	0.03	0.0001	0.0115	-0.0001	0.9485	0.0007	0.0431
29 SD-MAR20-1	0.0421	0	0.0072	0	0.9541	0.0017	0.0467
9 SD-MAR20-1	0.0377	0.0004	0.0041	0.0004	0.972	0.0011	0.0344
10 SD-MAR20-1	0.0382	0	0.0048	0.0009	0.972	-0.0003	0.0382
11 SD-MAR20-1	0.0325	0.0023	0.0069	0	0.9657	0.0026	0.0378
17 SD-MAR20-1	0.0194	0	0.0173	-0.0001	0.9573	-0.0003	0.0381
18 SD-MAR20-1	0.0208	0.0001	0.0029	0	0.9716	0.0019	0.0189
15 SD-MAR20-1	0.0281	0.0008	0.0113	0	0.9656	-0.0013	0.0381
16 SD-MAR20-1	0.0443	0.0001	0.0047	0	0.9688	-0.0002	0.0365
12 SD-MAR20-1	0.039	0.0004	0.0036	0	0.9669	0.0018	0.0256
3 SD-MAR20-1	0.023	0.0001	0.0133	0.0001	0.968	0.0027	0.0384
5 SD-MAR20-1	0.0447	0.0006	0.0041	0.0002	0.9676	-0.0006	0.039
14 SD-MAR20-1	0.0254	0.0011	0.0161	0.0001	0.9612	0.0014	0.04
4 SD-MAR20-1	0.026	0.0037	0.0135	0.0001	0.9601	0.0032	0.0398
6 SD-MAR20-1	0.0288	0.0001	0.0138	0.0002	0.9657	0.0009	0.0415
24 SD-MAR20-1	0.0258	0	0.0055	0.0002	0.9547	0.0025	0.0279
7 SD-MAR20-1	0.046	0	0.0121	0.0005	0.9431	-0.0352	0.057
8 SD-MAR20-1	0.0221	0.0004	0.005	0.0004	0.9747	0.0014	0.0234
9 SD-MAR20-1	0.0443	0.0002	0.0097	0.0007	0.9663	-0.0004	0.0545
13 SD-MAR20-1	0.0219	0.0019	0.0056	0.0003	0.968	0	0.0228

Table 4 Continued. MAR20-1 monazite results, CATIONS.

ID Tag:	Cations U	Y	La	Ce	Pr	Nd	Sm
7 SD-MAR20-1	0.0049	0.043	0.2136	0.4382	0.0456	0.1862	0.0295
8 SD-MAR20-1	0.0031	0.0214	0.2166	0.4359	0.0474	0.1885	0.0281
19 SD-MAR20-1	0.0009	0.0008	0.2214	0.4482	0.0483	0.1988	0.0244
20 SD-MAR20-1	0.0022	0.0078	0.2182	0.4627	0.0535	0.218	0.0317
28 SD-MAR20-1	0.0012	0.0009	0.2305	0.4604	0.0524	0.2099	0.0263
29 SD-MAR20-1	0.0036	0.004	0.2245	0.4419	0.0497	0.1976	0.0347
9 SD-MAR20-1	0.0067	0.0475	0.2136	0.4194	0.0427	0.1727	0.0276
10 SD-MAR20-1	0.0057	0.0296	0.211	0.4244	0.0446	0.1828	0.0282
11 SD-MAR20-1	0.0025	0.0187	0.2206	0.4419	0.0463	0.1909	0.0288
17 SD-MAR20-1	0.0013	0.0042	0.2241	0.4618	0.049	0.2038	0.0267
18 SD-MAR20-1	0.0041	0.0043	0.2264	0.4679	0.0493	0.1992	0.0322
15 SD-MAR20-1	0.0022	0.0179	0.216	0.4448	0.0466	0.1944	0.0278
16 SD-MAR20-1	0.0138	0.0771	0.187	0.3858	0.0411	0.1688	0.035
12 SD-MAR20-1	0.0135	0.0841	0.1957	0.3954	0.041	0.1664	0.0341
3 SD-MAR20-1	0.0009	0.0008	0.2304	0.4568	0.0479	0.1977	0.0231
5 SD-MAR20-1	0.0092	0.0433	0.2122	0.4177	0.0428	0.1774	0.0271
14 SD-MAR20-1	0.0008	0.0012	0.2317	0.4598	0.0478	0.198	0.0227
4 SD-MAR20-1	0.0009	0.001	0.2326	0.4598	0.0477	0.1986	0.0236
6 SD-MAR20-1	0.0009	0.0012	0.2214	0.4538	0.0483	0.2025	0.0246
24 SD-MAR20-1	0.004	0.0374	0.2235	0.4347	0.048	0.1916	0.0309
7 SD-MAR20-1	0.0046	0.0422	0.2092	0.4115	0.0458	0.1856	0.0302
8 SD-MAR20-1	0.0041	0.0361	0.2185	0.4297	0.0447	0.1841	0.0294
9 SD-MAR20-1	0.004	0.0366	0.212	0.4137	0.042	0.1743	0.0251
13 SD-MAR20-1	0.0044	0.0386	0.22	0.4336	0.045	0.1863	0.0293

Table 4 Continued. MAR20-1 monazite results, CATIONS.

		Cations							
ID Tag:		**Eu**	**Gd**	**Dy**	**Er**	**Yb**	**S**	**Pb**	**CatSum**
7	SD-MAR20-1	0.0045	0.0185	0.0067	0.0018	0.0002	-0.0003	0.0007	1.041
8	SD-MAR20-1	0.002	0.0167	0.005	0.0012	0.0005	0.0004	0.0007	1.0289
19	SD-MAR20-1	0.0014	0.0091	0.0007	0.0005	0.0006	0.0002	0.0008	1.0457
20	SD-MAR20-1	0.0023	0.0137	0.0018	0.0006	0.0003	-0.0003	0.0006	1.0669
28	SD-MAR20-1	0.002	0.0081	0.0006	0.0004	0	-0.0003	0.0009	1.0779
29	SD-MAR20-1	0.0023	0.0147	0.0015	0.0003	0.0003	-0.0003	0.0011	1.072
9	SD-MAR20-1	0.0032	0.0224	0.0093	0.002	0.0004	-0.0003	0.0011	1.0453
10	SD-MAR20-1	0.0057	0.021	0.007	0.0014	0.0001	-0.0003	0.0011	1.0441
11	SD-MAR20-1	0.0023	0.0172	0.0041	0.001	0.0003	-0.0003	0.0009	1.0545
17	SD-MAR20-1	0.0019	0.0099	0.0013	0.0003	0.0001	-0.0004	0.0008	1.0594
18	SD-MAR20-1	0.0025	0.0157	0.0014	0.0002	-0.0003	-0.0002	0.0006	1.0461
15	SD-MAR20-1	0.0021	0.0154	0.0038	0.0009	0.0002	-0.0004	0.0008	1.0507
16	SD-MAR20-1	0.0029	0.0336	0.0141	0.0032	0.0007	-0.0007	0.0015	1.0496
12	SD-MAR20-1	0.0028	0.0336	0.0148	0.0036	0.0007	-0.0006	0.0013	1.0551
3	SD-MAR20-1	0.0019	0.0073	0.0007	0.0005	0.0005	-0.0002	0.0008	1.044
5	SD-MAR20-1	0.0035	0.02	0.0083	0.0015	0.0001	-0.0004	0.0013	1.0528
14	SD-MAR20-1	0.002	0.0071	0.0007	0.0001	0.0001	-0.0003	0.0008	1.0554
4	SD-MAR20-1	0.0021	0.0087	0.0007	0.0003	0.0004	-0.0003	0.0008	1.0602
6	SD-MAR20-1	0.002	0.0076	0.0007	0.0002	0.0001	-0.0001	0.0008	1.0484
24	SD-MAR20-1	0.007	0.0244	0.0092	0.0015	0.0004	-0.0004	0.0006	1.0723
7	SD-MAR20-1	0.0061	0.024	0.0092	0.0016	0.0002	-0.0004	0.0011	1.0865
8	SD-MAR20-1	0.0072	0.0239	0.009	0.0013	0.0002	-0.0004	0.0005	1.0396
9	SD-MAR20-1	0.0044	0.0188	0.0067	0.0013	0.0004	-0.0003	0.001	1.0492
13	SD-MAR20-1	0.007	0.024	0.0093	0.0013	0.0002	-0.0005	0.0005	1.0517

B Bibliography

Allaz, Julien, 3022, Theriak-Domino Short Course: A program created by Christian de Capitani, UMass Amherst Geosciences.

Allaz, J. M., Jercinovic, M. J., and Williams, M. L., 2020, U-Th-Pb Total dating of REE-phosphate by electron microprobe: Review and progress, IOP Conference Series: Materials Science and Engineering, 891, 012001, doi:10.1088/1757-899X/891/1/012001.

Ashwal, L.D., Leo, G.W., Robinson, P., Zartman, R.E., and Hall, D.J., 1979, The Belchertown Quartz Monzodiorite Pluton, West-Central Massachusetts: A Syntectonic Acadian Intrusion: American Journal of Science, v. 279, p. 936–969.

Cherniak, D.J. and Pyle, J.M., 2008, Th diffusion in monazite, Chemical Geology 256, pgs. 52-61.

de Capitani C. and Petrakakis K., 2010. The computation of equilibrium assemblage diagrams with Theriak/Domino software. American Mineralogist, v. 95, p. 1006-1016.

de Capitani, Christian. Theriak-Domino program and User Guide. University of Basel, Mineralogy and Petrography. Accessed August, 2020.
https://titan.minpet.unibas.ch/minpet/theriak/theruser.html.

Förster, H.-J., 1998, The chemical composition of REE-Y-Th-U-rich accessory minerals in peraluminous granites of the Erzgebirge-Fichtelgebirge region, Germany, Part I: The monazite-(Ce)-brabantite solid solution series, American Mineralogist, vol. 83, pp. 259-272.

Förster, H.-J., 2006, Composition and origin of intermediate solid solutions in the system thorite-xenotime-zircon-coffinite, Lithos 88, pp. 35-55.

Förster, H.-J., and Harlov, D.E., 1999, Monazite-(Ce)-huttonite solid solutions in granulite-facies metabasites from the Ivrea-Verbano Zone, Italy, Mineralogical Magazine, vol. 63 (4), pp. 587-594.

Harlov, Daniel E. and Hetherington, Callum J., 2010, Partial high-grade alteration of monazite using alkali-bearing fluids: Experiment and nature, American Mineralogist, v. 95, pgs 1105-1108.

Markley, M.J., Dunn, S.R., Jercinovic, M.J., Peck, W.H., and Williams, M.L., 2018, Monazite U-Th-Pb geochronology of the Central Metasedimentary Belt Boundary Zone (CMBbz), Grenville Province, Ontario Canada: Canadian Journal of Earth Sciences, v. 99, p. 1063–1078, doi:https://doi.org/10.1139/cjes-2018-0039.

Martins, Lucelene, Vlach, Silvio Roberto Farias, and de Assis Janasi, Valdecir, 2009, Reaction microtextures of monazite: Correlation between chemical and age domains in the Nazare Paulista migmatite, SE Brazil, Chemical Geology, vol. 261, pp. 271-285.

Massey, M.A., and Moecher, D.P., 2008, Preliminary bedrock geologic map of the Palmer quadrangle, Massachusetts: Office of the Massachusetts State Geologist Open

File Report 08-02. Scale 1:24,000. 1 sheet and digital product: Adobe PDF and ESRI ArcGIS database.

Pyle, Joseph M., Spear, Frank S., Rudnick, Roberta L., and McDonough, William F., 2001, Monazite-xenotime-garnet equilibrium in metapelites and a new monazite-garnet thermometer, Journal of Petrology, vol. 42, pp. 2083-2017.

Robinson, P., 1992. In Guidebook for Field Trips in the Connecticut Valley Region of Massachusetts and the Adjacent States, New England Intercollegiate Geosciences Conference #84. Amherst, 1992. Robinson, Peter, and Brady, John B., editors.

Robinson, Peter, Tucker, Robert D., Bradley, Dwight, Berry IV, Henry N., and Osberg, Philip H., 1998, Paleozoic orogens in New England, USA, GFF, vol. 120, pp. 119-148.

Robinson, P., Unpublished Guidebook, Massachusetts Geological Society, 2016.

Shaw, Denis M., 1956, Geochemistry of pelitic rocks. Part III: Major elements and general geochemistry, Bulletin of the Geological Society of America, vol. 67, pp. 919-934.

Williams, Michael L., Grover, Timothy, Jercinovic, Michael J., Regan, Sean P., Pless, Claire R., and Suarez, Kaitlyn A., 2019, Constraining the timing and character of crustal melting in the Adirondack Mountains using multi-scale compositional mapping and in-situ monazite geochronology, American Mineralogist, vol. 104, pp. 1585-1602.

Williams, Michael L., Jercinovic, Michael J., and Hetherington, Callum J., 2007, Microprobe Monazite Geochronology: Understanding Geologic Processes by Integrating Composition and Chronology: Annual Review of Earth and Planetary Sciences, v. 35, p. 137-75, doi:10.1146/annurev.earth.35.031306.140228

Williams, Michael L., Jercinovic, Michael J., Mahan, Kevin H., and Dumond, Gregory, 2017, Electron Microprobe Petrochronology: Reviews in Mineralogy and Geochemistry, v. 83, p. 153-182.

Williams, M.L., Jercinovic, M.J., Harlov, D.E., Bydzyn, B., and Hetherington, C.J., 2011, Resetting monazite ages during fluid-related alteration, Chemical Geology, vol. 283, pp. 218-225.